Understanding the role of Fe-O hybridization in the characteristic transitions of iron oxide nanoparticles

by

Rachel Alexandra Nickel

A thesis submitted to
The Faculty of Graduate Studies of
The University of Manitoba
in partial fulfillment of the requirements
of the degree of

PhD

Department of Physics and Astronomy
The University of Manitoba
Winnipeg, Manitoba, Canada
July 2023

Thesis advisor

Dr. Johan van Lierop

Author

Rachel Alexandra Nickel

Understanding the role of Fe-O hybridization in the characteristic transitions of iron oxide nanoparticles

Abstract

Iron oxides have long attracted interest for both their fascinating scientific properties and potential applications due to their strong electron correlations and competing degrees of freedom. The evolution of these interactions underpins the electronic and magnetic transitions that occur, resulting in states that exhibit everything from simple ferrimagnetism to complex multiferroicity. However, the relationship between the underlying interactions and the overall material properties is not well-understood. In this work, the characteristic transitions of Fe_3O_4 and ϵ-Fe_2O_3 are studied to identify the role of Fe-O hybridization.

While the trimeron model has been accepted as the mechanism behind the Verwey transition in bulk Fe_3O_4, the disappearance of this metal-insulator transition in nanoparticles has not been addressed. By studying three sizes of Fe_3O_4 nanorods, a clear relationship between strain and the Verwey transition temperature (T_V) appears. Isotropic compressive strain (which typically occurs in spherical nanoparticles) reduces T_V, while uniaxial tensile strain increases T_V. Detailed study of the largest Fe_3O_4 nanorods confirms the formation of orbitally-ordered trimerons in the low temperature insulating phase, albeit a modified trimeron state from that of bulk Fe_3O_4.

Such altered hybridization causes T_V to shift in strained nanoparticles.

In ϵ-Fe_2O_3, the DO_{h1} octahedral chains create a complicated electronic structure which yields complex hybridization. As a result, the physical mechanism behind the characteristic transition of ϵ-Fe_2O_3 is unresolved. Full characterization of three sizes of ϵ-Fe_2O_3 reveal that this transition is purely electronic with no structural changes observed. Perturbed transition metal-doped ϵ-Fe_2O_3 provide further insights. In particular, temperature dependent hyperfine parameters (from Mössbauer spectroscopy) show high temperature charge ordering in the Cr-doped nanoparticles. Combined with the undoped ϵ-Fe_2O_3 behaviour, the transition is caused by the onset of super-transferred hyperfine interactions between T_d sites.

Contents

List of Figures

List of Tables

Acknowledgments

I would like to thank my supervisor, Dr. Johan van Lierop, for his continued support. His commitment to providing a productive, challenging environment has allowed me to develop as a person and a researcher. I am incredibly grateful for all of the opportunities and experiences I have had during my time in his research group. I would also like to thank all of members of the Nanomagnetism Research Group, for the assistance, helpful discussions and friendship you have provided.

I would also like to thank Prof. Chuenhou Ouyang, Ashok Ranjan and C.-C. Chi from National Tsing Hua University who contributed directly to this research via the transmission electron microscopy work which provided invaluable insights into the Fe_3O_4 nanorod crystal strain. This work has also benefited from the support of John Freeland, Richard Rosenberg, David Keavney, Chengjun Sun and Debora Motta Meira during experiments at the Advanced Photon Source, and Padraic Shafer at the Advanced Light Source. In particular, discussions with John Freeland were invaluable to the Fe_3O_4 nanorod analysis. Special thanks to Peiqing Wang for his assistance with liquid helium and lab equipment. Additionally, I would like to thank the Physics and Astronomy office staff: Robyn Beaulieu, Susan Beshta, and Aymsley Bishop-Mahon for the support they provide to all students within the Department.

I would like to thank the University of Manitoba and the Natural Sciences and Engineering Research Council of Canada (NSERC) for their financial support. Use of the Advanced Photon Source at Argonne National Laboratories, an Office of Science User Facility operated for the U.S. Department of Energy (DOE) Office of Science by Argonne National Laboratory, was supported by the US DOE under contract DE-AC02-06CH11357. Use of the Advanced Light Source, a US Department of Energy

(DOE) Office of Science User Facility was supported by the US DOE under contract DE-AC02-05CH11231.

Finally, I would like to thank my family and friends who have supported me throughout my studies.

For my grandfather.

Chapter 1

Introduction

Though simple in chemical composition, the iron oxide polymorphs are an incredibly diverse category of materials. Their natural abundance and unique properties have attracted multidisciplinary interest, with innumerable studies dedicated to understanding the underlying chemistry and physics of these compounds, and utilizing them in novel applications.[1] This work will focus on the former. As with other transition metal oxides, the properties of iron oxides are a product of structure, strong electronic correlations and the competition between different degrees of freedom.[2] These many factors yield a rich playground for scientific exploration.

In this work, two iron oxide polymorphs will be examined: Fe_3O_4, perhaps the oldest known magnetic material, and ϵ-Fe_2O_3, a far more novel phase. Both of these polymorphs exhibit temperature dependent transitions resulting in distinct high and low temperature states. The transition which occurs in Fe_3O_4, known as the Verwey transition, has been the subject of many studies since its discovery in 1939.[3–6] Though a physical model has been developed for the Verwey transition in bulk Fe_3O_4,

the transition in nanoparticles not well-understood. Nanoparticles cannot simply be considered as very small versions of the bulk material. While nanoparticles do maintain many of the properties of their bulk analogues, finite size effects, increased surface and disorder make them unique.[7–9]

The challenges associated with nanoparticle research are amplified with ϵ-Fe_2O_3 because this polymorph does not exist in bulk.[10] As such, the characteristics of this unique phase are convolved with the complexity inherent to nanoparticles, and the underlying physics has remained elusive. The goal of this research is to understand the Fe-O interactions that underpin the behaviour of both Fe_3O_4 and ϵ-Fe_2O_3 nanoparticles, particularly through their characteristic transitions.

The structure of this Thesis is as follows: chapter 1 contains a brief overview of bulk and nanoparticle magnetism, and introduces the iron oxide polymorphs and multiferroicity. Chapter 2 describes the protocols used to synthesize the nanoparticle samples as well as the experimental techniques used to characterize their structure, electronic and magnetic properties. Chapter 3 examines the role of strain in the Verwey transition of Fe_3O_4 nanorods, while Chapters 4 and 5 focus on ϵ-Fe_2O_3 nanoparticles. Specifically, chapter 4 characterizes different sizes of ϵ-Fe_2O_3 nanoparticles to decouple size effects, and chapter 5 examines the impact of perturbing the structure using small amounts of transition metal dopant ions. Chapter 6 compares the transitions of Fe_3O_4 and ϵ-Fe_2O_3 and uses the results of the transition metal-doped ϵ-Fe_2O_3 to develop a model of the Fe-O hybridization behind the characteristic ϵ-Fe_2O_3 transition. Chapter 7 contains overall conclusions and suggestions for future work.

1.1 Bulk Magnetism

1.1.1 Magnetic States

Magnetism in bulk materials originates from the interactions between its atomic moments. The way that these moments align as a consequence of this coupling is used to classify the magnetism in a material. Figure 1.1 shows different types of magnetic ordering. Ferromagnetic materials exhibit perhaps the most simple ordering, where even in the absence of a magnetic field, strong long range coupling cause the atomic dipole moments to align below the Curie temperature (T_C). In antiferromagnetic materials the atomic moments align in an antiparallel configuration within a unit cell such that the net moment is zero below the Néel temperature (T_N). This antiparallel

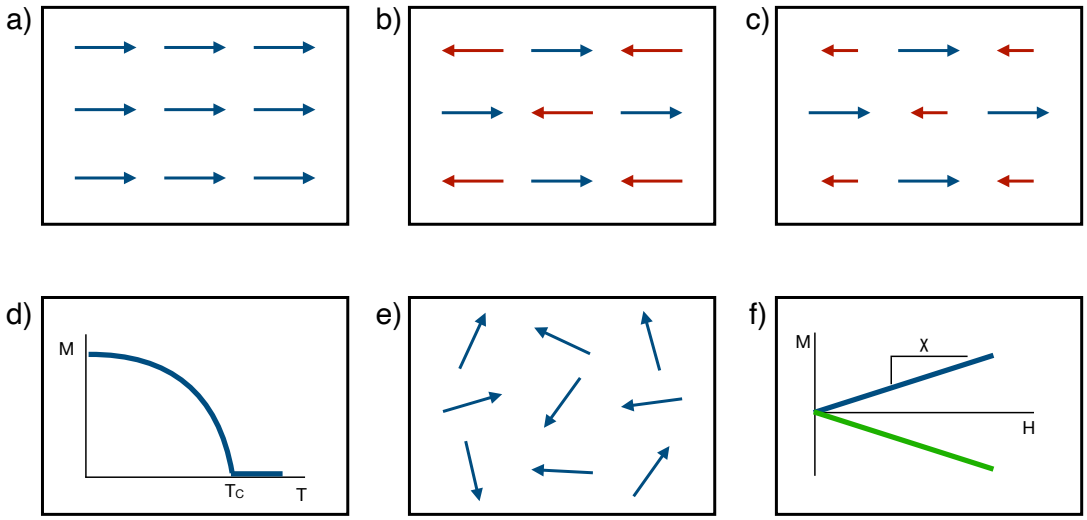

Figure 1.1: Schematic of magnetic moment configuration of a) ferromagnetic, b) antiferromagnetic and c) ferrimagnetic materials. d) Temperature dependence of magnetic moment vanishes at ordering temperature T_C when ferromagnetic material becomes e) paramagnetic. f) Field dependent magnetization of paramagnetic (blue) and diamagnetic (green) materials.

configuration is also present in ferrimagnetic materials. However, in ferrimagnets the magnetic moments do not fully compensate and so there is a net magnetic moment below T_C. Above the ordering temperatures (either T_C or T_N), these materials become paramagnetic as the atomic moments lack spontaneous ordering in the absence of a magnetic field. Paramagnetic materials exhibit a positive susceptibility (χ) in an applied magnetic field, in contrast to diamagnetic materials which have a negative susceptibility.[11]

1.1.2 Magnetic Exchange Interactions

The couplings between the atomic moments that determine the magnetic ordering are the magnetic exchange interactions. For localized electrons, such interactions are a quantum mechanical effect based on the Coulomb repulsion between electrons and the Pauli exclusion principle that prohibits electrons from having the same quantum number. The interaction between two spins ($\vec{S_i}$ and $\vec{S_j}$) is described by the Heisenberg Hamiltonian as

$$\mathcal{H} = -2\sum_{i<j} J_{ij}\vec{S_i}\cdot\vec{S_j} \tag{1.1}$$

where J_{ij} is the exchange constant between atoms at sites i and j. The magnitude of J_{ij} indicates the strength of the interaction, while the sign indicates if the alignment is parallel ($J_{ij} > 0$) or antiparallel ($J_{ij} < 0$). This Heisenberg interaction relies on orbital overlap to determine the strength of J_{ij}, and so describes direct interactions.[11]

However, in most materials, the magnetic ions are not sufficiently close for the orbital overlap necessary for direct interactions, and indirect interactions dominate. In transition metal (M) oxides, superexchange couples next-nearest neighbour ions

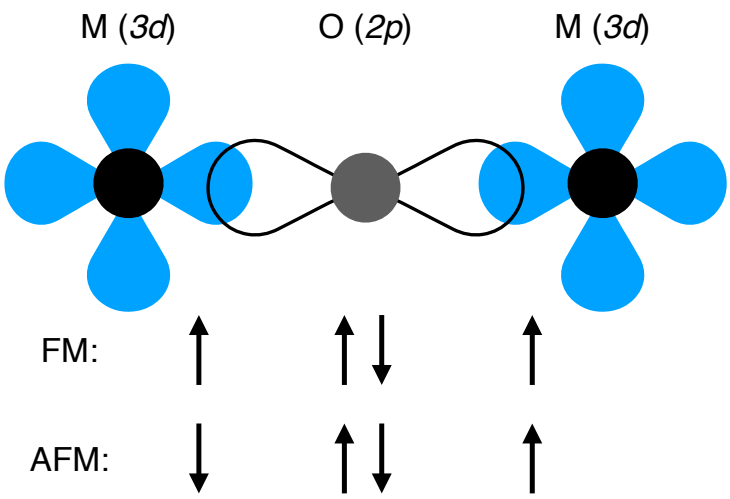

Figure 1.2: Schematic of a typical superexchange bond. For 180° bond with orbital overlap pictured, antiferromagnetic coupling (AFM) is energetically favourable over ferromagnetic coupling (FM).

through the hybridization of $3d$ orbitals with oxygen $2p$ orbitals as shown in figure 1.2. These mediated interactions can also be described by the Heisenberg Hamiltonion where J is determined by the M-O-M bond angle, interatomic separation, and occupancy and orbital degeneracy of the $3d$ orbitals.[12] The Goodenough-Kanamori rules[13,14] provide a framework for determining the sign and strength of J. Three cases to consider are as follows:

1. If the cations have singly occupied d orbitals which point towards each other with large overlap, then the exchange is strong and antiferromagnetic ($J < 0$). This is the typical case for M-O-M bonds from 120° to 180°.

2. If the cations have singly occupied d orbitals with an overlap integral that is zero by symmetry, then the exchange is fairly weak and ferromagnetic ($J > 0$). This is the typical case for M-O-M bonds of ∼90°.

3. If one cation has singly occupied and the other has empty or doubly occupied d orbitals of the same type that overlap, then the exchange is relatively weak and ferromagnetic ($J > 0$).

As the first case where orbital overlap is significant occurs most frequently, superexchange interactions are typically antiferromagnetic as shown in figure 1.3.

For oxides of mixed valence that contain both localized and delocalized d electrons, double exchange interactions are also possible. In a double exchange interaction one electron is able to hop from one cation to a neighbouring site that has a vacancy of the same spin. Because spin flips of the hopping electron are not permitted and Hund's rules dictate the filling of orbitals,[11] ferromagnetic interactions are favoured as shown in figure 1.3. Such interactions are evident in the octahedral sites of Fe_3O_4 where the electron hopping results in semi-metallic properties.

Anisotropic exchange or the Dzyaloshinskii–Moriya interaction (DMI) appears with broken inversion symmetry and arises from spin-orbit coupling.[15] The DMI ($\vec{D}$)

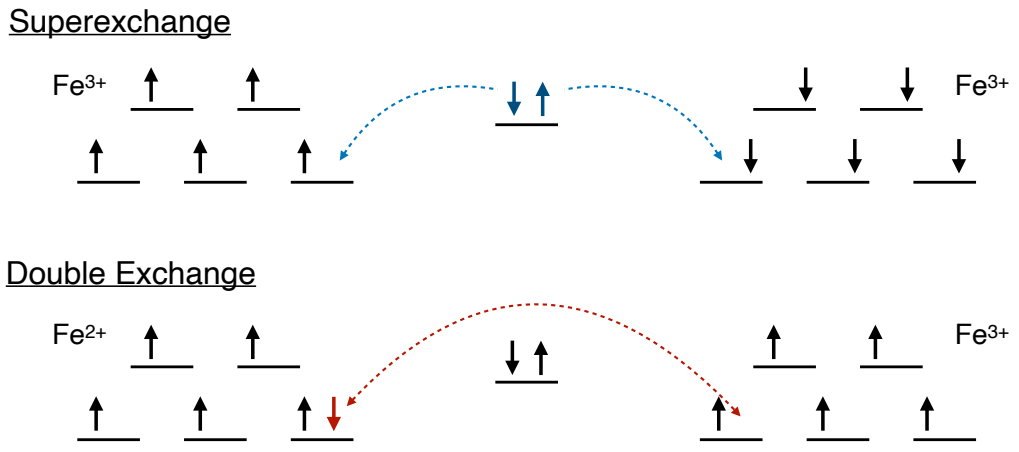

Figure 1.3: Schematics of AFM superexchange between two Fe^{3+} ions and FM double exchange between Fe^{3+} and Fe^{2+}.

between two spins is described by the Hamiltonian

$$\mathcal{H}_{DM} = \vec{D} \cdot \vec{S_i} \times \vec{S_j} \tag{1.2}$$

Unlike the exchange interactions based on the Heisenberg Hamiltonian discussed previously, DMI favours a canted spin configuration and is a weaker overall effect. However, DMI plays an essential role in many magnetic systems such as weak ferromagnets, spin glasses and multiferroics.[16,17] Notably the weak ferromagnetic moment of α-Fe_2O_3 is one of the original examples of DMI.[18]

1.1.3 Magnetic Anisotropy

Magnetic anisotropy (K) is used to describe how the magnetization of a material exhibits a preferred orientation. The overall anisotropy is the result of both intrinsic and extrinsic factors.

Magnetocrystalline anisotropy is intrinsic to a given material. Its largest contribution is single ion anisotropy where crystal-field interactions stabilize particular magnetic orbitals, and the spin-orbit interactions cause the magnetic moments to align in a crystallographic direction.[11] An axis of preferred alignment is known as the magnetic 'easy' axis. If only one easy axis exists, then the material has uniaxial anisotropy.[12] The energy required to rotate the magnetization from an easy axis to a 'hard' axis for such a system can be described by

$$E = K_{u,1} \sin^2(\theta) + K_{u,2} \sin^4(\theta) + K_{u,3} \sin^6(\theta) \tag{1.3}$$

where $K_{u,i}$ are the uniaxial anisotropy constants and θ is the angle between the magnetization and the easy axis. Regardless of its symmetry, magnetocrystalline

anisotropy depends on an asymmetric crystal field, non-zero orbital momentum to couple the orbit to the crystal field, and non-zero spin orbit coupling. The interplay between these factors determines the magnitude of the magnetocrystalline anisotropy constants.[11]

Shape anisotropy is an extrinsic factor determined by the shape of a particular sample. This anisotropy arises from the demagnetization field ($\mathcal{N}$) and only plays a significant role in samples that are small enough to remain single domain. For an ellipsoid sample with magnetic saturation M_S along its easy axis, the shape anisotropy (K_{sh}) is

$$K_{sh} = \frac{1}{4}\mu_0 M_S^2(1 - 3\mathcal{N}) \tag{1.4}$$

where $\mathcal{N}$ of the ellipsoid depends on the aspect ratio ($\alpha = c/a > 1$) via

$$\mathcal{N} = \frac{1}{(\alpha^2 - 1)}\left(\frac{\alpha}{\sqrt{\alpha^2 - 1}}\cosh^{-1}(\alpha)\right) \tag{1.5}$$

Note that for a sphere, $\mathcal{N} = 1/3$ and so $K_{sh} = 0$ as expected. Surface anisotropy also contributes to overall anisotropy; this will be discussed further in section 1.2.2

1.1.4 Bulk Magnetic Properties

In the picture presented thus far, one would expect a ferromagnetic material to exhibit fully aligned magnetic moments below its ordering temperature, even in the absence of a magnetic field. However, such behaviour is not usually observed, due to the formation of magnetic domains that reduce the magnetostatic energy of the system. Note that the formation of each domain requires the creation of a domain wall which costs energy depending on the exchange stiffness and anisotropy of the material.[12,15] For sufficiently small samples, the cost of domain wall formation exceeds

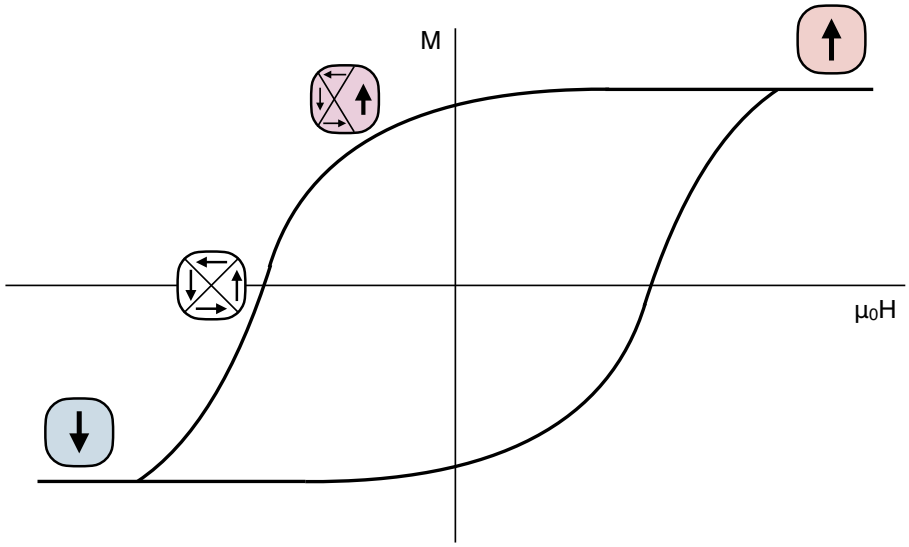

Figure 1.4: Schematic showing the relationship between a hysteresis loop and the domain structure of a bulk ferromagnet.

the magnetostatic energy reduction and so they remain single domain.

A consequence of this domain formation is that magnetization measurements are impacted by the behaviour of the domains and not just individual magnetic moments. A hysteresis loop (as shown in figure 1.4) is the typical measurement to probe magnetic response. Such a measurement often begins by applying a large field which aligns all the magnetic moments, inducing maximum magnetization, known as the magnetic saturation (M_S) and eliminating the domain structure. As the magnitude of the applied field is reduced, there is insufficient energy to keep all the moments aligned and the magnetization begins to decrease. This decrease is typically initiated by coherent rotation of the moments before reversed domains nucleate and spread through the material. The applied field where the net magnetic moment is zero is known as the coercive field ($\mu_0 H_C$).

1.2 Nanoparticle Magnetism

The magnetism of nanoparticles is significantly different from that of their bulk analogues. While the intrinsic properties of the material are retained, finite size effects create geometric restrictions and the large fraction of atoms in broken coordination induce surface effects. These combined effects impact the behaviour of individual nanoparticles, while interparticle interactions further modify the overall properties.

1.2.1 Superparamagnetism

Interesting magnetic properties arise when the size of a material becomes comparable to characteristic length scales such as the exchange length and domain wall width.[12] One of the most common consequences is that when the particle size is sufficiently small, the formation of domain walls becomes unfavourable and the particles become single domain. The critical diameter is proportional to $A^{1/2}/M_S$ where A is the exchange stiffness constant and M_S is the magnetic saturation as usual.[19]

In a simple single domain nanoparticle, the Stoner-Wohlfarth model can be used to describe the magnetism.[20] To start, the energy barrier to reversing the moment of a single uniaxial particle is considered. From Equation 1.3, this relationship takes the form $\Delta E = KV \sin^2\theta$ in the absence of an applied magnetic field, resulting in an energy barrier of $\Delta E = KV$. However, thermal effects need to be considered. For a collection of nanoparticles at a non-zero temperature T, the magnetization will fluctuate as a function of time t via

$$\frac{dM}{dt} = -\frac{1}{\tau_0} M e^{-\frac{\Delta E}{k_B T}} = -\frac{M}{\tau} \tag{1.6}$$

where $1/\tau_0$ is the number of times the system attempts to surpass the energy barrier ΔE and τ is the relaxation time. The Néel-Arrhenius Law is obtained by rearranging this equation into the following:[21]

$$\tau = \tau_0 \exp\left(\frac{\Delta E}{k_B T}\right) \tag{1.7}$$

Essentially this law describes the probability of the moments spontaneously flipping due to thermal effects. At $T = 0$, the magnetization is fixed and no fluctuations are possible. An increase in system temperature allows fluctuations to occur. If T becomes sufficiently high that $k_B T$ exceeds ΔE, then the energy barrier to reversal effectively vanishes and the system will exhibit no net magnetization in the absence of a magnetic field. The overall behaviour of the system becomes similar to that of a paramagnet, albeit with a larger effective magnetization. This situation is known as 'superparamagnetism', and the threshold temperature is referred to as the superparamagnetic blocking temperature (T_B).

1.2.2 Surface Effects

One of the most significant effects of shifting from a bulk system to a nanoscale system is the significant role of surface effects. At the surface of nanoparticles, atoms exist in an altered coordination environment. Typically these surface ions have a broken crystallographic symmetry with a reduced coordination number, resulting in relaxation of the lattice. These variations in the atomic structure at the surface are coupled to altered electronic bonding, which then impacts the exchange interactions that control magnetism. Because it is practically impossible to separate the different effects that can occur at the surface, the concept of surface anisotropy (K_S) is

used.[11,22,23]

This surface anisotropy combines with the bulk crystal and shape anisotropies to yield the effective anisotropy. The relative importance of surface anisotropy to a particular system is primarily dependent on its surface area to volume ratio. As a result surface anisotropy has a greater role in smaller nanoparticles, due to the relative increase in surface atoms.[24] While experimental determination of the spin structure due to surface anisotropy remains difficult, simulations reveal that the magnetic behaviour depends on the magnitude of surface anisotropy (K_S) compared to bulk anisotropy

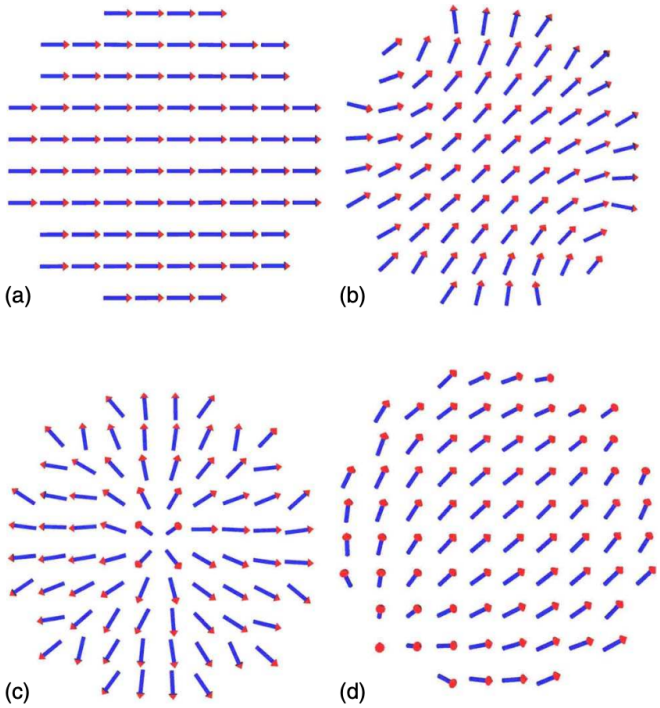

Figure 1.5: Simulated spin configurations of a particle with simple cubic structure: a) collinear ferromagnetic configuration if K_S=0, b) throttled configuration, c) hedgehog configuration, and d) artichoke configuration. Reprinted figure with permission from L Berger, Y Labaye, M Tamine, and JMD Coey. Physical Review B, 77(10):104431, 2008. Copyright 2008 by the American Physical Society.

(K_V).[22] Figure 1.5 shows the simulated spin configurations of a nanoparticle where K_S/K_V is varied. Surface spins are perfectly collinear to bulk spins when K_S=0, while a 'throttled' or 'flower' configuration (see figure 1.5b) occurs as K_S increases. The 'hedgehog' configuration occurs as an extreme case when K_S/K_V becomes very large, resulting in no net moment. If K_S is negative, the easy direction lies parallel to the particle surface and an 'artichoke' configuration occurs.[25] Because K_S is estimated to be $\sim$1 mJ/m^2[26] – several orders of magnitude larger than K_V of most cubic ferromagnets,[22] surface anisotropy effects are critical to nanomagnetism.

1.3 Iron Oxide

Iron oxides are amongst the oldest known magnetic materials and have been used for incredibly diverse applications. Though composed of only iron and oxygen ions, variations in composition and structure yield six distinct iron oxides, each with its own unique properties. These consist of FeO (wüstite), Fe_3O_4 (magnetite) and four Fe_2O_3 polymorphs: α-Fe_2O_3 (hematite), β-Fe_2O_3 , γ-Fe_2O_3 (maghemite), and ϵ-Fe_2O_3.[1] The studies in this work will focus on magnetite and ϵ-Fe_2O_3.

1.3.1 Magnetite (Fe_3O_4)

Magnetite is amongst the oldest known magnetic materials and is the only stoichiometric iron oxide that contains both Fe^{3+} and Fe^{2+}.

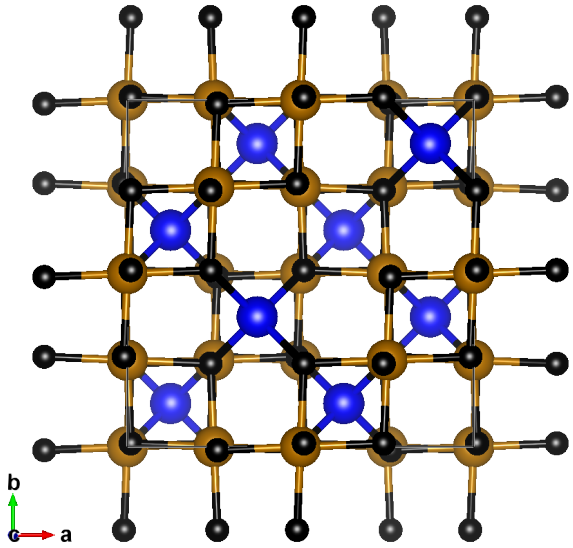

Figure 1.6: Structure of Fe_3O_4. T_d Fe are blue, O_h Fe are gold, and O are black.

Structure

At room temperature Fe_3O_4 is an inverse spinel of space group $Fd\bar{3}m$ with one O site and two distinct Fe sites as shown in figure 1.6. Tetrahedral (T_d) sites are occupied by Fe^{3+}, while octahedral (O_h) sites contain both Fe^{2+} and Fe^{3+}, resulting in the nominal cation distribution $(Fe^{3+})[Fe^{2+}Fe^{3+}]O_4$. Due to double exchange interactions and fast electron hopping between O_h sites, the effective cation distribution is $(Fe^{3+})[Fe^{2.5+}]_2O_4$.[27] At low temperatures ($<\sim$120 K), the structural symmetry is lowered and Fe_3O_4 becomes monoclinic with the $C2/c$ space group.[28,29]

The Verwey Transition

The Verwey transition was first discovered by Evert Verwey in 1939.[3] This phase transition is characterized by the simultaneous change in structure and electrical conductivity that occurs at $\sim$125 K where Fe_3O_4 transforms from a high temperature

inverse spinel semi-metal (from the O_h site electron hopping) to a monoclinic insulator. The structural changes have also been described by a freezing of phonon modes.[6] While this transition was originally attributed to charge ordering via alternating Fe^{2+} and Fe^{3+},[30] advances in experimental techniques and theoretical modelling have disproven this model.[4,5]

Instead, the concept of 'trimerons' has been proposed based on density functional theory (DFT) calculations[31] and the observed shortening of Fe-Fe distances between O_h sites (see figure 1.7).[6,32] Trimerons are quasiparticles created by the delocalization of t_{2g} electrons from a central Fe^{2+} ion to two acceptor ions resulting in orbital order within the three Fe sites.[33] The atomic shifts from trimeron formation are associated

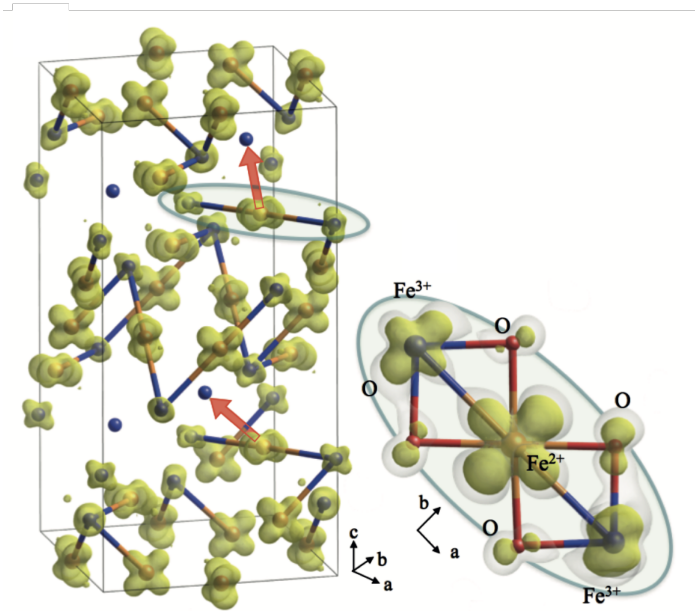

Figure 1.7: Trimeron structure formed by orbital ordering in Fe_3O_4, where red arrows indicate electric dipole moments. Schematic of a single trimeron highlights the Fe-O hybridization. Reproduced with permission from K Yamauchi, and P Barone. Journal of Physics: Condensed Matter, 26(10):103201, 2014. Copyright IOP Publishing. All rights reserved.

with the freezing of the Δ_5 and X_1 phonon modes and impact the (001) and (110) Bragg reflections.[34] Both NMR and pump-probe experiments support the existence of this orbital ordering in the low temperature insulating phase.[34,35]

1.3.2 ϵ-Fe_2O_3

Of the iron oxide polymorphs, ϵ-Fe_2O_3 is amongst the least understood. This phase was first reported in 1934;[36] however, progress was relatively limited in subsequent decades[37,38] because preparation of single phase samples remained an obstacle. Discovery that the ϵ phase could be stabilized using a silica matrix in the late 1990's[39] represented significant progress and generated increased interest in ϵ-Fe_2O_3.

The challenges in producing ϵ-Fe_2O_3 samples originate in its metastable nature. This phase of iron oxide occurs between γ-Fe_2O_3 (maghemite) and the thermodynamically stable α-Fe_2O_3 (hematite). Notably, ϵ-Fe_2O_3 is only stable in the nanoscale. It has been proposed that this limitation is due to the relatively low surface energy of ϵ-Fe_2O_3;[10] however further investigation into the $\gamma \rightarrow \epsilon$ transformation above 700°C is necessary.[40]

Structure

ϵ-Fe_2O_3 is an orthorhombic perovskite of space group $Pna2_1$, composed of four Fe sites and six O sites as shown in figure 1.8a and tabulated in table 1.1.[41] The Fe sites consist of two distorted octahedra (DO_h), called such for the increased variance in Fe-O bond lengths, one regular octahedra (RO_h) and one tetrahedra (T_d).[10,39,41] Both the DO_{h1} and RO_h sites form edge-shared octahedral chains along the a-axis as shown in figure 1.8b.

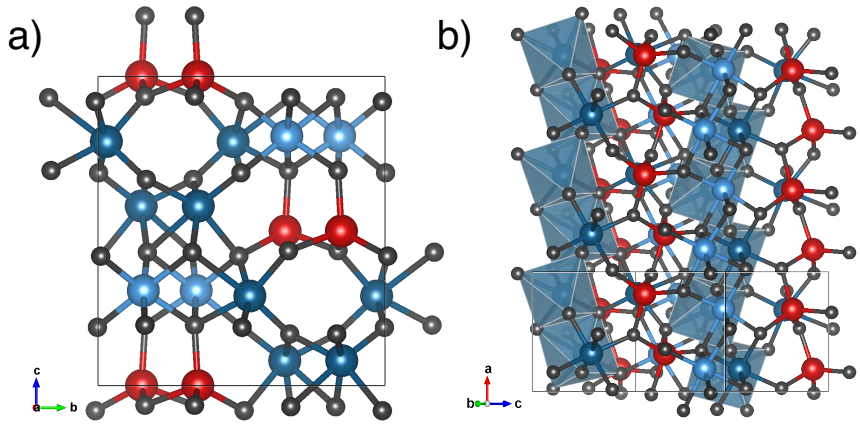

Figure 1.8: a) Structure of ϵ-Fe_2O_3 composed of DO_h (dark blue), RO_h (light blue) and T_d (red) sites. b) Structure of ϵ-Fe_2O_3 showing formation of edge-shared DO_{h1} octahedral chains along a-axis.

Table 1.1: Atomic positions for ϵ-Fe_2O_3 with space group $Pna2_1$.

Atom	x	y	z
Fe1 (DO_{h1})	0.67904	0.84309	0.00000
Fe2 (DO_{h2})	0.20010	0.35191	0.77193
Fe3 (T_d)	0.81084	0.65813	0.69060
Fe4 (RO_h)	0.68562	0.46366	0.98392
O1	0.34250	0.84459	0.89107
O2	0.00153	0.48512	0.63848
O3	0.46636	0.67871	0.63941
O4	0.55053	0.65394	0.10864
O5	0.85091	0.33322	0.85814
O6	0.34318	0.50802	0.89220

Magnetism

At room temperature, ϵ-Fe_2O_3 is a weak ferrimagnet with net moment along the a-axis, an enormous coercivity ($\mu_0 H_C$) of ~2 T, and magnetoelectric coupling.[42,43] However, the collinearity and origin of the net magnetic moment is not understood. Two proposed configurations are shown in figure 1.9. In the collinear model, supported by neutron diffraction, the magnetic moments along the a-axis are $m_{DOh1} = -3.9\mu_B$, $m_{DOh2} = +3.9\mu_B$, $m_{Td} = -2.4\mu_b$, and $m_{ROh} = +3.7\mu_B$.[41] Together this yields a net magnetization of $0.3\mu_B$ per Fe^{3+}, due to the uncompensated moments between T_d and RO_h sites. The origin of the reduced T_d moment is unknown. The authors of this report do note that their data also supports a small canting of m_{Td} and m_{ROh}, and so does not exclude the possibility of a non-collinear magnetic model. In the non-collinear magnetic model, the O_h sites have nearly collinear magnetization, while the T_d site is misaligned and possibly disordered.[39] In this model, the net magnetic moment arises from the geometric compensation of T_d sites. Recent density functional theory simulations have attempted to identify the magnetic ground state of

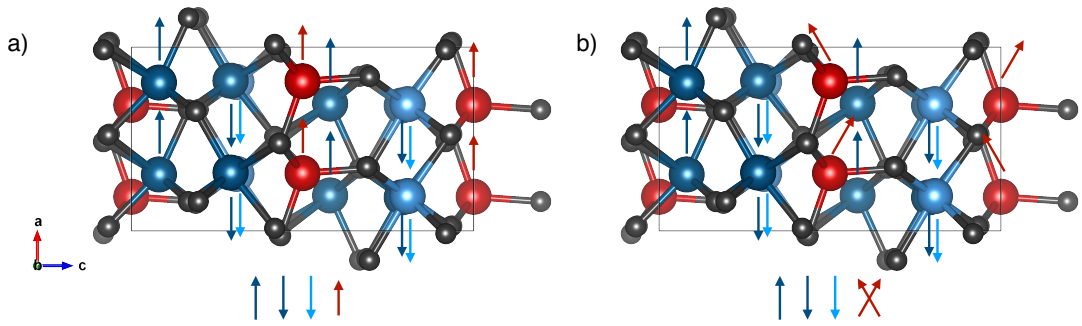

Figure 1.9: Possible a) collinear and b) non-collinear magnetic structures of ϵ-Fe_2O_3. Magnetic moments of DO_h (dark blue), RO_h (light blue) and T_d (red) sites indicated by arrows.

ferrimagnetic ϵ-Fe_2O_3;[44] however, inconsistencies between experimental results and the setup of these simulations make the overall conclusions less trustworthy.

Like many other perovskites,[45] ϵ-Fe_2O_3 exhibits a magnetic transition. Below ~80 K, it has an square wave incommensurate magnetic structure with reduced anisotropy.[41] The physics that underpin this transition is currently unresolved.

Conflicting Local Electronic Environment Reports

In addition to the open questions concerning the collinearity of the high temperature ferrimagnetic phase and the physics behind the magnetic transition, reports of the local electronic environment around the Fe sites of ϵ-Fe_2O_3 often conflict. Though overall magnetic properties such as the low field susceptibility (χ_{DC}) and $\mu_0 H_C$ show very similar temperature dependent behaviours, hyperfine parameters obtained via Mössbauer spectroscopy reveal significant differences, particularly in the quadrupole splittings (Δ) that measure the charge symmetry from the O-ligand fields about the Fe ions. Spectra even show the transition temperature itself changes with respect to the overall, long-range system's magnetism.[41,46–49] This variability has made the connection between bulk properties, microstructural effects (e.g. stress, strain, bonding disorder etc.) and local properties unclear, particularly because the fitting of Mössbauer spectra is model independent. One confounding factor is the samples themselves. Because a variety of synthesis methods have been used, each impacts the resulting structure-composition-magnetism inter-relations of the measured nanoparticles differently (especially with the sometimes unavoidable presence of the other iron oxide polymorphs). A more systematic study of ϵ-Fe_2O_3 nanoparticles is necessary to

decouple the impacts of structure and composition, and identify the local electronic environment of this phase.

1.4 Crystal Field Theory and Jahn-Teller Distortion

Crystal field theory describes how the orbital degeneracy of transition metal ions is broken by crystal field effects. Because electrons are filled from lower to higher energy orbitals, such effects determine the electronic configuration of individual ions which impacts the electronic and magnetic interactions within a material. The crystal field splitting energy (Δ) is the energy difference that appears between orbitals oriented between the ligands and those oriented towards the ligands. Thus ions with octahedral coordination have lower energy t_{2g} orbitals, while ions with tetrahedral coordination

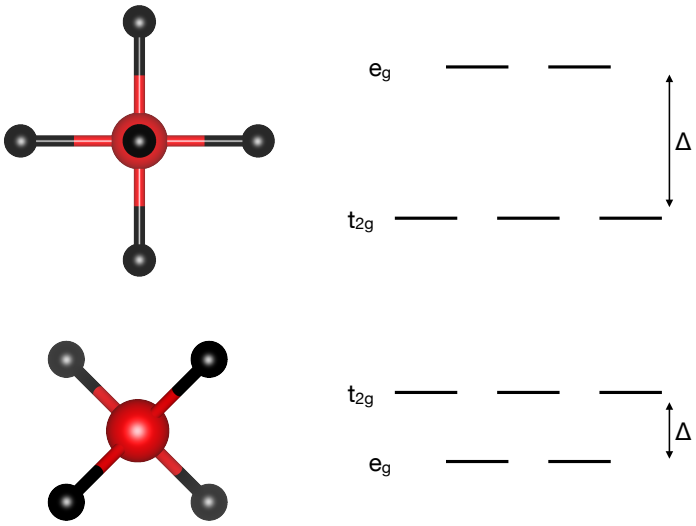

Figure 1.10: Effect of crystal field effects on ions in octahedral (top) and tetrahedral (bottom) coordination. Crystal field splitting energy Δ separates the t_{2g} and e_g orbitals.

have lower energy e_g orbitals (see figure 1.10). In tetrahedral coordination, Δ is 4/9 of Δ for octahedral coordination. The spin state of an ion is determined by the relationship between Δ and the energy required to pair electrons (P). If $\Delta < P$, then a high spin state is favoured, while $\Delta > P$ favours a low spin state. The reduced Δ of tetrahedrally coordinated ions typically results in high spin states. In both Fe_3O_4 and ϵ-Fe_2O_3, all of the Fe ions are in a high spin state.

Note that while crystal field splitting reduces orbital degeneracy, it does not lift it completely. Depending on both the number of valence electrons and the spin state, a situation may occur where orbitals of equal energy are unequally occupied. This electron configuration is unfavourable, and so a Jahn-Teller distortion often occurs to lift the orbital degeneracy via either the compression or expansion of some ligand bonds. Weak Jahn-Teller distortions occur for uneven occupation of t_{2g} orbitals, while strong Jahn-Teller distortions occur for uneven occupation of e_g orbitals. High spin Mn^{3+} (d^4) is the archetypal Jahn-Teller active ion, known for exhibiting strong Jahn-Teller distortions. For the iron oxides of interest, only the Fe^{2+} ions in Fe_3O_4 are Jahn-Teller active (albeit weakly), while the Fe^{3+} ions are Jahn-Teller inactive.

1.5 Multiferroicity

Multiferroic materials simultaneously exhibit at least two types of ordering (magnetism, electricity, elasticity, toroidicity).[50] These materials are fascinating because the coupling between orderings has great potential for a wide range of applications. Magnetoelectrics are of particular interest because the interplay between magnetism and electricity can allow the manipulation of spin with electricity and charge with

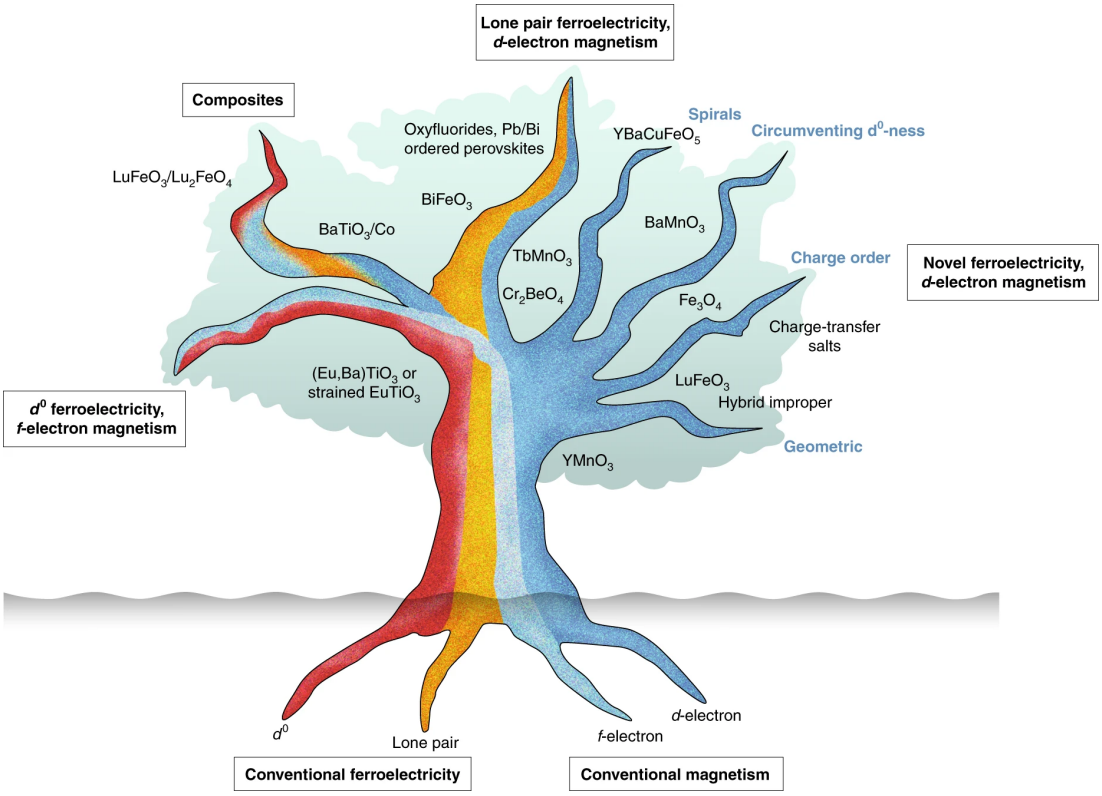

Figure 1.11: Magnetoelectric "family tree" showing how the origins of conventional ferroelectricity and magnetism combine to form magnetoelectric materials. Reproduced with permission from N Spandin and R Ramesh. Nature Materials, 18(3):203–212, 2019. Copyright Springer Nature BV.

magnetism.[51] Such control would represent a significant advance for magnetic recording and spintronics applications. However; ferromagnetism and ferroelectricity tend to be mutually exclusive.[52]

The requirements for magnetism are straightforward, with a magnetic moment occurring for partially filled d or f orbitals. In contrast, the origins of ferroelectricity are more complicated. Though different mechanisms have been determined, the underlying physics is not well understood.[53] 'Conventional' ferroelectricity occurs via two mechanisms: d^0 or lone pairs configurations, both of which significantly limit the

number of possible magnetoelectrics. In contrast, 'novel' ferroelectricity can originate from structural distortion, charge and magnetic ordering etc., creating opportunities for more materials.[51,53] Figure 1.11 shows how ferroelectricity and magnetism combine in magnetoelectric materials.[54] Because most single phase multiferroics are rare-earth (R) transition metal (M) perovskites (RMO_3), this general structure will be used to discuss some of the different mechanisms behind magnetoelectricity.

For the d^0 configuration, ferroelectricity occurs because the hybridization of electron clouds of neighbouring M ions allows for off-centred ions. This type of displacive ferroelectricity is favourable when the d shell is empty and electrons are highly localized.[55] For example, in $BaTiO_3$ the empty d states of Ti^{4+} establish strong pd covalency with some of the neighbouring O ions, causing the Ti ion to shift from the centre of the O_6 octahedra.[53] This shift causes the broken symmetry necessary for ferroelectricity. By contrast, in the lone pairs configuration there is no restriction on the valence of M ions. Instead, the broken spatial symmetry is caused by the anisotropic distribution of unpaired valence electrons from R. The most notable lone pair multiferroics are $BiFeO_3$ and $BiMnO_3$, where a pair of $6s$ electrons from Bi^{3+} do not participate in sp-hybridization, and are free to create a local dipole moment.

The origins of novel ferroelectricity are more varied and less predictable than that of conventional ferroelectricity. Geometric structural distortions have been shown to cause ferroelectricity in some materials such as hexagonal manganites. However, because this ordering tends to be due to polyhedral rotations, it is less responsive to switching than conventional ferroelectricity. Charge ordering is another novel mechanism, although much of the interest appears to be focused on organic-based

multiferroics. Finally, and perhaps most interestingly, magnetic ordering has also been shown to induce ferroelectricity. Such a mechanism is appealing because the magnetoelectric coupling is particularly strong.[53,54]

Chapter 2

Experimental Methods

2.1 Nanoparticle Synthesis

2.1.1 Fe_3O_4 Nanorods

Three different sizes of Fe_3O_4 nanorods were synthesized. The smallest nanorods were prepared via the solvothermal decomposition of $Fe(CO)_5$.[56] First a solution containing 1.2 g hexadecylamine (technical grade, 90%, Aldrich), 4 ml oleic acid (99%, Alfa Aesar) and 16 ml 1-octanol (99%, Alfa Aesar) was heated to 55°C and stirred for 30 minutes. The solution was cooled to room temperature, 4 ml $Fe(CO)_5$ (Acros Organics) was added, and the solution was stirred for an additional 60 min. The entire solution was transferred into the Teflon liner of a 45 ml Parr acid digestion vessel, sealed and placed in a 200°C box furnace for six hours. The resulting particles were separated magnetically and washed in ethanol.

Both the medium and large Fe_3O_4 nanorods were synthesized via a two-step process where β-FeOOH were prepared via hydrothermal decomposition, then reduced

to Fe_3O_4 in oleylamine. To prepare the medium-sized β-FeOOH nanorods, 4.3248 g of $FeCl_3 \cdot 6H_2O$ (ACS grade, Fisher Scientific) and 0.16 g polyethylenimine (branched, 800 M_w, Aldrich) were dissolved in 80 ml DI water.[57] Only 38 ml of solution was poured into a digestion vessel, sealed and placed in a 110°C box furnace for seven hours. The resulting particles were recovered via centrifugation, washed in ethanol and dried in a 50°C box furnace overnight.

To prepare the large β-FeOOH nanorods, 9.4602 g of $FeCl_3 \cdot 6H_2O$ and 2.1 g of urea (ACS grade, Fisher Scientific) were dissolved in 35 ml DI water.[58] The entire solution was poured into a digestion vessel, 5 ml removed, and the vessel sealed and placed into a 125° box furnace for four hours. The resulting particles were recovered via centrifugation, washed in ethanol and dried in a 50°C box furnace overnight.

To convert the β-FeOOH nanorods into Fe_3O_4 nanorods, the β-FeOOH nanorods were suspended in 50 ml oleylamine (70% technical grade, Aldrich) and heated to 210°C in an argon atmosphere under reflux conditions for two hours. The resulting particles were separated magnetically and washed extensively; first in hexanes and acetone, then ethanol, and finally methanol. The nanoparticles were dried in a 50°C box furnace overnight.

2.1.2 ϵ-Fe_2O_3 Nanoparticles

ϵ-Fe_2O_3 nanoparticles were synthesized by annealing an iron-impregnated silica gel.[59,60] To prepare the gel, 0.84 ml DI water and 3.9 ml reagent alcohol (ACS grade, Fisher Scientific) were stirred together for 5 min at 350 RPM before 1.590 g $Fe(NO)_3$-$9H_2O$ (98+%, Acros Organics) was added. Once fully dissolved, 3 ml TEOS (98%, Alfa

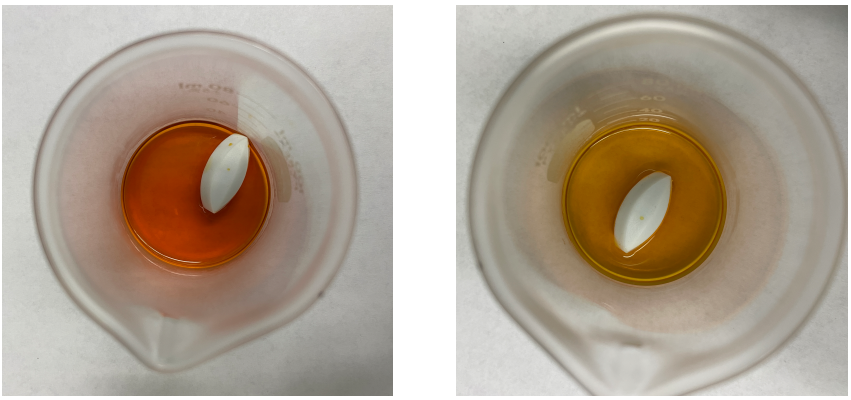

Figure 2.1: $FeCl_3$ solution (left) before and (right) after TEOS addition

Aesar) was added dropwise under stirring conditions over ∼10 min causing the solution to noticeably lighten in colour as shown in figure 2.1. After TEOS addition, the beaker was covered and stirred for 20 min. The solution was divided between two 6 cm diameter glass Petri dishes, covered, and placed in a 40°C furnace for two days. The Petri dishes were monitored during this period to ensure that the dishes remained unsealed and films were drying.

Resulting gels were ground using an agate mortar and pestle and placed in an alumina crucible for annealing in a Thermolyne 79300 tube furnace in air. Gels were heated at 3°C/min to 60°C, held for 60 min, heated at 3°C/min to 450°C, then heated at 1°C/min to 1100°C where it was held for 180 min. After the set time elapsed, the furnace turned off and cooled naturally. The sample progression is shown in figure 2.2. To prepare larger nanoparticles, the maximum temperature was increased while the dwell time was adjusted such that the annealing time was equal for all samples. Thus the 1150°C and 1200°C samples were held for 130 min and 80 min, respectively.

While the silica matrix is necessary to stabilize the nanoparticle phase during

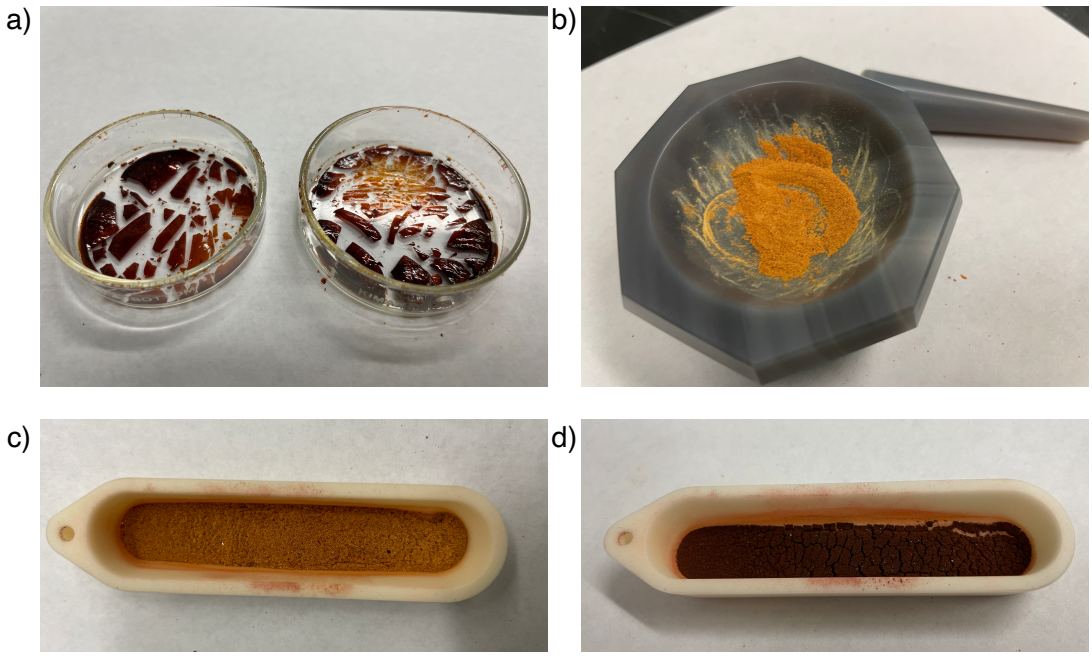

Figure 2.2: Fe-impregnated SiO_2 gel after a) drying and b) grinding. Alumina crucible with c) Fe-impregnated SiO_2 before annealing and d) SiO_2-coated ϵ-Fe_2O_3 nanoparticles after annealing.

synthesis, removal is required to facilitate sample characterization. Silica etching was achieved by refluxing the annealed ϵ-Fe_2O_3-SiO_2 samples in an excess of 12 M NaOH for 18 h. The resulting sample was divided amongst six test tubes, centrifuged and washed thoroughly with DI water until nanoparticles remained suspended in solution. Then 100 μl of glacial acetic acid (99.7%, Alfa Aesar) was added to each test tube to neutralize any remaining NaOH. After 30 min, two test tubes of solution were divided amongst three new tubes, filled with acetone and centrifuged. The process was repeated with the remaining four tubes to yield three test tubes containing all of the etched nanoparticles. These were washed twice using a ~1:4 water:acetone solution and twice with acetone before drying.

Transition metal doped ϵ-Fe_2O_3 nanoparticles were prepared using the same method

Table 2.1: Transition-metal (M) doped ϵ-Fe_2O_3 nanoparticle samples prepared for this work. Percentage denotes fraction of M substituted for Fe ions in the synthesis.

Dopant (M)	0.5%	1%	2%	3%	4%	6%	8%	9%	12%
Cr	–	x	x	–	x	x	–	x	x
Mn	–	x	x	–	x	x	x	–	x
Co	x	x	x	–	x	–	–	–	–
Ni	x	x	x	–	x	–	–	–	–
Cu	x	x	x	x	x	–	–	–	–
Zn	–	x	x	x	x	x	–	–	–

described in section 2.1.2. To incorporate the dopant a fraction of the Fe ions were replaced with an equivalent amount of transition metal ions in the form of a hydrated nitrate salt in the preparation of the impregnated SiO_2 gel. Low levels of doping (<4%) were prepared initially, and the doping level was increased until x-ray diffraction patterns deviated from that of the undoped ϵ-Fe_2O_3. Table 2.1 lists the samples that were prepared.

2.2 Powder x-ray diffraction

X-ray diffraction (XRD) provides information about crystal structure. Incident x-rays scatter off of the electrons that surround each ion in the lattice, and the constructive interference of these scattered waves form a diffraction pattern. The Bragg equation relates the periodic spacing between hkl planes (d_{hkl}), diffraction angle θ, and x-ray wavelength λ as

$$n\lambda = 2d_{hkl}\sin\theta_{hkl} \tag{2.1}$$

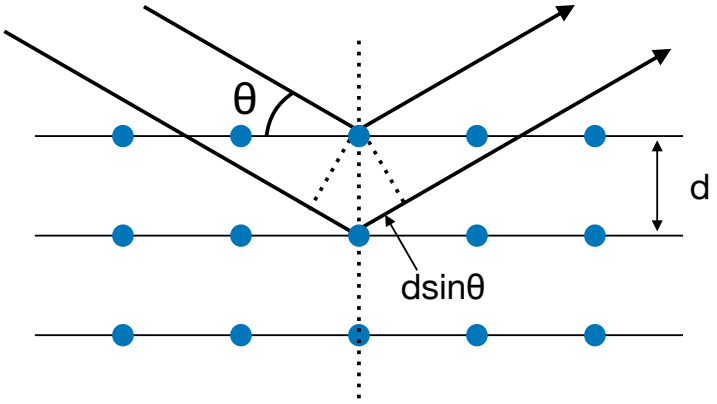

Figure 2.3: Schematic of Bragg diffraction.

where n is an integer. Figure 2.3 shows a schematic of Bragg diffraction. For an infinitely large crystal, the width of the diffraction patterns peaks is determined by instrumental factors; however, finite size effects lead to broadened peaks in smaller crystallites. The Scherrer equation relates the average crystallite size τ to the broadening as

$$\tau = \frac{K\lambda}{\beta \cos\theta} \tag{2.2}$$

where K is a dimensionless shape factor (0.9 for spherical particles), λ is the x-ray wavelength, β is the full width at half maximum of the intensity in radians, and θ is the Bragg angle.

XRD patterns were collected to determine the structure of the nanoparticles. All patterns were collected using a Bruker D8 DaVinci in Bragg-Brentano geometry with Cu-K_α radiation. The x-ray tube consists of an electrically heated tungsten cathode which produces electrons that are accelerated to the Cu anode target by a large potential difference (40 eV). When the tube current (40 mA) strikes the target, characteristic Cu x-rays and Bremsstrahlung radiation are generated, exiting the tube

through the Be window. The primary optics are configured to focus the x-ray beam on the sample surface, while secondary optics focus the diffracted x-rays on the detector. A Ni filter on the secondary optics is used to attenuate the Bremsstrahlung and Cu K_β x-rays. A Lynxeye linear Si strip detector was used to detect the diffracted x-rays. Incident x-rays cause photoionization resulting in electron-hole pairs which are measured using a bias voltage. To reduce the effects of fluorescent radiation produced by excitation of the Fe K-shell (7 keV) electrons by the Cu K_α x-rays (8.04 keV), a minimum energy threshold is set in the diffractometer software.

XRD patterns were collected using dried nanoparticle samples on a zero-background quartz slide. Room temperature measurements used a rotating stage, while low temperature measurements used an Oxford Cryosystems Phenix closed cycle refrigeration stage. Rietveld refinements to obtain lattice parameters, average crystallite sizes and strain analysis were performed using FullProf and GSAS-II.[61,62]

2.3 Transmission electron microscopy

Transmission electron microscopy (TEM) is a characterization technique that uses an high energy beam of electrons for imaging and diffraction. Electrons are emitted using a field emission electron gun, which is designed to deliver a bright coherent beam of electrons. The beam is focused through a multistage condensing system before interacting with the sample. Because electrons interact strongly with matter, only thin samples can be imaged using a TEM. Depending on the imaging mode used, different information can be obtained. For comprehensive discussion of TEM, the reader is referred to Reference.[63]

In bright-field mode, the transmitted beam of electrons is used to generate an image of the sample. Here the beam of electrons can be treated as particles, where the interaction depends on the mass thickness (proportional to the density and thickness) and the material composition (proportional to the atomic number (Z)) of the sample. As a result, TEM bright field images provide information about nanoparticle morphology and composition.

The TEM can also be operated in scanning transmission electron microscopy (STEM) mode. Unlike conventional modes where the images area is fully illuminated, STEM mode uses a tightly focused beam that is rastered across the sample. For typical high angle annular dark field (HAADF) images, the image is formed by electrons scattered to high angles from the sample. As a result, HAADF images are very sensitive to Z. STEM mode is also used for energy dispersive spectroscopy (EDS), which measures the characteristic x-rays excited by the electron beam. EDS detectors are based on semi-conductor chips that measure the current produced by the formation of electron-hole pairs generated by the incoming x-rays.[64] In this manner, both the intensity and energy of the x-rays can be detected, producing a spectrum that corresponds to the composition of the sampled region. By performing EDS measurements while rastering the beam across the sample in STEM mode a full compositional map can be produced.

Nanoparticles were suspended in chloroform and dropped onto a 200-mesh carbon-coated copper grid. TEM images were collected on a FEI Talos F200X S/TEM at the Manitoba Institute of Materials (MIM) using a 200 kV accelerating voltage. Bright field images were acquired using the Ceta-D scintillator-based camera, while EDS

measurements used the Super-X integrated EDS system composed of four individual detectors. Bright field images were analyzed using ImageJ[65] to determine particle size distributions.

Additional high resolution TEM (HRTEM) and STEM images of the Fe_3O_4 nanorods were collected using a JEOL ARM-200TH at 200 keV by Prof. C. Ouyang, C.-C. Chi, and A. Ranjan at National Tsing Hua University in Taiwan. They also performed image analysis and structural simulations using Java Electron Microscope Simulation (JEMS)[66] with Fe_3O_4 structural parameters from ICDD. This analysis uses the multislice method where the *ab initio* simulations used the Vienna *ab initio* simulation package (VASP) based on first principals density functional theory with the generalized gradient approximation (DFT-GGA).[67] Lattice parameters were determined by adjusting the shape and radius of the simulated pattern to fit the experimental diffraction obtained from the fast-fourier transform (FFT) of the HRTEM image. Lattice strain is calculated using $\Delta a/a_0$ where a_0 is the lattice parameter of bulk Fe_3O_4.

2.4 Overall magnetism

Magnetic properties were measured using a superconducting quantum interference device (SQUID)-based magnetic properties measurement system by Quantum Design (shown in figure 2.4). This system combines temperature and magnet control capabilities with a sensitive amplifier system to measure magnetization and magnetic susceptibility of materials. The magnetic fields are generated by a superconducting magnet wound into a solenoid. This magnet is designed to be a closed superconducting loop so that it can be charged to the desired current and then operated

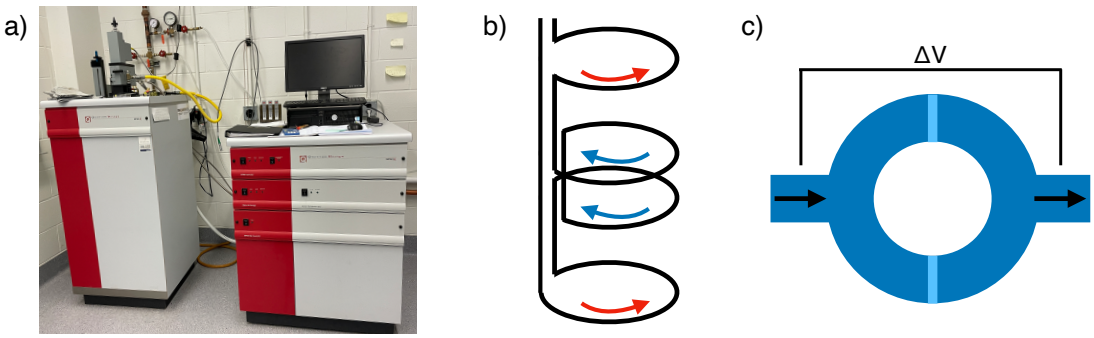

Figure 2.4: a) Quantum Design MPMS XL-5. b) Superconducting detector coils in second-order gradiometer configuration with clockwise windings shown in red and counter clockwise windings in blue. c) SQUID device containing two Josephson junctions (light blue) where voltage across device produces output signal.

in persistent mode. During a measurement, the sample is moved through a set of superconducting detection coils (located outside of the sample chamber and in the centre of the magnet). The detection coils are a single superconducting wire wound as shown in figure 2.4 into three coils that function as a second-order gradiometer. This particular configuration is used to minimize noise caused by fluctuations of the superconducting magnet, and is well-suited to minimize background drifts caused by the relaxation of the applied magnetic field. As the sample travels through the detection coils, the magnetic moment of the sample inductively couples to the coils and generates an electric current. This generated current is proportional to the change in magnetic flux within the detection coils. The signal from the detection coils is transmitted to the SQUID through superconducting wires.

The SQUID consists of a closed superconducting loop with two Josephson junctions (see figure 2.4) located below the magnet inside a superconducting shield. This shielding is necessary because the SQUID is extremely sensitive to magnetic field fluc-

tuations –both from those of the superconducting magnet in the instrument and any external fields present in the laboratory. The SQUID receives the current from the detection coils and converts it to an output voltage. Since both the detector coils and SQUID have linear response, the final output voltage is directly proportional to the magnetic moment of the sample. Thus as the sample is moved through the magnet and detection coils, the data recorded is of voltage response vs sample position. The computer can then fit the acquired signal to that of a theoretical magnetic dipole to determine the magnetization of the sample.

Preliminary measurements were performed on ϵ-Fe_2O_3 powder samples mounted in gel caps; however, measurement irreproducibility and significantly smaller than expected values of $\mu_0 H_C$ were evident. Because interparticle interactions were suspected, dilutions of nanoparticles in paraffin were prepared. As no concentration dependence was detected and the phase is known to exhibit substantial $\mu_0 H_C$, physical movement of the particles was suspected. Thus magnetometry samples were prepared by placing a known mass of nanoparticles into a gel cap, then saturating the powder with hot paraffin. Full paraffin saturation was evidenced by the darkening of the sample. Note that fixation in paraffin limits the measuring temperature to <320 K. Zero-field-cooled (ZFC)/field-cooled (FC) DC susceptibility measurements (χ_{DC}) were done on virgin samples by cooling from 300 to 10 K, then measuring using 50 Oe applied field. Hysteresis loops were measured from 10 to 300 K in 50 kOe after cooling a 0 Oe field (having quenched the magnet at 300 K beforehand).

2.5 Mössbauer spectroscopy

Mössbauer spectroscopy uses the Mössbauer effect, discovered in 1958 by Rudolf Mössbauer,[68] to probe the local environment of atoms in a sample. This effect is defined by the recoil-free absorption and emission of γ-radiation by atomic nuclei in a solid. For a full references, see 69, 70.

Experiments based on technique typically utilize γ rays emitted from a radioactive nucleus as it transitions from excited state E_e to ground state E_g, where the change

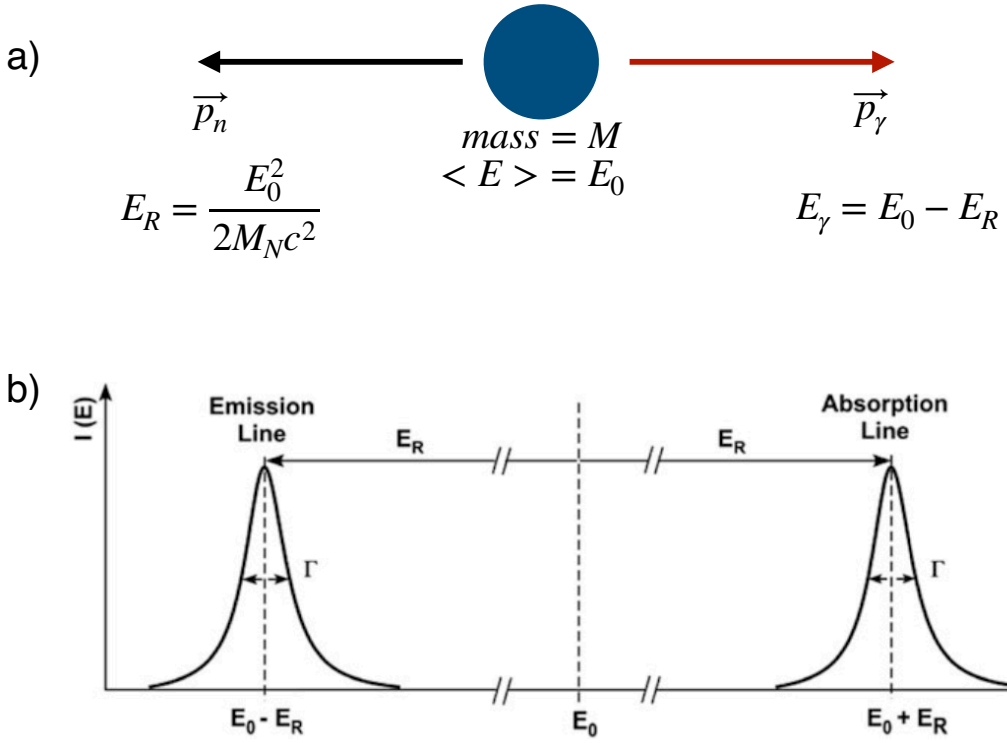

Figure 2.5: a) Recoil energy (E_R) and momentum (p_n) of a free atom after ejection of a γ-ray. b) Energy separation of γ-ray emission and absorption lines caused by recoil of free atom. Reprinted figure from P Gütlich, E Bill, and A Trautwein. Mössbauer spectroscopy and transition metal chemistry, 2010. Copyright Springer Nature.

in energy is $E_0 = E_e - E_g$. If the nucleus is unbound, then it will experience a loss in energy due to recoil of

$$E_R = \frac{E_\gamma^2}{2M_N c^2} \tag{2.3}$$

where E_γ is the energy of the emitted photon, M is the mass of the recoiling object and c is the speed of light. Here a non-relativistic approximation is used because of the large mass of the nucleus and low recoil velocity. This recoil will also affect the absorption of γ-rays, since

$$E_\gamma = E_0 - E_R \tag{2.4}$$

Since E_R is very small compared to E_0, $E_\gamma \simeq E_0$ can be used in Equation 2.3. This can be shown numerically since for ^{57}Fe, E_0=14.4 keV and E_R=1.95 meV. Note that E_R will also impact the absorption of a γ-ray, requiring $E_\gamma = E_0 + E_R$ to excite the ground state. As a result, the Mössbauer effect where a γ-ray is absorbed and then emitted with the same energy is not possible for a nucleus at rest due to energy loss by recoil.

Of course, from Heisenberg's uncertainty principle, the precise energy E_0 of an excited state with finite lifetime τ cannot be determined exactly. The physical consequence is that the energy E of γ-rays emitted from an ensemble of fixed nuclei will be distributed around E_0. This distribution is a Lorentzian with full-width at half maximum (FWHM) Γ_{nat}, where the natural line width is related to the half life of the excited state by $\Gamma_{nat} = \hbar/\tau_{1/2}$. For recoil-free absorption and emission to occur, $\Gamma_{nat} > 2E_R$, as shown in figure 2.5b.

For free nuclei, E_R is nearly six orders of magnitude larger than Γ_{nat}, making the probability of resonant fluorescence incredibly low. This probability increases if the

nucleus becomes bound to a matrix where the recoil momentum becomes distributed throughout the entire crystallite causing E_R to become negligible. Provided that no phonon annihilation or creation occurs (which would split the absorption and emission energies), the probability of resonant absorption and emission is given by the f-factor (Lamb-Mössbauer factor) as

$$f = exp[-E_\gamma^2 \langle x^2 \rangle / (\hbar c)^2] \tag{2.5}$$

where $\langle x^2 \rangle$ is the mean square vibrational amplitude of the emitting atom in the direction of the emitted photon. This is analogous to the Debye-Waller factor for Bragg x-ray scattering where the solid's phonon modes are described by the Debye model. Because the mean-squared displacement ($\langle x^2 \rangle$) increases with temperature, the f-factor decreases as temperature increases, with the rate of decrease dictated by the absorber's Debye temperature (Θ_D).

In a Mössbauer experiment, a spectrum is collected by measuring the transmission of Doppler-shifted γ-rays through a sample. For the study of ^{57}Fe, a radioactive ^{57}Co source is moved relative to the absorber producing Doppler-shifted γ-rays to excite transitions in the absorber nuclei whose energies are shifted from E_0 by hyperfine interactions. The γ-rays with energy equal to these shifted nuclear transitions will be absorbed and the Mössbauer spectrum is collected by detecting the transmitted γ-rays as a function of Doppler-shifted source velocity. The amount of resonant nuclear γ-ray absorption is determined by the overlap between the shifted emission line and the absorption line, where maximum absorption occurs when the lines completely overlap. The line shape of the spectral line is a convolution of the emission and

absorption lines.

Mössbauer spectroscopy is insightful because the perturbed energy states evidenced in the spectra speak to nuclear hyperfine interactions. The three types of hyperfine interactions to be considered are the nuclear charge density, the electric field gradient, and the nuclear hyperfine field.[71]

The nuclear charge density is related to the isomer shift (δ) via the centroid shift of the Mössbauer spectrum. This parameter is the result of the intrinsic isomer shift (δ_I) from the electric monopole interaction and the second-order Doppler shift (δ_{SOD}) from relativistic thermal effects of the emitting and absorbing nuclei. The intrinsic

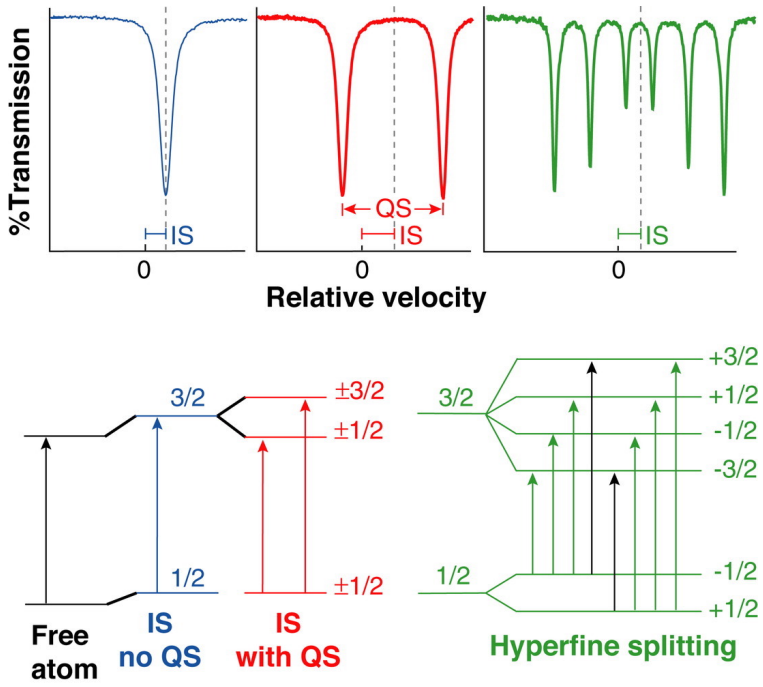

Figure 2.6: Schematic showing impact of hyperfine parameters (isomer shift (IS) and quadrupole splitting (QS)) on Mössbauer spectrum. Forbidden Zeeman transitions shown with black arrows in hyperfine splitting diagram. Reproduced with permission from Dyar et al, Annu. Rev. Earth Planet. Sci., 34:83–125, 2006. Copyright Annual Reviews, Inc.

isomer shift is caused by differences in s-electron density between the source and the absorber

$$\delta_I = \frac{2\pi}{5} Ze^2\{|\psi_s(0)_A|^2 - |\psi_s(0)_S|^2\}\{R_e^2 - R_g^2\} \tag{2.6}$$

where Z is the atomic number, e is the charge of an electron, $|\psi_s(0)_A|^2$ and $|\psi_s(0)_B|^2$ are the s-orbital electron densities of the absorbing nuclei and source nuclei respectively, and R_e and R_g are the radii of the nuclei in the excited and ground states. Since $R_e < R_g$ for ^{57}Fe, an increase in s-orbital density causes δ_I to decrease. The second-order Doppler shift is related to the mean square velocity ($\langle v^2 \rangle$) of the Mössbauer nuclei, similar to the f-factor, which was related to $\langle x^2 \rangle$. As such, δ_{SOD} can also be described by the Debye model with the rate of decrease controlled by Θ_D.

Information about the electric field gradient is provided via the quadrupole splitting (Δ). The quadrupole splitting occurs because $2I+1$ magnetic substates (m_I) will form in a state with spin quantum number I when exposed to an electric field gradient. Because states with $|m_I|$ are degenerate, only nuclear states with spin quantum number $I > 1/2$ have an observable quadrupole moment (Q). For ^{57}Fe, this means that the excited $I = 3/2$ state becomes becomes split into two states –measured experimentally as a doublet. In general, the energy of this splitting is given by

$$E_Q = \frac{eQV_{zz}}{4I(2I-1)}[3m_I^2 - I(I+1)]\sqrt{1 + \frac{\eta^2}{3}} \tag{2.7}$$

where $V_{zz} = \partial^2 V/\partial z^2$ is the principal component of the electric gradient field tensor, and η is the asymmetry parameter given by

$$\eta = \frac{V_{xx} - V_{yy}}{V_{zz}} \tag{2.8}$$

where V_{xx} and V_{yy} are the off diagonal elements and $0 \leq \eta \leq 1$. For the $I = 3/2$ state

of ^{57}Fe, the energy splitting simplifies to

$$E_Q = \frac{eQV_{zz}}{2}\sqrt{1+\frac{\eta^2}{3}} \tag{2.9}$$

Because $V_{zz} \propto r^{-3}$, the strongest contributor of E_Q are the valence electrons ($p-$ and $d-$orbitals) belonging to the Mössbauer atom; however, symmetry distortions, covalency effects and spin-orbit coupling all play a role.

Finally, the Mössbauer spectrum also provides information about the local magnetic field ($\vec{B}_{hf}$). The interaction between the nuclear spin ($\vec{I}$) and the magnetic moment ($\vec{\mu}$) with $\vec{B}_{hf}$ at the nucleus occurs via the Zeeman interaction as described by the Hamiltonian

$$\mathcal{H} = -\vec{\mu}\cdot\vec{B}_{hf} = -g_N\mu_N\vec{I}\cdot\vec{B}_{hf} \tag{2.10}$$

where g_N is the nuclear Landé factor and μ_N is the nuclear magneton. Thus the Zeeman interaction splits the states with $\vec{I}$ into equally spaced substates with nuclear energies

$$E_M = -g_N\mu_N m_I B_{hf} \tag{2.11}$$

where m_I is the nuclear magnetic spin quantum number.

In ^{57}Fe, the transition from $I = 1/2$ to $I = 3/2$ with selection rules $\Delta I = 1$ and $\Delta m_I = 0, \pm 1$ allows for six transitions as shown in figure 2.6, resulting in a sextet. For a randomly oriented powder (giving an isotropic distribution of the magnetic field relative to the direction of γ-ray propagation), the relative line intensities from the Clebsch-Gordan coefficients are 3:2:1:1:2:3.

There are a number of sources that contribute to B_{hf}. The isotropic Fermi contact field is the most significant, stemming from a net spin-up or spin-down s-electron

density at the nucleus caused by spin polarization by unpaired valence electrons. Other contributors to B_{hf} are caused by the orbital motion of the valence electrons and a non-spherical distribution of the electric spin density.

Figure 2.7 shows a typical Mössbauer spectrometer configuration. For the ^{57}Fe Mössbauer experiments in this thesis, a ^{57}Co source in Rh matrix is mounted on a Wissel MDU MR-360 transducer. A Wissel DFG-1200 digital function generator supplies a constant acceleration (triangle) waveform to the drive, producing the Doppler-shifted γ-rays that interact with the ^{57}Fe nuclei in the sample. A LND model 45431 Ar/Xe proportional counter located behind the sample detects γ-rays that are transmitted through the sample. This signal is amplified before processing with an ORTEC single channel analyzer (SCA), which generates a pulse when it detects a signal within a voltage window. This window is set using the SCA's upper and lower discriminators and chosen to detect only the 14.4 keV γ-rays. The output of the SCA is sent to the PC with an ORTEC multi-channel scaler (MCS) which sorts the

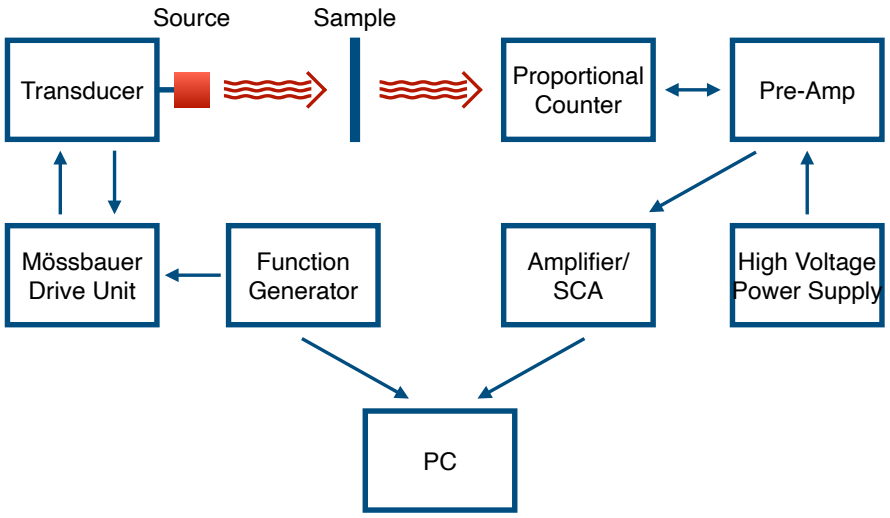

Figure 2.7: Schematic of typical Mössbauer spectrometer.

incoming data into channels. Each channel corresponds to a specific drive velocity, so the resulting Mössbauer spectrum is the number of transmitted γ-rays as a function of drive velocity.

The spectrometer is calibrated using 6 μm α-Fe foil, which has B_{hf} of 33 T at room temperature. All δ are reported relative to α-Fe at room temperature. Spectra were collected from 10 to 300 K using a Janis SHI-850 closed cycle refrigeration system of silica-free powder samples. A non-linear least squares analysis was applied to the spectra, where each Fe site is characterized by a Lorentzian sextet with the hyperfine parameters discussed above.

2.6 X-ray spectroscopy

X-ray spectroscopic techniques are amongst most useful for materials characterization due to their sensitivity and element specificity, and are most often performed at synchrotron facilities. In a synchrotron, electrons at relativistic energies are accelerated along a circular path. Each change in direction causes electromagnetic energy to be emitted with total intensity proportional to Γ^4 where $\Gamma = E_p/(mc^2)$ where E_p and m are the energy and mass of the electron and c is the speed of light. Thus the intensity of synchrotron radiation is high compared to conventional sources. This radiation is emitted tangentially from the particle beam, and directed for use through a beam port into a beam line and experimental end station.[72] Experiments utilizing lower energy ("soft") x-rays require the beam path to be under vacuum, while those with high energy ("hard") x-rays require end stations to be shielded (often through the use of lead-lined hutches).

2.6.1 Soft x-ray absorption spectroscopy

X-ray absorption spectroscopy (XAS) is a soft x-ray technique. It utilizes monochromatic x-rays to excite core electrons of the sample into empty valence holes. Such an excitation occurs when the incoming x-ray photons have sufficient energy to overcome the binding energy, making this an element-specific technique. Dipole selection rules limit the transitions between states to $\Delta L = \pm 1$ and $\Delta S = 0$, where L is the azimuthal quantum number and S is the spin quantum number. For a full derivation, the reader is directed to reference 73. The consequence of these selection rules is that s-orbital electrons can be excited into p-orbitals, while p-orbital electrons can be excited to both d- and s-orbitals.

There are three methods for measuring the XAS spectrum: transmission, electron

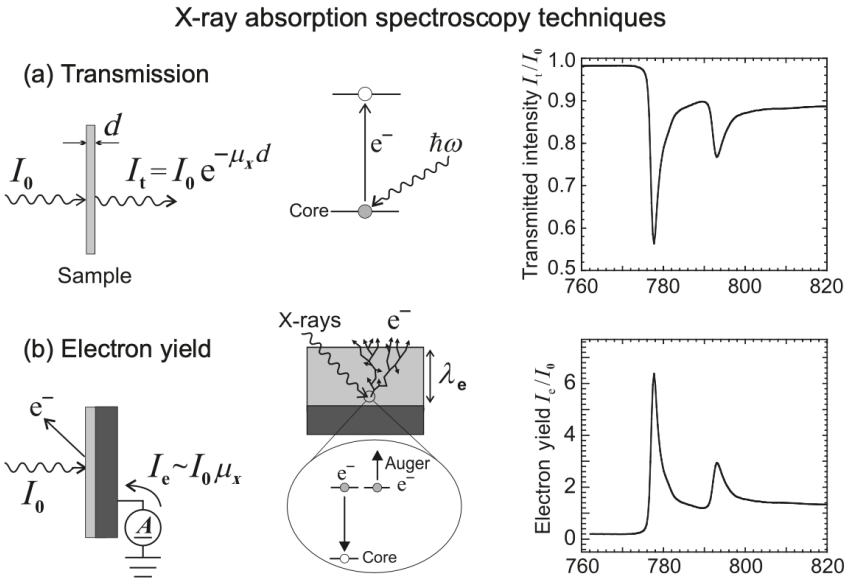

Figure 2.8: Comparison between a) transmission and b) electron yield methods for measuring x-ray absorption spectra. Reproduced with permission from J Stöhr and HC Siegmann, Magnetism. Solid-State Sciences. Springer, Berlin, Heidelberg, 5:236, 2006. Copyright Springer.

yield and fluorescence. In transmission mode shown in figure 2.8a, the experiment is set up where the incoming beam with incident intensity (I_0) passes through a thin sample with thickness d and linear x-ray coefficient μ_x, and the transmitted intensity (I_t) is detected. The relationship between the incident and transmitted beam is given by $I_t = I_0 e^{-\mu_x d}$. When the incident energy ($\hbar\omega$) becomes sufficient to excite a core electron to an empty state, a drop in I_t appears, corresponding to the quantized absorption edge. Typically I_t is normalized by I_0 to minimize the effect of incident beam fluctuations and the spectrum is presented as $\ln(I_0/I_t)$, making the presented data proportional to μ_x.

Electron yield mode measures the same process, though the detection takes advantage of different physics as shown in figure 2.8b. As in transmission mode, the incident x-ray beam causes the excitation of a core electron to a valence state creating a core-hole. This core hole is then filled by a valence electron causing the ejection of either a fluorescent x-ray or an Auger electron which generates a low energy cascade of electrons that travel to the surface of the material. Additional current will be generated by photoemission from the incident beam. This current (or total electron yield) is then measured using a picoammeter. Because the total number of electrons is proportional to the probability of Auger electron creation and the effective thickness of the sample is very thin ($d << 1/\mu_x$), the resulting signal I_e is directly proportional to $I_0\mu_x$. While this relationship seems to require very thin samples, most of the electron yield signal is only able to escape $\lambda_e \sim$5 nm.[74] Note that the x-ray absorption length $\lambda_x = 1/\mu_x$ (defined as the distance in the material where the intensity is reduced by $1/e$), depends on the photon energy and becomes shorter near absorption edges. For

the L_3 edge of Fe λ_x is ~500 nm before the edge, ~20 nm at the edge and ~80 nm above the edge.[73] This means that the x-ray sampling depth changes as a function of energy, and while most of the electron signal originates from λ_e, some corrections for contributions of greater depths could be necessary for quantitative analysis. The reader is directed to reference 74 for a more quantitative description of electron yield measurements.

XAS spectra can also be measured in fluorescence yield mode. This method is similar to that of electron yield in that it measures the fluorescent signal produced when a valence electron fills the core-hole created by the incoming beam. However, because the produced photons are able to travel further in matter this technique can probe greater depths than electron yield mode. Since fluorescence yield measurements are susceptible to self-absorption effects this technique is less quantitative than either transmission or electron yield modes. Self-absorption is reduced for low concentrations of the target element, making fluorescent measurements well-suited for probing low doping levels. Fluorescent yield mode is also an excellent option for insulating samples where charging effects negative impact electron yield measurements.

In addition to the elemental coordination and valence information, x-ray absorption using polarized x-rays in an applied magnetic field probes elemental magnetism. These magnetic insights occur because the probability of exciting a core electron to a spin polarized valence state is different between left- and right-circularly polarized beams which have opposite angular momentum. The x-ray magnetic circular dichroism (XMCD) signal is the difference between the x-ray absorption spectra measured for the two polarizations and is proportional to the difference in the density of 'spin-

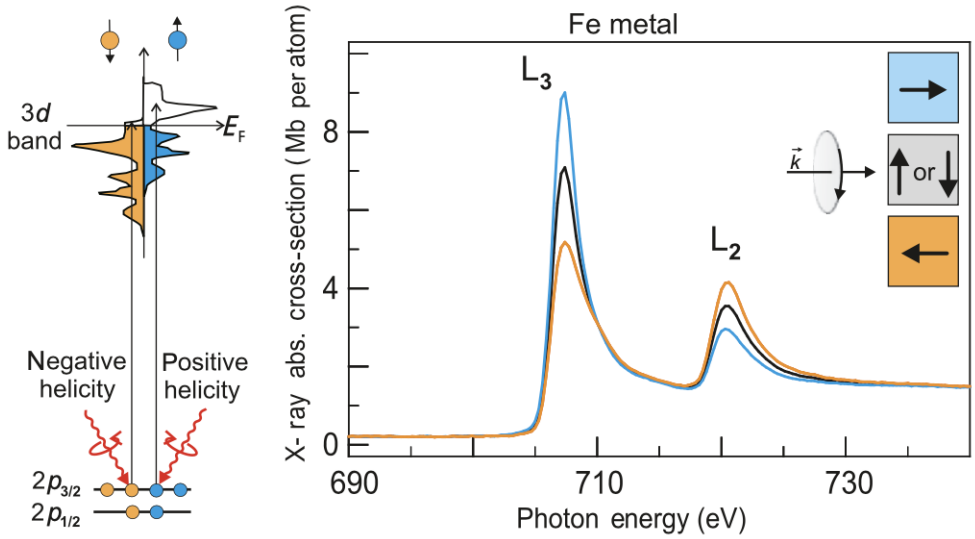

Figure 2.9: (left) Schematic of the XMCD effect for $L_{3,2}$ absorption edge of Fe metal. (right) Experimental data acquired using RCP light with sample magnetization as shown in inset. The XMCD signal (not pictured) is the difference between yellow and blue lines. Reproduced with permission from J Stöhr and HC Siegmann, Magnetism. Solid-State Sciences. Springer, Berlin, Heidelberg, 5:236, 2006. Copyright Springer.

up' and 'spin-down' states that generate the magnetic moment as shown in figure 2.9. As a result, the XMCD signal is directly proportional to the atomic magnetic moment. Note that in this ideal model, a fixed beam helicity measured in a magnetic field with positive and negative polarity is completely equivalent (see figure 2.9).

XMCD of the $L_{3,2}$ edges begins with the excitation of the $2p_{3/2}$ (L_3) and $2p_{1/2}$ (L_2) electrons. Since these levels have opposite spin-orbit coupling ($l+s$ and $l-s$, respectively), the spin polarization will be opposite at the L_3 and L_2 edges. Additionally, because dipole selection rules do not allow for spin flips during excitation ($\Delta S = 0$), spin-up $2p$ electrons can only be excited into partially unfilled spin-up $3d$ holes. By examining the possible transitions for the L_3 edge, we find that x-rays with a positive

photon spin will excite 62.5% of the spin-up electrons while a negative photon spin will excite 37.5% of the spin-up electrons. At the L_2 edge, a positive spin excites 25% of the spin-up electrons and a negative spin excites 75%. To maximize the XMCD signal, the photon spin should be aligned parallel to the magnetization of the sample in a saturating magnetic field.

While selection rules do not allow for spin flips during excitation, an indirect interaction of the x-ray's angular momentum and the spin of the electron can occur via spin-orbit coupling which impacts the relative intensities of the L_3 and L_2 edges. Information about the spin moment (m_s) and orbital moment (m_l) can be obtained from sum rules analysis using the relationship

$$\frac{m_l}{m_s} = \frac{2q}{9p - 6q} \tag{2.12}$$

where p is the integrated area of XMCD spectrum over the L_3 edge and q is the integrated area of both $L_{3,2}$ edges.[75] To extract useful information, XMCD spectra should be free of non-magnetic artifacts before the integrated areas are calculated. Such artifact-free XMCD spectra can be obtained by averaging the XMCD signals from both magnetic field polarities.

XAS and XMCD spectra of the Fe_3O_4 nanorods were acquired at beamline 4-ID-C of the Advanced Photon Source (APS), while measurements of the ϵ-Fe_2O_3-based nanoparticles were acquired at beamline 4.0.2 of the Advanced Light Source (ALS). All measurements were done in a helium flow cryostat with powder samples mounted on carbon tape. ALS spectra were measured as flying scans. Spectra were collected in total electron yield mode, baseline corrected, and normalized to the maximum amplitude. XMCD spectra were XAS normalized. Where noted as artifact-free,

XMCD spectra were averaged over both beam helicities and field polarities. XAS simulations were performed using CTM4XAS and Crispy.[76,77]

2.6.2 X-ray absorption fine structure spectroscopy

X-ray absorption fine structure (XAFS) spectroscopy is a 'hard' x-ray technique, utilizing higher energies than those of XAS discussed previously. As with XAS, a monochromated beam of x-rays interacts with the sample. When the incoming photons have sufficient energy to overcome the binding energy, core electrons are excited and an absorption edge occurs. While transition metal XAS spectra consist $L_{3,2}$ edges from the excitation of $2p$ orbitals, XAFS spectra of transition metal ions typically probe the K edge where $1s$ core electrons are excited. The decay of the excited state then produces a cascade of emissions via photoelectrons, Auger electrons, and x-ray fluorescence. Like XAS, the XAFS spectrum can be measured in either transmission mode or fluorescence mode and is proportional to the x-ray absorption coefficient ($\mu(E)$).

The XAFS spectrum itself can be divided into two parts: the near edge spectra (XANES) composed of features that occur within ~30 eV of the edge jump and the extended fine structure (EXAFS) that contains oscillations which extend up to a few kV above the edge. This thesis will utilize only the EXAFS portion, and so that will be the focus for the remainder of this discussion.

Figure 2.10 shows how the EXAFS spectrum is produced.[78] In the pre-edge region where beam energy (E) is less than the binding energy of the $1s$ state (E_0), there is not enough energy to excite a transition and so $\mu(E)$ is low. At $E = E_0$ such transition

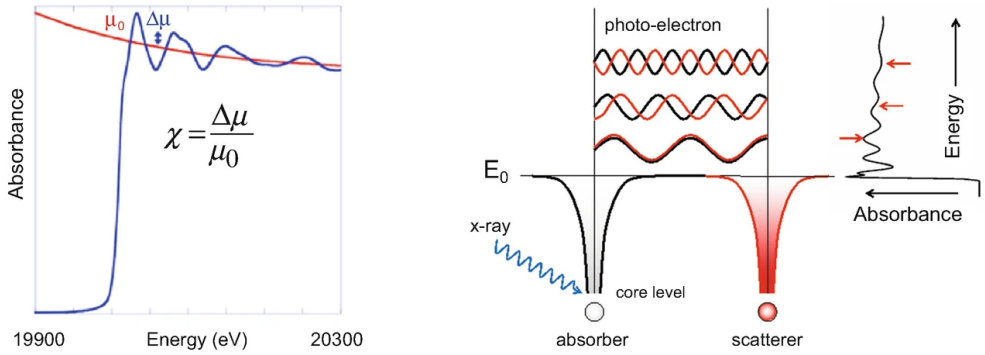

Figure 2.10: Schematic of how EXAFS spectrum is produced as described in the text. Reproduced with permission from SP Cramer, X-ray absorption and EXAFS, X-Ray Spectroscopy with Synchrotron Radiation: Fundamentals and Applications, 2020. Copyright Springer Nature.

becomes possible and there is a jump in absorption known as the edge jump. As the beam energy is increased further, excess energy can produce a photoelectron that propagates from the absorbing atom with wavelength $\lambda \sim 1/\sqrt{(E - E_0)}$. This photoelectron can scatter from a neighbouring atom causing interference with this initial wave. This interferance modulates $\mu(E)$ and results in the oscillatory behaviour of the EXAFS spectrum. The EXAFS region ($\chi(E)$) is isolated via

$$\chi(E) = \frac{\mu(E) - \mu_0(E)}{\Delta\mu} \tag{2.13}$$

where $\mu(E)$ is the measured absorption coefficient, $\mu_0(E)$ is a smooth background function representing the absorption of a single (isolated) atom, and $\Delta\mu$ is the measured jump in $\mu(E)$ at E_0.

Since the wave-like behaviour of the photoelectron underpins the physics of the EXAFS regions, the wavenumber (k) is usually used to describe the spectrum where

$$k = \sqrt{\frac{2m(E - E_0)}{\hbar^2}} \tag{2.14}$$

and m is the mass of an electron. $\chi(k)$ can then be weighted by different powers of k to enhance oscillations at higher energies. Because the frequencies of the oscillations is $\chi(k)$ originate from neighbouring atoms, a Fourier transform into real space reveals information about the scattering path distances to neighbouring atoms. Thus EXAFS speaks directly to the local structure around the scattering ion. The EXAFS equation provides a framework to model the contributions from different neighbouring ions via

$$\chi(k) = \sum_j \frac{N_j f_j(K) e^{-2k^2\sigma_j^2}}{kR_j^2} \sin[2kR_j + \delta_j(k)] \tag{2.15}$$

where j is the shell of N identical atoms located distance R from the excited atom, $f(k)$ and $\delta(k)$ are scattering properties of the photoelectron emitted by the neighbouring atoms, and σ^2 is the disorder in the distance.[79]

Extended x-ray absorption fine structure (EXAFS) spectra of the Fe K-edge were collected at beamline 20-BM-B of the Advanced Photon Source at Argonne National Laboratory. The x-ray beam was monochromated by a Si(111) double crystal monochromator. A harmonic rejection mirror was used and the beam intensity was detuned by 15% to eliminate the higher-order harmonics. Samples were a thin layer of powder enclosed in Kapton tape inside a displex low temperature stage, and spectra were collected in transmission mode using an ionization chamber-based detector. Data processing and fitting were performed using the ATHENA and ARTEMIS software packages.[80]

Chapter 3

Trimerons and the Verwey transition in Fe_3O_4 nanorods

Magnetite (Fe_3O_4) is one of the oldest known magnetic materials, and has been the focus of many studies in large part because of its metal-insulator transition. Known as the Verwey transition, it was identified as a change in structure accompanied by a sudden decrease in electrical conductivity.[3,81] At room temperature, Fe_3O_4 is an inverse spinel with charge distribution $Fe^{3+}(Fe^{2.5+})_2O_4$. Below the Verwey temperature (T_V =$\sim$125 K in the bulk), the cubic phase transforms to a monoclinic structure with β=0.23° along the (110) direction. Much work has been focused on characterizing the low temperature phase of Fe_3O_4 with regards to structure. While an approximation of the crystal structure was published in 1982 by Iizumi et al.,[28] only in 2011 was the full $C2/c$ space group resolved for bulk Fe_3O_4 below T_V.[29]

Similarly, understanding of the electronic charge ordering behaviour has evolved significantly in the last two decades. Verwey's original proposal of alternating Fe^{2+} and Fe^{3+} in the octahedral B sites[30] has been discarded as both experimental tech-

niques and theoretical modelling have improved.[4,5] Recently, Senn et al. used the predictions of electronic band structure calculations based on density functional theory (DFT) with the inclusion of Coulomb interactions (DFT+U scheme)[31] and observed shortening of B site Fe-Fe distances to introduce the concept of 'trimerons'.[6,32] Trimerons are quasiparticles formed by the delocalization of t_{2g} electrons from a central Fe^{2+} ion to two acceptor ions resulting in orbital order within the three Fe sites.

Due to the complexity of the Verwey transition in ideal bulk Fe_3O_4, the behaviour of nanoscale Fe_3O_4 (both thin films and nanoparticles) is not well understood. Such nanoscale Fe_3O_4 is distinguished from its bulk counterpart by strain,[82] which has previously been shown to impact the metal-insulator transition in VO_2 thin films.[83–85] Because trimerons are oriented in a three dimensional network, the orbital molecules are affected by strain along a variety of planes. Experimentally, well-controlled strain has been shown to modify T_V in both externally strained Fe_3O_4 single crystals,[86–89] and a series of progressively strained epitaxial thin films.[90] In a similar manner, experimental studies of nanocrystals have identified the suppression (T_V <120 K) or disappearance of T_V with decreasing size,[91,92] but the origins of this behaviour has remained an open question. To provide an answer to the receding T_V with decreasing size, nanorods of varying size (and strain) are studied.[93]

3.1 Structural and Electronic Characterization

TEM images of the three sizes of nanorods were acquired to characterize the morphology and obtain particle size distributions of both length and width. Representative images and their corresponding size distributions are shown in figure 3.1. The aver-

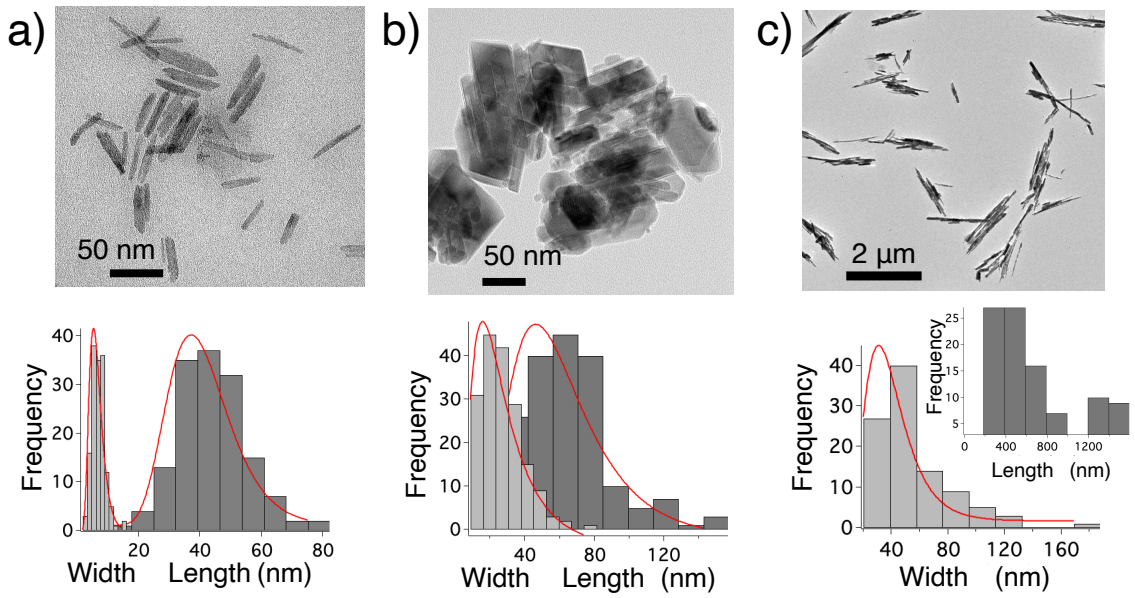

Figure 3.1: Representative TEM images of the a) small, b) medium and c) large nanorods and corresponding size distributions with lognormal fits of the length (dark grey) and width (light grey).

age size of the small nanorods is ∼6 nm by ∼40 nm, while the medium nanorods are ∼20 nm by ∼50 nm. The width of the large sample is ∼40 nm. Because the large nanorods were susceptible to breakage the length has an irregular size distribution unsuitable for fitting; however, the mean length is ∼700 nm. This breakage is a consequence of the two-step synthesis procedure, as any Cl impurities in the β-FeOOH precursor will form HCl during the reduction procedure, leading to pitting and cleavage of the Fe_3O_4 rods. Variations in contrast along the nanorods indicate that these samples are polycrystalline. For ease of discussion, the samples will be referred to from here by their average length (40 nm, 50 nm, and 700 nm).

Room temperature XRD patterns of the three samples are shown in figure 3.2. Reitveld refinement confirms that all crystallites have a spinel structure with space group $Fd\bar{3}m$. The lattice constants of 8.382(1) Å, 8.377(1) Å, and 8.3828(6) Å for the

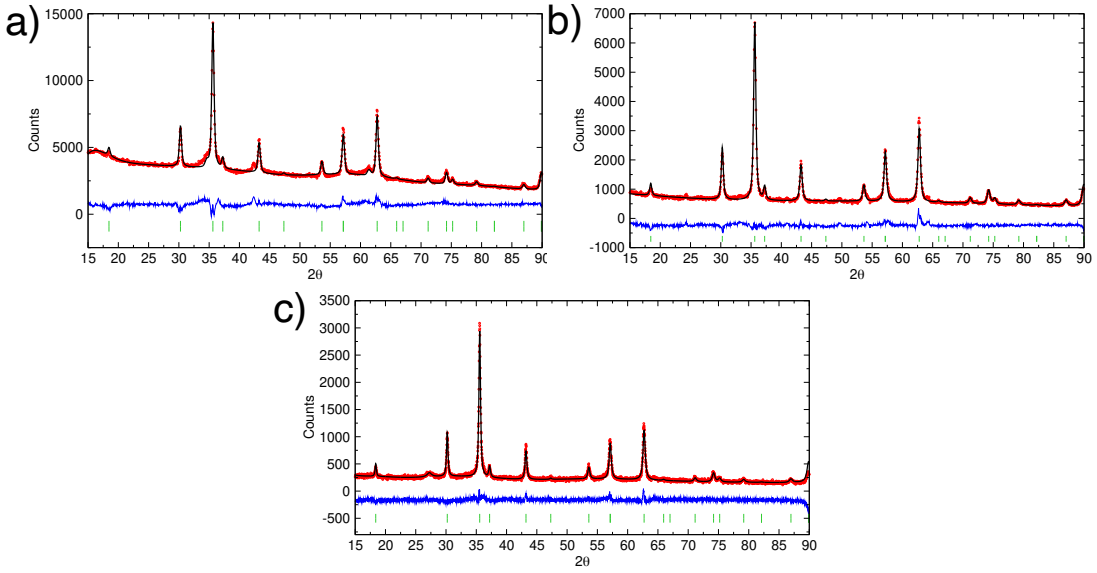

Figure 3.2: Room temperature XRD patterns of the a) small, b) medium and c) large nanorods. Red dots are data and black line indicates fit. The green Bragg markers index the $Fd\bar{3}m$ structure while the blue is the residuals of the refinement.

40 nm, 50 nm, and 700 nm nanorods, respectively, are consistent with Fe_3O_4 (8.39 Å in bulk) and not γ-Fe_2O_3 (8.34 Å in bulk).[12] The best fit to the data was achieved using a uniaxial crystallite size model where the unique axis for uniaxial refinement was determined to be along the (110) plane, and crystal strain was included. Both the 40 nm and 50 nm nanorods were fit using an isotropic strain model. The 40 nm nanorods had an average crystallite size of 14.2±0.6 nm by 16.3±0.6 nm, while the 50 nm nanorods had an average crystallite size of 14.9±0.7 nm by 17.2±0.7 nm. The isotropic strain for the the 40 nm and 50 nm nanorods are -0.53±0.03% and -0.21±0.05%, respectively, where the negative sign indicates compressive strain. The 700 nm nanorods had an average crystallite size of 34±4 nm by 53±4 nm, and were best fit with a uniaxial strain model. Strain was 0.42±0.05% along (110) and 0.25±0.07% perpendicular.

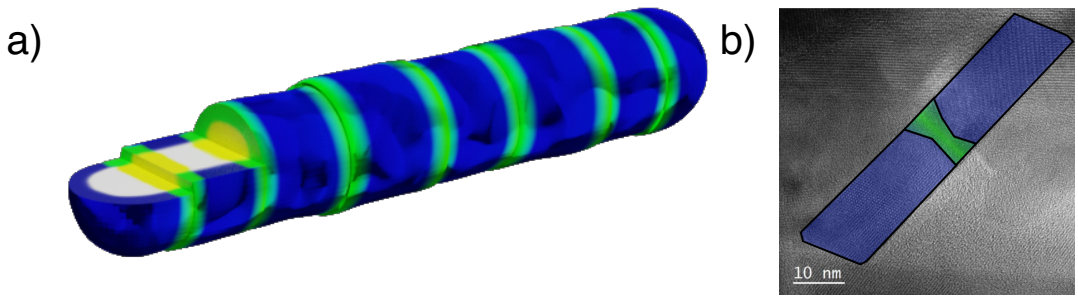

Figure 3.3: a) Schematic of strain present in a polycrystalline nanorod. Surface strain is blue, intercrystalline strain is yellow, region with both surface and intercrystalline strain is green, and unstrained crystallite is white. b) TEM image of a 50 nm nanorods composed of two crystallites with strained intercrystalline region shaded in green. Reproduced with permission from R Nickel et al, Advanced Materials, 33(16):2007413, 2021. Copyright John Wiley & Sons.

The mismatch between the nanorod dimensions obtained from TEM images and the crystallite dimensions confirms that all three nanorods are polycrystalline. As such, the quantified strain can be attributed to a variety of sources. Figure 3.3a shows a schematic of surface and intercrystalline strain in a polycrystalline nanorod. The intercrystalline strain is experimentally observed via TEM (see figure 3.3b).

High resolution STEM images, and the corresponding experimental and simulated diffraction patterns[66] of the 40 nm and 700 nm nanorods provide complementary information about local crystal strain. Figure 3.4 shows the images and diffraction patterns used for strain analysis of the 700 nm nanorods. The 40 nm nanorods exhibit exhibit an average of -0.04±0.03% of isotropic strain in each of the measured planes ((110), (111), and (112)). In contrast, the 700 nm nanorods show significant uniaxial strain along the (110) plane (∼0.5%), while both (111) and (112) planes have 0.09±0.02% strain. Thus the electron diffraction results and simulations are consistent with the XRD refinements. The 40 nm nanorods exhibit small isotropic

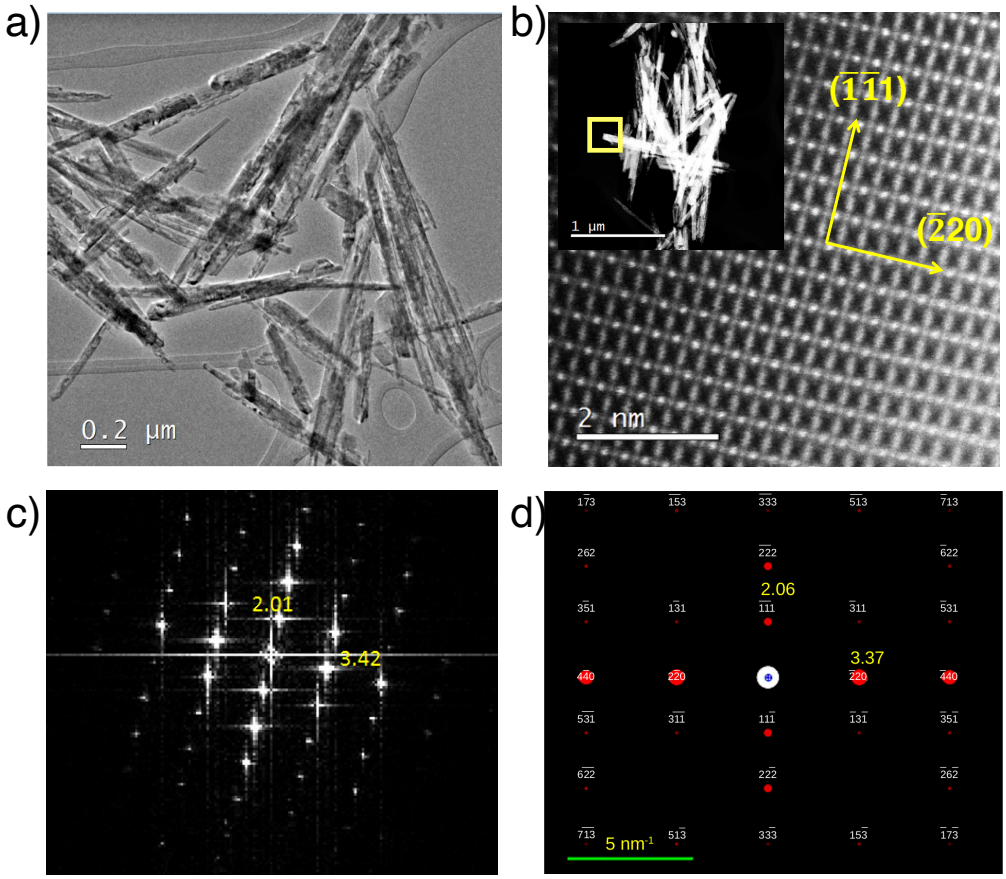

Figure 3.4: a) TEM image of 700 nm nanorods with contrast variation indicating pitting and polycrystallinity as discussed in the text. b) High magnification STEM image of 700 nm nanorods with orientation marked. (inset) Low magnification image of 700 nm nanorods. Box denotes acquisition region of c) diffraction pattern showing the Fe_3O_4 structure with zone axis [112]. d) Simulated diffraction pattern of Fe_3O_4 using Java Electron Microscope Simulation. Reproduced with permission from R Nickel et al, Advanced Materials, 33(16):2007413, 2021. Copyright John Wiley & Sons.

compressive strain and the 700 nm nanorods have large uniaxial tensile strain along the (110) plane. Strain in this direction is notable, because the two phonon modes whose freezing is associated with trimeron formation are cooperative along (110).[34] Differences between the electron diffraction and XRD results occur because electron

diffraction measurements characterize a highly localized region of the sample while XRD provides sample-averaged information.

While the structure of the different sizes of nanorods is more consistent with Fe_3O_4 than γ-Fe_2O_3, further evidence is necessary to confirm the phase. Low temperature Mössbauer spectroscopy is a more sensitive probe, because the two phases have very different hyperfine parameters (reflecting the different Fe coordination environments).[69] Figure 3.5 shows the Mössbauer spectra of the nanorods at 10 K. All spectra are well described by three sextets with equal relative absorption, corre-

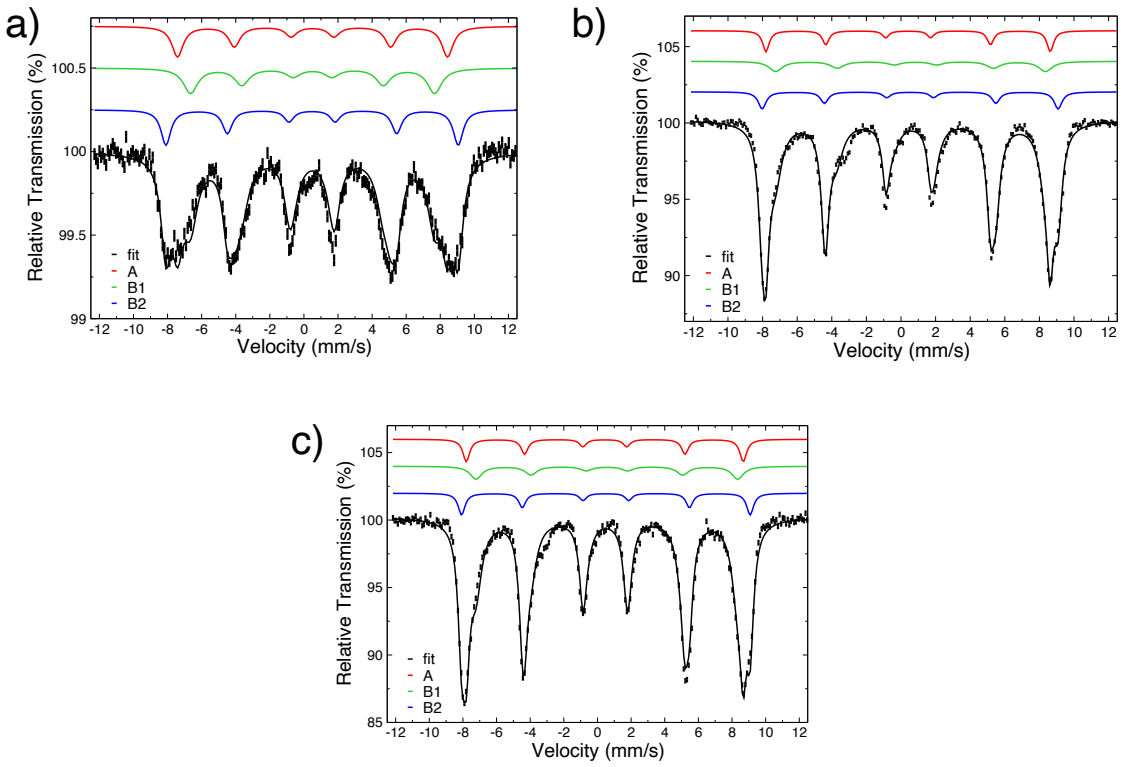

Figure 3.5: Mössbauer spectra at 10 K of a) 40 nm, b) 50 nm and c) 700 nm nanorods. Components A, B1 and B2 represent tetrahedral (T_d) Fe^{3+}, and octahedral (O_h) Fe^{2+} and Fe^{3+} respectively. Equal relative absorption between the three components is consistent with stoichiometric Fe_3O_4.

sponding to the Fe^{3+} T_d, Fe^{2+} O_h and Fe^{3+} O_h sites. The fitted hyperfine parameters are tabulated in table 3.1. The increased line width of the 40 nm nanorods reflects increased structural and chemical disorder due to finite size effects on the crystallites. Overall, the 10 K Mössbauer spectra clearly identify that all three sizes of nanorods are composed of Fe_3O_4.

Table 3.1: Hyperfine parameters of Fe_3O_4 nanorods at 10 K.

Size	Component	δ (mm/s)	B_{hf} (T)	Γ (mm/s)
40 nm	Fe^{3+} T_d	0.50 ± 0.02	49.2 ± 0.2	0.38 ± 0.08
	Fe^{2+} O_h	0.51 ± 0.02	44.4 ± 0.3	0.50 ± 0.06
	Fe^{3+} O_h	0.48 ± 0.01	53.3 ± 0.2	0.34 ± 0.03
50 nm	Fe^{3+} T_d	0.409 ± 0.007	51.09 ± 0.06	0.23 ± 0.03
	Fe^{2+} O_h	0.68 ± 0.02	48.6 ± 0.2	0.46 ± 0.04
	Fe^{3+} O_h	0.529 ± 0.009	53.15 ± 0.09	0.27 ± 0.02
700 nm	Fe^{3+} T_d	0.436 ± 0.007	51.16 ± 0.08	0.25 ± 0.03
	Fe^{2+} O_h	0.56 ± 0.02	48.3 ± 0.2	0.42 ± 0.03
	Fe^{3+} O_h	0.500 ± 0.007	53.31 ± 0.08	0.25 ± 0.02

3.2 Verwey Transition

Because all nanorod samples are confirmed as being Fe_3O_4, focus shifts to the observation of a Verwey transition in each sample. As the structural change from high temperature cubic to low temperature monoclinic is one of its defining features, XRD can identify the Verwey temperature (T_V) in bulk Fe_3O_4. The 20 K and 300 K patterns of the 700 nm nanorods are shown in figure 3.6. The refinement parameters of these patterns are in agreement within uncertainties, and thus the structural change observed in bulk Fe_3O_4 is not observed. Note that this is not unexpected, due to the finite size of the nanorod crystallites. The reported peak splitting in the cubic to monoclinic transition of bulk Fe_3O_4 has a peak-to-peak separation of 0.04°,[29] while the average FWHM of the 20 K pattern is 0.33° so any structural transition is obscured by the crystallite broadening. Differences in the residuals are attributed to background artifacts from the sample holder. Since XRD lacks the sensitivity to identify a Verwey transition in nanomaterials, other techniques are necessary.

The most commonly used identifier for nanoparticles is a change in the susceptibil-

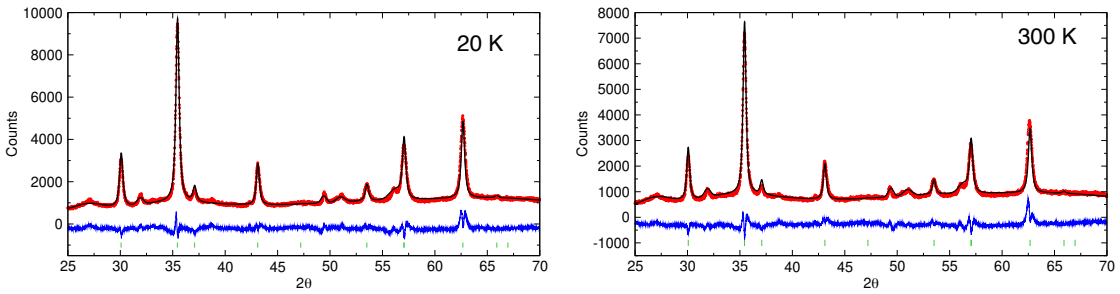

Figure 3.6: XRD patterns of 700 nm nanorods at 20 K (left) and 300 K (right). Red dots are data, black line are fit, green Bragg markers index the structure, and blue line is residuals.

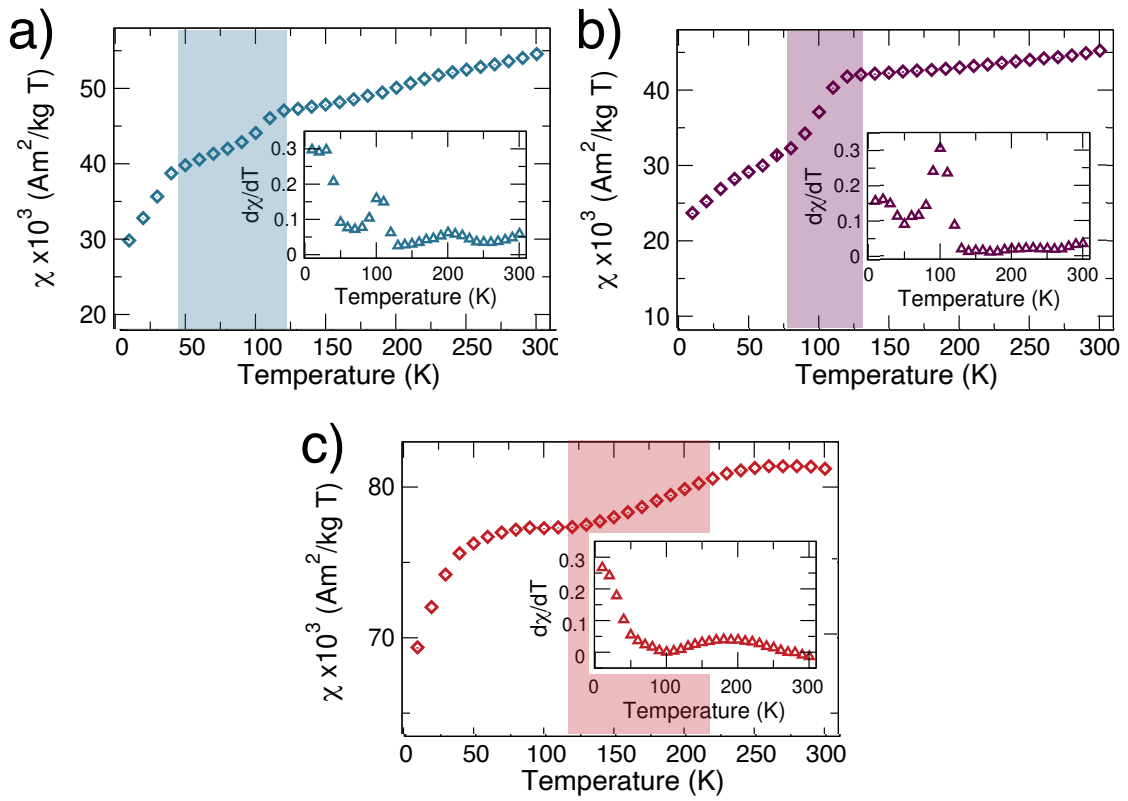

Figure 3.7: Zero-field cooled (ZFC) χ_{DC} of a) 40 nm, b) 50 nm and c) 700 nm nanorods measured in 50 mT. Inflection point corresponding to the change in magnetic susceptibility is indicated by shaded region, and derivatives are inset. Reproduced with permission from R Nickel et al, Advanced Materials, 33(16):2007413, 2021. Copyright John Wiley & Sons.

ity (χ_{DC}).[4] From figure 3.7, the ZFC χ_{DC} of both the 40 nm and 50 nm nanorods have an inflection point between 90-120 K and 80-120 K, respectively, while the 700 nm sample has a broad feature between 140 K and 220 K. The nature of these measurements are consistent with reported χ_{DC} of bulk Fe_3O_4, where the Verwey transition occurs at ∼125 K albeit over a much narrower temperature range.[4] Both the 40 nm and 50 nm nanorods, which have isotropic compressive strain, show the magnetic transition starting at a lower temperature than bulk Fe_3O_4, while the transition in

the uniaxially strained 700 nm nanorods begins at a higher temperature. While these results suggest a correlation between strain and the magnetic transition, the broadening of the observed magnetic transition from T_V within the nanorod samples prevents precise conclusions. Though the transition may occur over an increased temperature range due to structural inhomogeneities as evidenced by distributions of particle size, crystallite size and structural strain, the nature of the measurement is a contributing factor as magnetometry measurements of nanoparticles detect the collective response of a sample and are sensitive to effects such as dipole-dipole interparticle interactions.

Because the magnetometry measurement lacks sufficient clarity (particularly for the 700 nm nanorods), a complementary technique is necessary to uniquely identify the Verwey transition and corresponding T_V. Since the low temperature monoclinic phase is established by the freezing of phonon modes,[6,34] we can use the measured relative absorption (f-factor, or Debye-Waller factor) of Mössbauer spectra to detect the structural transition. The relative absorption of a Mössbauer spectrum depends on the oxidation and spin state of the ^{57}Fe atoms in the sample, as well as the elastic bond strength. As a result, the f-factor can be used to detect changes in valence, spin state or phase with temperature. For the Verwey transition, the structural transition from the high temperature cubic phase to the low temperature monoclinic phase would be expected to correspond with an increase in f-factor as the lattice stiffens and more phonon modes become frozen. Note that the f-factor is intrinsically temperature dependent. Based on the Debye model of phonon modes the temperature dependence is given by

$$f(T) = \exp\left[\frac{-3E_\gamma^2}{k_B\Theta_D Mc^2}\left\{\frac{1}{4} + \left(\frac{T}{\Theta_D}\right)^2 \int_0^{\Theta/T} \frac{x}{e^x - 1}\mathrm{d}x\right\}\right] \tag{3.1}$$

where $E_\gamma/2Mc^2$ is the free-atom recoil energy of 1.9563 meV for ^{57}Fe, k_B is the Boltzmann factor and Θ_D is the Debye temperature.

The temperature-dependent f-factor data is shown in figure 3.8 along with the theoretical curve for Θ_D=300 K – chosen because it described the high temperature behaviour of all three sizes of nanorods. The 40 nm and 50 nm nanorods have changes in f-factor from 15-25 K and 50-75 K, respectively, while the 700 nm sample shows an inflection point at 100 K and a jump between 140 K and 150 K. Note that the temperature range for the 40 nm nanorods was chosen to correspond to a ∼10%

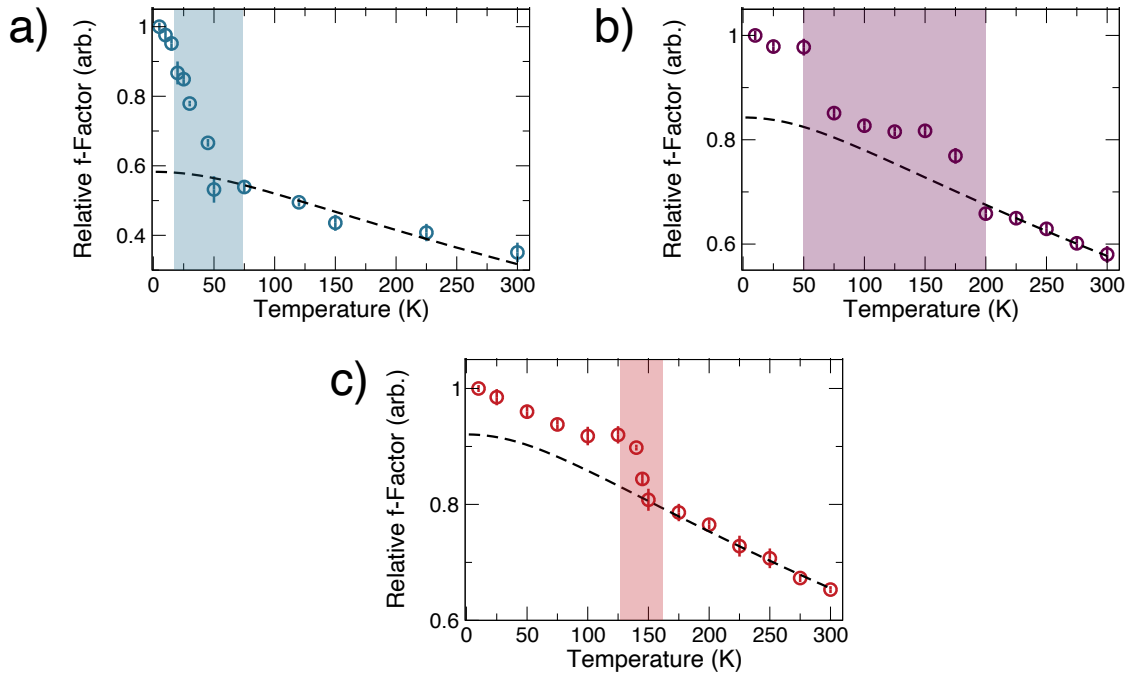

Figure 3.8: Temperature dependent f-factor of a) 40 nm, b) 50 nm and c) 700 nm nanorods. Temperature range where f-factor changes is indicated by shaded region. Dashed line is the analytical expression for the temperature dependent Debye-Waller factor where Θ_D=300 K. Reproduced with permission from R Nickel et al, Advanced Materials, 33(16):2007413, 2021. Copyright John Wiley & Sons.

jump in f-factor, consistent with that observed for the other two nanorod samples. The presence of both a structural and magnetic transition indicate that the nanorods all undergo a Verwey transition. The reduction in transition temperature from that observed in the magnetic susceptibility is because the f-factor is a very sensitive local probe. Overall, T_V is identified at 30 K, 60 K and 150 K for the 40 nm, 50 nm and 700 nm nanoparticles, respectively. The first jump at 60 K is identified as T_V for the 50 nm nanorods because it is sharper than the one at 170 K, which is likely caused by a differently strained population.

The decrease in T_V from that of bulk Fe_3O_4 ($\sim$125 K) to 20 K and 60 K for the 40 nm and 50 nm nanorods, respectively, is consistent with previous reports for nanoparticles where T_V decreases as particle size is reduced.[91,94–96] However, the average crystallite sizes of the 40 nm and 50 nm nanorods are comparable indicating that size is not the what affects the Verwey transition. Instead T_V is correlated with crystallite strain, with the transition temperature decreasing with increasing isotropic compressive strain since -0.53$\pm$0.03% strain was identified for the 40 nm nanorods compared to -0.21$\pm$0.05% for the 50 nm nanorods. This conclusion is consistent with the observed disappearance of the Verwey transition in very small ($<$ 6 nm) Fe_3O_4 nanoparticles[91] as surface lattice distortion causes increased isotropic strain.[97]

The 700 nm nanorods show the opposite behaviour, with a significantly increased T_V of $\sim$150 K. This increase is attributed the uniaxial tensile strain along the (110) plane (0.42$\pm$0.05%), similar to the T_V measured by Liu et al. on thin films strained along (001) with T_V = 136 K.[90] The 700 nm nanorods exhibit a higher T_V than these films because of the cooperative effect of phonon modes along (110), instead of the

competing effects along (001).[34] The strain along this plane generates minor shifts in the microstructure that increase the thermodynamic barrier to phonon unfreezing along multiple modes.

3.3 Trimerons in the 700 nm Nanorods

3.3.1 Evidence via XAS/XMCD

While trimerons have been accepted as the low temperature charge ordering mechanism behind the Verwey transition, experimental studies of the formation of these orbitally-ordered quasiparticles have been performed on ideal bulk Fe_3O_4 and the existence of trimerons in nanocrystallites have not been reported previously. The observed changes in T_V for all the nanorods speak to an altered energy landscape compared to bulk Fe_3O_4. With the largest shift in T_V, the 700 nm rods provide the clearest window into trimeron dynamics. Additionally, these nanorods present a unique opportunity to study the Verwey transition in a system under uniaxial tensile strain (a state unaccessible to bulk systems), and will be the focus for the remainder of this discussion.

To examine the elemental coordination and magnetism of Fe and O ions, and identify the formation of trimerons, x-ray absorption spectroscopy (XAS) and x-ray magnetic circular dichroism (XMCD) were performed over the Fe $L_{3,2}$ edge (700-740 eV). The Fe XAS spectrum located in figure 3.9 is consistent with an inverse spinel oxide.[98] From the 10 K simulation containing Fe^{3+} T_d, Fe^{2+} O_h, and Fe^{3+} O_h, the relative site areas of the Fe L_3 edge are 32%, 34% and 34%, respectively. This ratio matches well with that obtained from the 10 K Mössbauer spectrum, providing further

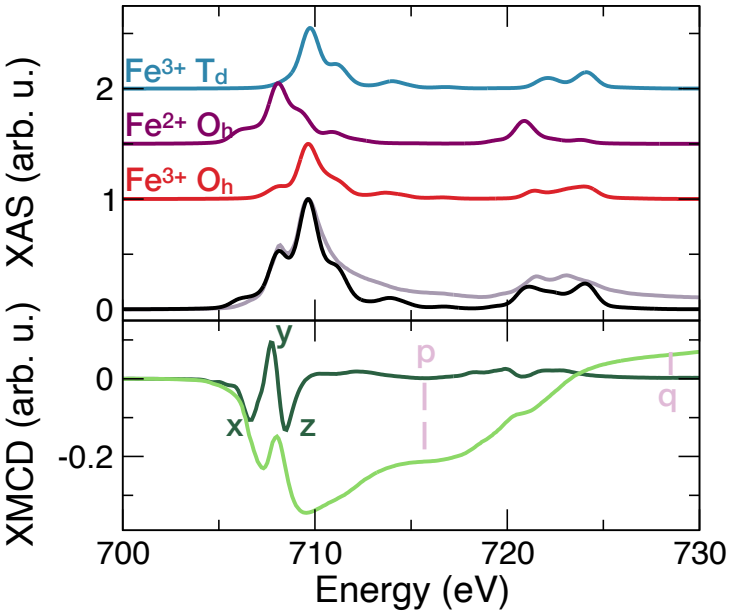

Figure 3.9: (top) 10 K Fe $L_{3,2}$ XAS spectrum of 700 nm nanorods. Experimental spectrum is grey and simulation is black. Simulated components of Fe^{3+} T_d (blue), Fe^{2+} O_h (purple), and Fe^{3+} O_h (red) shown above. (bottom) 10 K Fe $L_{3,2}$ XMCD spectrum and integrated area in dark green and light green, respectively. Features x, y, and z correspond to XMCD signal of Fe^{2+} O_h, Fe^{3+} T_d and Fe^{3+} O_h, respectively. Lines at 717 eV and 738 eV mark p and q used for sum rules analysis to calculate orbit-to-spin ratio. Reproduced with permission from R Nickel et al, Advanced Materials, 33(16):2007413, 2021. Copyright John Wiley & Sons.

confirmation of the phase. Minor differences between the experimental spectrum and the simulation could be the result of charge sharing between the Fe sites and orbital distortion caused by the formation of trimerons in the low temperature phase (below T_V).

Since Fe_3O_4 is a ferrimagnet, with antiferromagnetic coupling between T_d and O_h sites, the XMCD spectrum located in figure 3.9 is split. This effect is most clearly seen in the L_3 edge, with the contributions of the various sites marked. Because the orbital

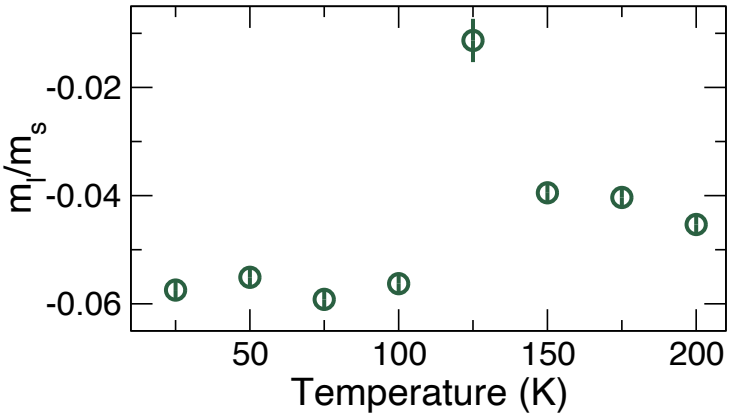

Figure 3.10: Temperature dependent orbit-to-spin ratio (m_l/m_s) of 700 nm Fe_3O_4 nanorods. Reproduced with permission from R Nickel et al, Advanced Materials, 33(16):2007413, 2021. Copyright John Wiley & Sons.

moment (m_l) and the spin moment (m_s) contribute differently to the L_3 and L_2 edges, sum rules analysis can be used to determine m_l/m_s as given in Equation 2.6.1. The parameters p and q used for this calculation are marked in figure 3.9 and quantify the integrated XMCD intensities over the L_3 and $L_3, 2$ edges, respectively. Note that there are practical limitations to determining m_l/m_s. $L_{3,2}$ edge mixing and $s-p$ hybridization (evidenced by the non-zero XMCD signal above the L_2 edge, and sensitivity to data all impact the accuracy of the m_l/m_s value, particularly for nanoscale systems.[99] However, the temperature dependence of m_l/m_s for a single sample can be used to track the evolution of the system. Figure 3.10 shows m_l/m_s as a function of temperature. The observed jump below 150 K indicates the formation of trimerons because the orbital order of the shared t_{2g} electrons will increase the orbital magnetic moment of O_h sites.[33]

XAS spectra were also collected over the O K edge (520-560 eV), where the pre-

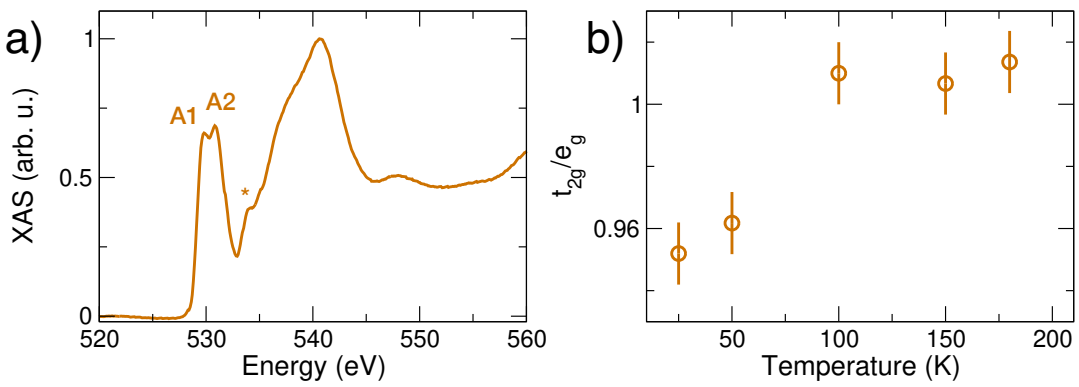

Figure 3.11: a) O K-edge XAS spectra at 50 K. A1 and A2 denote the pre-peak features. The characteristic feature of oxygen on the carbon tape is indicated by (*).[100] b) Temperature dependence of t_{2g} to e_g hole ratio determined from O K edge pre-peak amplitudes. Reproduced with permission from R Nickel et al, Advanced Materials, 33(16):2007413, 2021. Copyright John Wiley & Sons.

peak provides additional insights into the low temperature phase. This region of the spectrum relates to $2p-3d$-hybridization. Specifically, the splitting of the pre-peak speaks to the nature of the t_{2g} and e_g symmetry bands in d^5 ions, as the interactions of d^6 ions yield a broad (unsplit) peak.[101,102] Thus the relative intensity of the two features in the pre-peak (labelled A1 and A2 in figure 3.11a give insight into the t_{2g} to e_g hole ratio for the Fe^{3+} sites. Because the Fe^{3+} T_d atoms are not directly involved with the Verwey transition, variations with temperature are attributed to the Fe^{3+} O_h.

Figure 3.11b shows that below 100 K, the t_{2g} holes are the minority species, while the e_g holes are dominant above 100 K. Such a trend is consistent with the trimeron model where sharing of a central Fe^{2+}'s t_{2g} electron decreases the t_{2g} to e_g hole ratio in the low temperature phase. Interestingly, the observed jump in the electron ratio occurs at a lower temperature than the transitions observed in either the f-factor or

m_l/m_s. To better track how the environment around the Fe ions change through the Verwey transition, we use Mössbauer spectroscopy.

3.3.2 Evidence via Mössbauer Spectroscopy

Prior to the introduction of the trimeron picture, low temperature Mössbauer spectra have been primarily described by three components corresponding to Fe^{3+} T_d, Fe^{2+} O_h, and Fe^{3+} O_h.[27,103] This description was utilized in the initial phase identification of the nanorod samples. However, there have been reports since 1969 that suggest more Fe sites are present in low temperature Fe_3O_4.[104,105] Close examination of the 10 K spectrum fit with the conventional three component fit reveals missed absorption along the inner edge of line 2 (from the $m_{3/2} \rightarrow m_{1/2}$ transition). This absorption can be better fit using a four component fit where the additional sextet corresponds

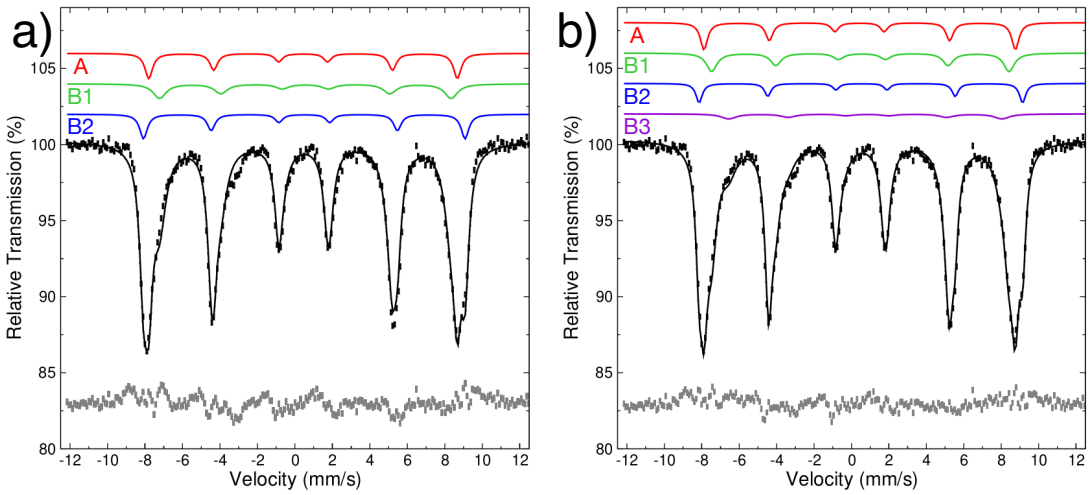

Figure 3.12: Mössbauer spectrum of 700 nm nanorods at 10K fit with either a) three sextets or b) four sextets corresponding to Fe^{3+} T_3 (A), Fe^{2+} O_h (B1), Fe^{3+} O_h (B2/B3). Fit is solid black line and residuals shown in grey. Reproduced with permission from R Nickel et al, Advanced Materials, 33(16):2007413, 2021. Copyright John Wiley & Sons.

to a second coordination of Fe^{3+} O_h, as evidenced by smoother residuals. Figure 3.12 shows the both the three and four component fits with residuals. The four component fit is quantitatively better, with χ^2_ν of 3.6 compared to 5.4 for the three component fit.

In this four component fit, the relative site areas of the sites Fe^{3+} T_d:Fe^{2+} O_h:Fe^{3+} O_{h1}:Fe^{3+} O_{h2} are 8:8:5:3, matching DFT simulation results of the trimeron model.[106] Compared to the three component fit, the incorporation of a third O_h site has minimal effect on the T_d site hyperfine parameters with δ=0.441±0.006 mm/s, Γ=0.25±0.02 mm/s and B_{hf}=51.34±0.07 T. Both O_h sites from the conventional fit are affected by the addition of the third O_h site (Fe^{3+} O_{h2}). A detailed examination of the hyperfine parameters provides insights into the local electronic structure of the Fe ions.

Based on the isomer shifts of 0.517±0.009 mm/s and 0.517±0.007 mm/s respectively, the Fe^{2+} O_h and Fe^{3+} O_{h1} sites are located in identical electronic environments – implying a strong interaction. The oxidation states are identified by their hyperfine fields of 49.39±0.07 T and 52.71±0.05 T since $B_{hf,2+} < B_{hf,3+}$.[69] Thus all of the Fe^{2+} O_h sites interact with the majority of the Fe^{3+} O_h. This interpretation is consistent with the trimeron picture where all of the Fe^{2+} share t_{2g} electrons with acceptor ions, and all but one acceptor is Fe^{3+}.[6] Since the Fe^{3+} O_{h2} site has very different isomer shift than the other O_h sites with δ=0.79±0.04 mm/s, these ions are in a different bonding environment and are not involved in trimeron formation. Notably, this component exhibits an increased line width (Γ=0.49±0.07 mm/s), reflecting significant local disorder. In the trimeron model for bulk Fe_3O_4, only two of the eight Fe^{3+} O_h ions are not involved in trimeron formation.[6] The Mössbauer spectrum indicates that

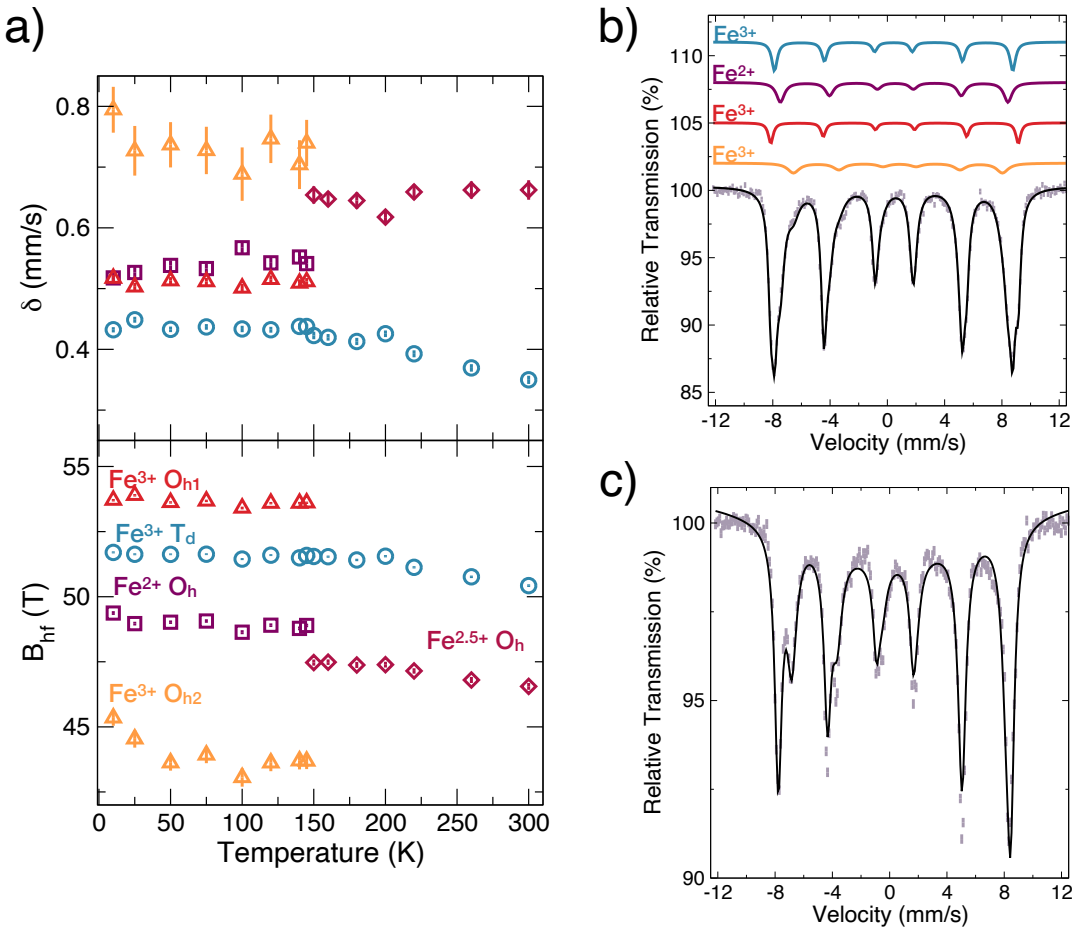

Figure 3.13: a) Temperature dependent isomer shifts (δ) and hyperfine fields (B_{hf}) of 700 nm nanorods. Hyperfine parameters of broad singlet component (T>150 K) not shown as both δ and B_{hf} are zero. Mössbauer spectra at b) 10 K and c) 300 K. Reproduced with permission from R Nickel et al, Advanced Materials, 33(16):2007413, 2021. Copyright John Wiley & Sons.

these nanorods have three non-participating Fe^{3+} ions per unit cell. Differences in microstructure due to strain are a possible origin of this difference.

Further insights are obtained by tracking the temperature evolution of the hyperfine parameters. As evident in figure 3.13a, the T_d site is relatively constant throughout the entire temperature range (from 10 to 300 K) indicating that these ions are not

affected by the Verwey transition and the formation/dissolution of trimerons. Note that the decrease in both δ and B_{hf} of the T_d site with increasing temperature can be attributed to a standard second order Doppler shift.[70] By comparison, the O_h sites show variations with temperature and provide insights into the electronic evolution of the Fe_3O_4 nanorods. Below 150 K, small variations in the hyperfine parameters of the O_h sites are visible. Most clearly, the variation of the isomers shifts of the interacting Fe^{2+} O_h and Fe^{3+} O_{h1} at 25 K and again at 100 K suggests changes to the trimerons. A simultaneous effect is evident in δ of the Fe^{3+} O_{h2} site as well, indicating that all O_h sites are affected by trimeron dynamics.

At 150 K the Mössbauer spectrum transforms as the three sextets that describe the O_h sites in the low temperature phase are replaced by a single sextet with mixed valence ($Fe^{2.5+}$) and a broad singlet. This sharp change in hyperfine parameters corresponds to the conclusion of the jump observed in the temperature dependent f-factor indicating that the change in phonon modes precedes that of the local environment around the Fe ions. The 10 K and 300 K spectra are shown in figure 3.13a-b. At 300 K the isomer shifts of the Fe^{3+} T_d and $Fe^{2.5+}$ O_h sextets are 0.350±0.007 and 0.66±0.02 mm/s, respectively. These values match well with the 0.32 mm/s and 0.66 mm/s reported for similarly sized spherical Fe_3O_4 nanoparticles. Similarly, the hyperfine fields of 50.42±0.05 and 46.6±0.1 are consistent with the reported values of 49.1 and 45.7 T.[95] Thus above 150 K the signatures of trimeron formation vanish and the mixed valence $Fe^{2.5+}$ O_h sites are recovered.

Reports of 300 K Mössbauer of Fe_3O_4 do not account for the broad singlet; however, by comparing the experimental 300 K spectrum (shown in figure 3.13c) to that

of bulk Fe_3O_4 there are clear discrepancies.[27] Most notably the spectra appears to be a spinel rather than an inverse spinel since the outer sextet corresponding to the T_d site is more heavily weighted than the inner sextet from O_h sites. This suggests a deficiency of O_h site Fe ions characteristic of γ-Fe_2O_3; however, at 10 K, the Mössbauer fit was consistent with stoichiometric Fe_3O_4. Thus the O_h site absorption missing from the sextet must be the source of the broad singlet, where the large line width reflects a high degree of disorder. Based on the evidence of trimeron formation at low temperatures, we attribute this to the persistence of some trimerons above 150 K – possibly due to the intrinsic strain preventing full quasiparticle dissolution.

3.3.3 Impact on Magnetism

Overall, the temperature dependent Mössbauer spectra confirm the formation of trimerons in the low temperature phase, as well as their breakdown at 150 K. Interestingly, instabilities within the trimeron state are observed. The separation of the Fe^{2+} O_h and Fe^{3+} O_{h1} isomer shifts at 100 K reveal that the trimeron-bonded sites shift to slightly different bonding environments. Such behaviour is consistent with the reduction in the t_{2g} electron sharing observed from the O K-edge data and the inflection point in the temperature dependent f-factor at 100 K. The impact of these fluctuations is also evident in the overall magnetism, with the coercivity ($\mu_0 H_C$) decreasing at 100 K (see figure 3.14a). This reduction in $\mu_0 H_C$ is consistent with the higher monoclinic anisotropy constants being exchanged for a much smaller cubic magnetocrystalline anisotropy constant.[107] Similarly, the squareness ratio (M_R/M_S, shown in figure 3.14b), shows an initial decrease at 100 K, indicating the a change in

domain wall motion has occurred, followed by a greater change at 150 K.

While both $\mu_0 H_C$ and M_R/M_S are affected by the trimeron fluctuations at 100 K, the magnetic saturation (M_S) is not. Instead, a change in behaviour is observed at ∼150 K. Because M_S reflects the magnon fluctuations in the system, it is expected to follow Bloch's $T^{3/2}$ Law ($M_S(T) = M_S(0)(1 - BT^{3/2})$) where the slope ($B$) of $M_S(T^{3/2})$ is proportional to the material's exchange interaction. As shown in figure 3.14c, $M_S(T) \propto T^{3/2}$ is observed, with two distinct regimes relating to two different Bloch constants. This behaviour means that the exchange interaction strengths are

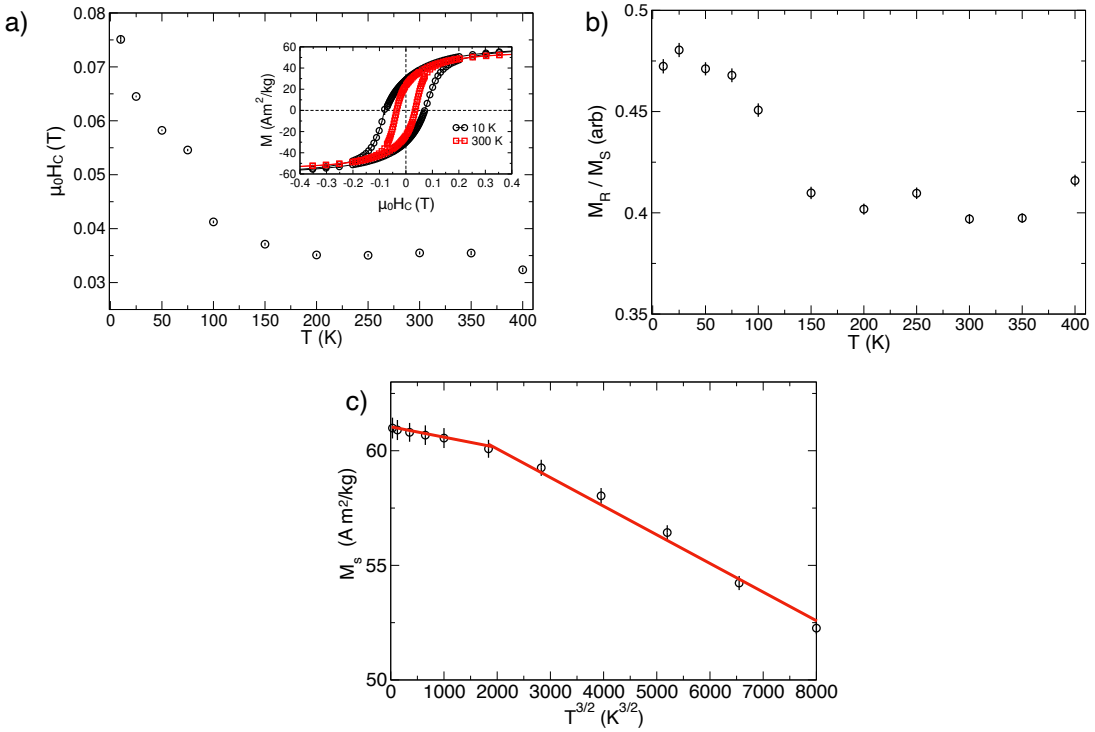

Figure 3.14: a) Coercive field ($\mu_0 H_C$) of the 700 nm Fe_3O_4 nanorods as a function of temperature. Inset contains hysteresis loops at 10 K (black triangles) and 300 K (red squares). b) Squareness ratio (M_R/M_S) as a function of temperature. c) Magnetic saturation (M_S) of large nanorods as a function of $T^{3/2}$. Linear regimes are marked in red to guide the eye.

weakened when the trimerons dissolve at 150 K, consistent with the jump in $m_l : m_s$ and drastic change of hyperfine parameters.

3.4 Summary

Three different sizes of Fe_3O_4 nanorods were characterized and their Verwey transitions identified.The 40 nm and 50 nm nanorods exhibited T_V at 40 K and 80 K, respectively – substantially lower than the ∼125 K observed in bulk crystals. In contrast, the 700 nm nanorods with tensile strain along (110) undergo a Verwey transition at 150 K. Overall, the shifts in T_V with nanorod size reveal a clear relationship between the temperature of this metal-insulator transition and strain. Detailed study of the 700 nm nanorods confirms the trimeron model of the low temperature insulating state and reveals a deviated microstructure with three non-participating Fe^{3+} O_h instead of two. Such a state arises because the uniaxial strain changes the energy landscape and strengthens the hybridization that generates the orbital molecules. These results provide an explanation for why signature transitions such as the Verwey transition in Fe_3O_4 or Morin transition in α-Fe_2O_3 tend to vanish in the nanoscale, and a clear handle by which to tune the metal-insulator transition.

Chapter 4

Size Dependent Behaviour and Magnetic Transition of ϵ-Fe_2O_3

In chapter 3 one of the world's oldest known magnetic materials, Fe_3O_4, was examined to gain insights into how its characteristic Verwey transition is altered in the nanoscale. These results reveal that the hybridization which underpins Fe_3O_4's unique properties can be altered via crystal strain. In this chapter, the role of hybridization will be examined for a far more novel material.

ϵ-Fe_2O_3 is an iron oxide polymorph that has attracted interest for its enormous coercive field ($\mu_0 H_C$) of $\sim$2 T at room temperature, millimeter-wave ferromagnetic resonance, and magnetoelectric coupling.[10,42,43] Combined, these properties make ϵ-Fe_2O_3 appealing for a range of applications; however, exploiting this material demands a deeper understanding of its underlying physics than is presently available. There are two factors that add significant complexity to studying ϵ-Fe_2O_3. Firstly, ϵ-Fe_2O_3 is only stable in the nanoscale and so its overall properties are convolved with size effects. Secondly, the metastable nature of the perovskite ϵ-Fe_2O_3 tends to yield

samples that are not single-phase. Because this secondary phase (often α-Fe_2O_3) is also of the nanoscale, its properties are less well-defined than a bulk analogue and thus decoupling the two phases becomes impossible. To decouple size effects and obtain insights into the physics that underpins the properties of ϵ-Fe_2O_3, three sizes of phase-pure ϵ-Fe_2O_3 nanoparticles are studied.[108]

4.1 Physical Characterization

TEM images were acquired of the three ϵ-Fe_2O_3 samples to identify how annealing temperature affects nanoparticle morphology. Representative images are shown in

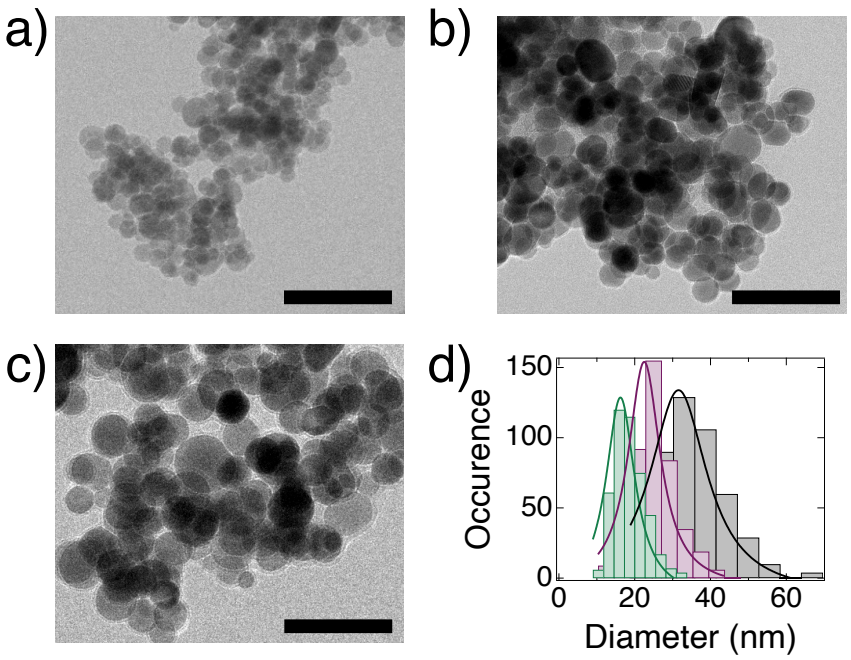

Figure 4.1: Representative TEM images of ϵ-Fe_2O_3 nanoparticles annealed at a) 1100°C, b) 1150°C and c) 1200°C. Size bars are 100 nm. d) Size distributions of 1100°C, 1150°C and 1200°C shown in green, purple and black, respectively, with the lines to guide the eye. Reprinted with permission from R Nickel, *et al.* Nano Letters, 2023. Copyright 2023 American Chemical Society.

figure 4.1a-c. Overall, all samples are composed primarily of spherical particles, as is expected for this type of synthesis, which lends itself to isotropic growth. ImageJ was used to quantify the size of ∼450 particles per sample, and the resulting size distributions are shown in figure 4.1d). From a Gaussian fit, the average diameter of the sample annealed at 1100°C is 16 ± 5 nm, while the 1150°C and 1200°C yielded 22 ± 5 nm and 32 ± 9 nm, respectively. For ease of reference, the three samples will be denoted 15 nm, 20 nm and 30 nm.

Room temperature XRD patterns are shown in figure 4.2a. Full pattern Reitveld refinements were done using the structure described by Gich et al. in reference 41,

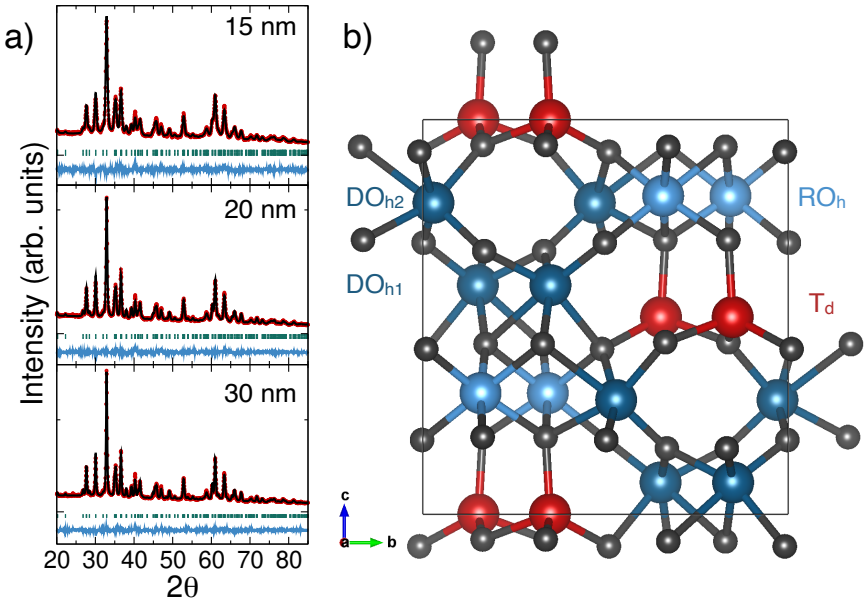

Figure 4.2: a) Room temperature XRD of 15 nm, 20 nm and 30 nm ϵ-Fe_2O_3 nanoparticles. Red markers are data and black line indicates fit. The green Bragg markers index the $Pna2_1$ structure while the blue is the residuals of the refinement. b) Crystal structure of ϵ-Fe_2O_3 where T_d is red, DO_{h1} and DO_{h2} dark blue, and RO_h light blue. Reprinted with permission from R Nickel, *et al.* Nano Letters, 2023. Copyright 2023 American Chemical Society.

Table 4.1: Lattice parameters, unit cell volume and average crystallite size (<d>) of ϵ-Fe_2O_3 nanoparticles at room temperature.

Sample	a (Å)	b (Å)	c (Å)	Volume (Å^3)	<d> (nm)
15 nm	5.0901 ± 0.0003	8.7898 ± 0.0006	9.4721 ± 0.0005	423.8 ± 0.3	16.9 ± 0.1
20 nm	5.0907 ± 0.0002	8.7850 ± 0.0004	9.4704 ± 0.0004	423.5 ± 0.2	23.4 ± 0.1
30 nm	5.0920 ± 0.0002	8.7870 ± 0.0004	9.4721 ± 0.0004	423.8 ± 0.2	29.8 ± 0.1

and illustrated in figure 4.2b. Atomic positions for all ten sites were fixed (tabulated in table 1.1) and full occupancy was assumed, while reflection broadening, lattice parameters and a twelve coefficient Chebychev background were fit for each pattern. All three patterns were well-described by the ϵ-Fe_2O_3 structure, and no additional reflections from secondary phases are evident. Lattice parameters do not show significant variations, while differences in the broadening of reflections indicate that the crystallite sizes increase with nanoparticle size. These results are summarized in table 4.1. Overall, the volume-normalized crystallite sizes obtained from the XRD refinement agree well with the plane-view averaged nanoparticle sizes determined from TEM image analysis, and the underlying crystal structure is very similar.

While XRD shows no significant differences in the crystal structure with nanoparticle size, EXAFS spectra were measured over the Fe K edge to provide more sensitive, local information about the structure. Spectra acquired at 50 K along with the extracted k^2-weighted $\chi(k)$ are shown in figure 4.3a-b. While oscillations extend to higher wavenumbers, the fitting range was constrained from 3 to 9.5 Å^{-1}. The Fourier transform of this range and corresponding fit is shown in figure 4.3c. The data was fit in real space from 1 to 3.5 Å using k weights of 1, 2 and 3. Because the

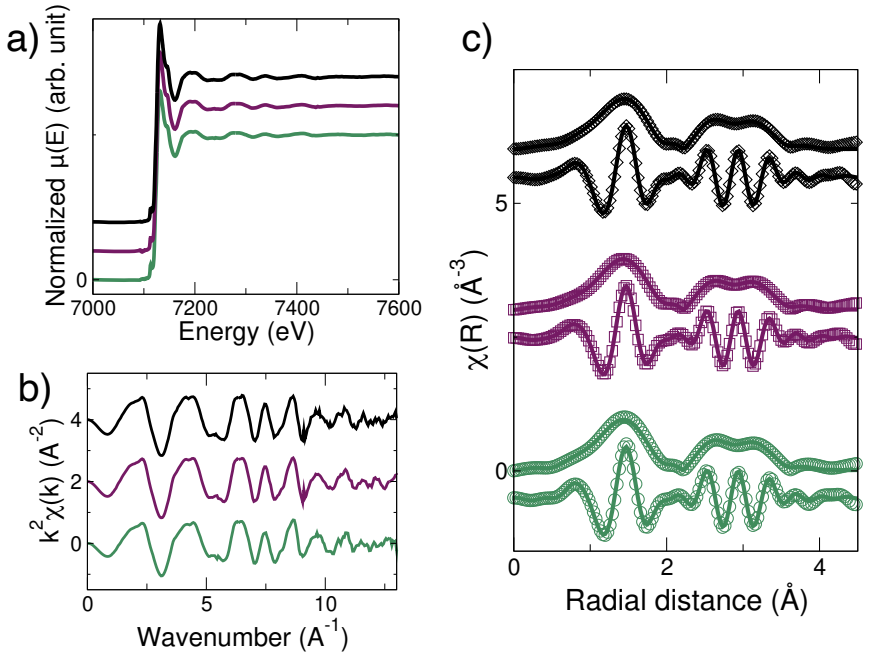

Figure 4.3: a) EXAFS spectra and k^2-weighted $\mu(k)$ of 30 nm (black), 20 nm (purple) and 15 nm (green) ϵ-Fe_2O_3 nanoparticles at 50 K. c) Corresponding Fourier transformed EXAFS spectra in real space of 30 nm (black), 20 nm (purple) and 15 nm (green) ϵ-Fe_2O_3 nanoparticles with fits (solid lines). Reprinted with permission from R Nickel, *et al.* Nano Letters, 2023. Copyright 2023 American Chemical Society.

distorted perovskite structure exhibits a low degree of local symmetry, a simplified model is necessary to fit the data otherwise the number of scattering paths becomes enormous. For example, the four Fe and six O sites combine to yield 18 distinct nearest neighbour Fe-O paths. This complexity increases exponentially as next nearest neighbours and multiple scattering paths are considered. Instead, the model used consists of only four paths: one nearest neighbour (NN) Fe-O, two NN Fe-Fe and one next-nearest neighbour Fe-O. Initial fitting was done to determine appropriate Debye-Waller parameters (σ^2) and corrections to the effective path lengths. These parameters were then fixed to minimize the number of free parameters in the final fit

Table 4.2: Path multiplicities from EXAFS fit.

Sample	Fe-O (1.957 Å/ 3.665 Å)	Fe-Fe_1 (3.029 Å)	Fe-Fe_2 (3.414 Å)
15 nm	4.5 ± 0.2	1.5 ± 0.2	2.9 ± 0.2
20 nm	4.4 ± 0.2	1.5 ± 0.2	2.9 ± 0.2
30 nm	4.4 ± 0.2	1.6 ± 0.2	2.9 ± 0.3

so that variations in the path multiplicities would be more evident. Both Fe-O paths had σ_O^2 of 0.0110, while σ_{Fe-Fe1} and σ_{Fe-Fe2} were 0.0067 and 0.0052, respectively. The final fit yielded an energy shift of -1.3 ± 0.4 eV for all spectra. Path multiplicities are summarized in table 4.2. All fit parameters agree within uncertainties indicating that the local structures of the three sizes of ϵ-Fe_2O_3 nanoparticles are practically identical.

4.2 Electronic Characterization

Mössbauer spectroscopy was used to characterize the local electronic environment around the Fe ions. While the structural techniques discussed thus far indicate that the samples are ϵ-Fe_2O_3, Mössbauer spectroscopy is a more sensitive probe because the other iron oxide polymorphs have significantly different hyperfine parameters and so the detection limit is much lower. The 10 K spectra of the three sizes of ϵ-Fe_2O_3 nanoparticles are shown in figure 4.4a. Each spectrum is composed of three components corresponding to the distorted octahedral (DO_h), regular octahedral (RO_h) and tetrahedral (T_d) sites. The relative areas of the three components are consistent with the expected 2:1:1 ratio of ϵ-Fe_2O_3.[41] The various hyperfine parameters are consis-

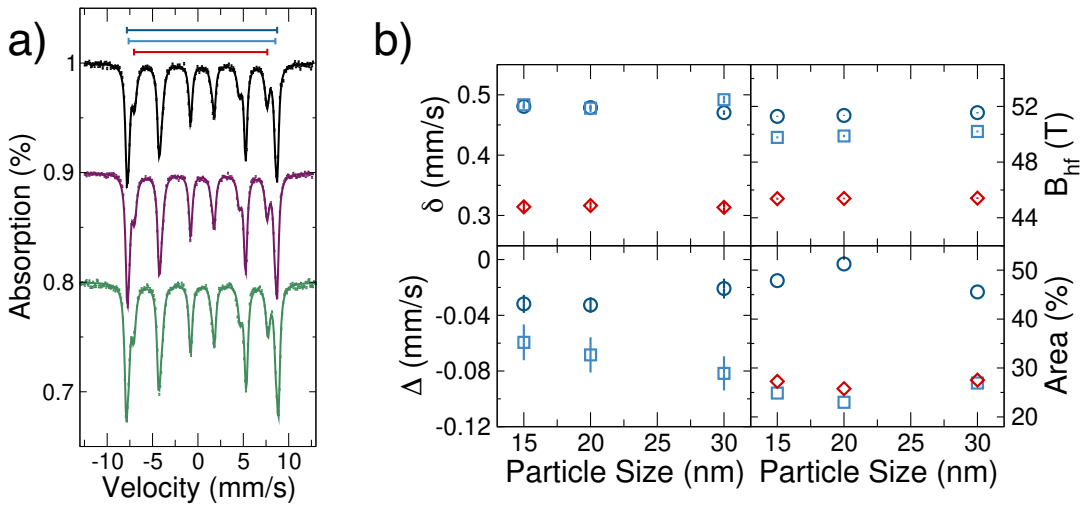

Figure 4.4: Transmission Mössbauer spectra at 10 K of 30 nm (black), 20 nm (purple) and 15 nm (green) ϵ-Fe_2O_3 nanoparticles with fits (solid lines). Hyperfine field of DO_h (dark blue), RO_h (light blue) and T_d (red) components indicated by lines above spectra. b) Isomer shift (δ, top left), quadrupole splitting (Δ, bottom left), hyperfine field (B_{hf}, top right) and relative area (bottom right) of ϵ-Fe_2O_3 nanoparticles as a function of size at 10 K. DO_h, RO_h and T_d sites shown as dark blue circles, light blue squares and red diamonds, respectively. Reprinted with permission from R Nickel, *et al.* Nano Letters, 2023. Copyright 2023 American Chemical Society.

tent with previous reports of ϵ-Fe_2O_3,[41,49] and notably there is no evidence of other iron oxides, particularly α-Fe_2O_3[48] which is the most typical additional phase present from the synthesis protocols. Table 4.3 contains a full tabulation of the hyperfine parameters.

Magnetic hyperfine fields (B_{hf}) of the 15 nm sample are 51.28 ± 0.04 T and 47.77 ± 0.08 T for the DO_h and RO_h sites, respectively, and 45.37 ± 0.07 T for the T_d site. All B_{hf} increase monotonically with size. For the 15 nm sample the isomer shifts (δ) of the DO_h and RO_h sites are 0.481 ± 0.003 mm/s and 0.483 ± 0.006 mm/s, respectively, while the T_d site is 0.314 ± 0.009 mm/s as expected for Fe^{3+}. Isomer

Table 4.3: 10 K Mössbauer hyperfine parameters of 15 nm, 20 nm, and 30 nm ϵ-Fe_2O_3.

Size	Γ (mm/s)		δ (mm/s)			Δ (mm/s)		B_{hf} (T)			Area (%)		
	RO_h/DO_h	T_d	RO_h	DO_h	T_d	RO_h	DO_h	RO_h	DO_h	T_d	RO_h	DO_h	T_d
15 nm	0.201(5)	0.30(2)	0.481(3)	0.483(6)	0.314(9)	-0.032(7)	-0.06(1)	51.28(4)	49.77(8)	45.37(7)	48	25	27
20 nm	0.211(4)	0.28(1)	0.479(3)	0.478(6)	0.316(7)	-0.033(6)	-0.07(1)	51.35(4)	49.88(8)	45.39(6)	51	23	26
30 nm	0.200(5)	0.28(2)	0.470(4)	0.492(6)	0.313(8)	-0.021(7)	-0.08(1)	51.56(5)	50.20(8)	45.41(6)	46	27	28

shifts for all sites of the 20 nm sample and the T_d site of the 30 nm sample are in agreement with these values. Unlike the smaller samples, the octahedral δ of the 30 nm sample are distinguishable, with δ_{DOh} of 0.470 ± 0.004 mm/s and δ_{ROh} of 0.491 ± 0.006. Such a splitting speaks to differences in the electronic charge density at these sites.

Such variations are also reflected in the quadrupole splitting (Δ), which describes the electric field gradient. For the 15 nm sample at 10 K Δ_{DOh} is -0.032 ± 0.007 mm/s and Δ_{ROh} is -0.05 ± 0.01 mm/s. Quadrupole splittings of the 20 nm nanoparticles are the same as those of the 15 nm nanoparticles, but the 30 nm particles are different, with Δ_{DOh} of -0.021 ± 0.007 mm/s and Δ_{ROh} of -0.08 ± 0.01 mm/s. Thus the electric field gradient of the DO_h component in the 30 nm sample is more symmetric than that of the smaller samples, while that of the RO_h component is more asymmetric. Overall, the altered hyperfine parameters for the 30 nm sample reflect electrons being pulled symmetrically away from the DO_h sites, and pushed asymmetrically towards the RO_h sites.

Because the structural characterization revealed no identifiable differences between the sizes of ϵ-Fe_2O_3 nanoparticles that can be correlated to the variations in the Mössbauer spectra, XAS spectra at 50 K were done to study the elemental coordination of both Fe and O. The Fe $L_{3,2}$ edge spectra shown in figure 4.5 are consistent with previous reports for ϵ-Fe_2O_3,[49,109] where feature at 707.8 eV is ~50% of the amplitude of the main L_3 peak and the dip between these peaks is ~40% of peak amplitude. No significant differences are evident between the $L_{3,2}$ edge spectra, indicating that Fe coordination and valence are indistinguishable with respect to

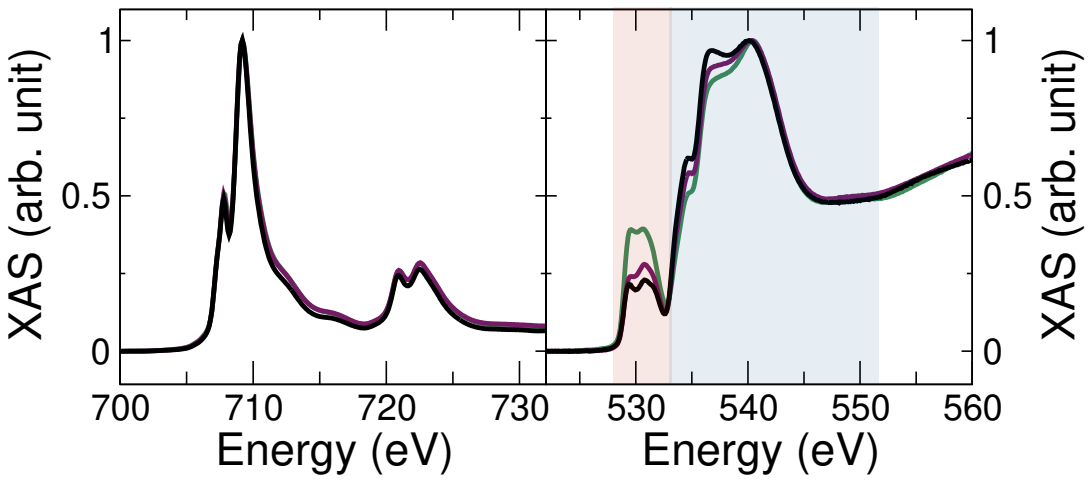

Figure 4.5: Fe $L_{3,2}$ edge (left) and O K edge (right) XAS spectra at 50 K of 30 nm (black), 20 nm (purple) and 15 nm (green) ϵ-Fe_2O_3 nanoparticles. Regions associated with $2p-3d$ and $2p-4sp$ hybridization of O K edge spectrum marked in red and blue, respectively. Reprinted with permission from R Nickel, *et al.* Nano Letters, 2023. Copyright 2023 American Chemical Society.

nanoparticle size for these samples.

In contrast, the O K edge is affected by nanoparticle size. As shown in figure 4.5, the spectrum is composed of two regions: the first from 528 to 532 eV which reflects $2p-3d$ hybridization and the second from 532 to 545 eV corresponding to $2p-4sp$ hybridization. Both of these regions show changes with nanoparticle size. The absorption in the $2p-3d$ region decreases as nanoparticle size increases, indicating decreased $2p-3d$ hybridization. The $2p-4sp$ region shows the opposite behaviour with increased absorption at both the 534.7 eV and 536.6 eV shoulders with increased particle size. Overall, the 50 K O K edge XAS spectra show that Fe-O hybridization is affected by nanoparticle size. The increase in $2p-4sp$ hybridization and reduction in $2p-3d$ hybridization is consistent with the 10 K Mössbauer hyperfine parameters which indicated subtle changes in the electronic configuration around the Fe sites.

These differences with nanoparticle size are most likely caused by the establishment of longer-range Fe-O ordering impacted by geometric restrictions.

4.3 Magnetic Characterization

Thus far, the structural and electronic characterization has been used to identify similarities and differences between samples at a single temperature. After establishing that all samples are single phase ϵ-Fe_2O_3 with near identical structures and only slight differences in electronic bonding, attention shifts to their magnetism – specifically, the magnetic phase transition between the low temperature incommensurate and the high temperature ferrimagnetic phases.[41]

Figure 4.6a shows the DC magnetic susceptibility measurements ($\chi_{DC}(T)$) for the three different sizes. In this measurement a virgin sample was first cooled to 10 K. The superconducting magnet is quenched prior to cooling to eliminate any remnant

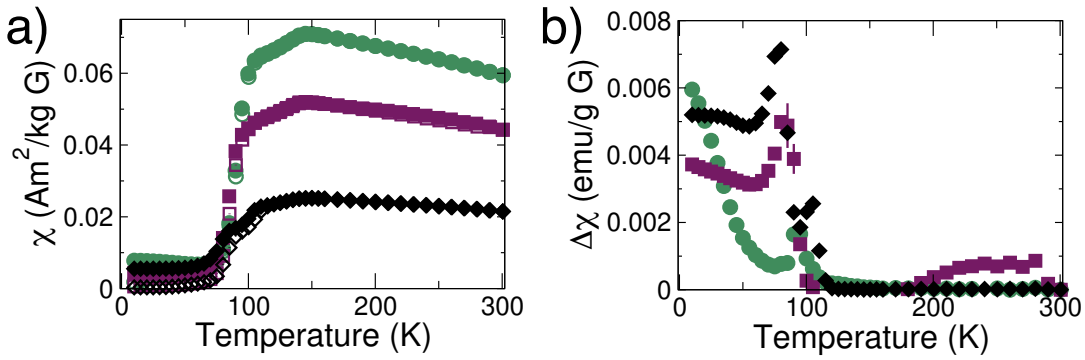

Figure 4.6: a) Zero field-cooled (open) and field-cooled (closed) $\chi_{DC}(T)$, and b) Difference between field-cooled and zero field-cooled $\chi_{DC}(T)$ of 15 nm (green circles), 20 nm (purple squares) and 30 nm (black diamonds) ϵ-Fe_2O_3 nanoparticles. Reprinted with permission from R Nickel, *et al.* Nano Letters, 2023. Copyright 2023 American Chemical Society.

field. A 5 mT magnetic field is applied and the magnetization is first measured upon warming to 300 K (zero-field cooled (ZFC)), then upon cooling (field-cooled (FC)) back to 10 K. All samples show the expected temperature dependence of ϵ-Fe_2O_3[110,111] with a weak magnetic response from 10 to 75 K followed by a sharp increase around 100 K, more gradual increase to a maximum at 150 K, and gradual decrease with further warming. Notably, the overall magnitude of $\chi_{DC}(T)$ decreases as nanoparticle size increases. This reduction in magnetic response is due to the decrease in the relative surface area-to-volume ratio. As ϵ-Fe_2O_3 is a ferrimagnet with a highly compensated spin structure, the broken coordination and reduced anisotropy of surface ions will increase the net magnetic response. A simple model can be used to illustrate the impact of surface effects. If the broken coordination is assumed to extend 2 nm (or roughly two unit cells) from the surface of the particle, then 57%, 44%, and 33% of the Fe ions will be located in this region for the 15 nm, 20 nm, and 30 nm particles respectively. The relative magnitude of $\chi_{DC}(T)$ in the ferrimagnetic phase (>150 K) scales with the reduced fraction of surface ions.

Differences between FC and ZFC $\chi_{DC}(T)$ ($\Delta\chi_{DC}(T)$) measurements are shown in figure 4.6b. In the ferrimagnetic phase, such differences are negligible, while below 100 K in the incommensurate phase where $\Delta\chi_{DC}(T)$ is non-zero and increases with increased nanoparticle size. Because this measurement quantifies the difference in magnetization between the field-cooled and that of the initial (random) configuration, this increase in $\Delta\chi_{DC}(T)$ is further evidence of the increased hybridization coupling and establishment of longer range ordering in the low temperature phase with nanoparticle size.

Hysteresis loops (shown in figure 4.7) quantify how the overall magnetism of the ϵ-Fe_2O_3 nanoparticles evolve with temperature. All three sizes show the expected collapse and expansion of the loop shape across the magnetic phase transition as the magnetic anisotropy is transformed. The temperature-dependent coercivity ($\mu_0 H_C$) and magnetic saturation (M_S) are shown in figure 4.8. Note that the magnetic saturation was calculated after the high field susceptibility was subtracted. This treatment is typical for nanoparticle samples, where this slope is attributed to a paramagnetic

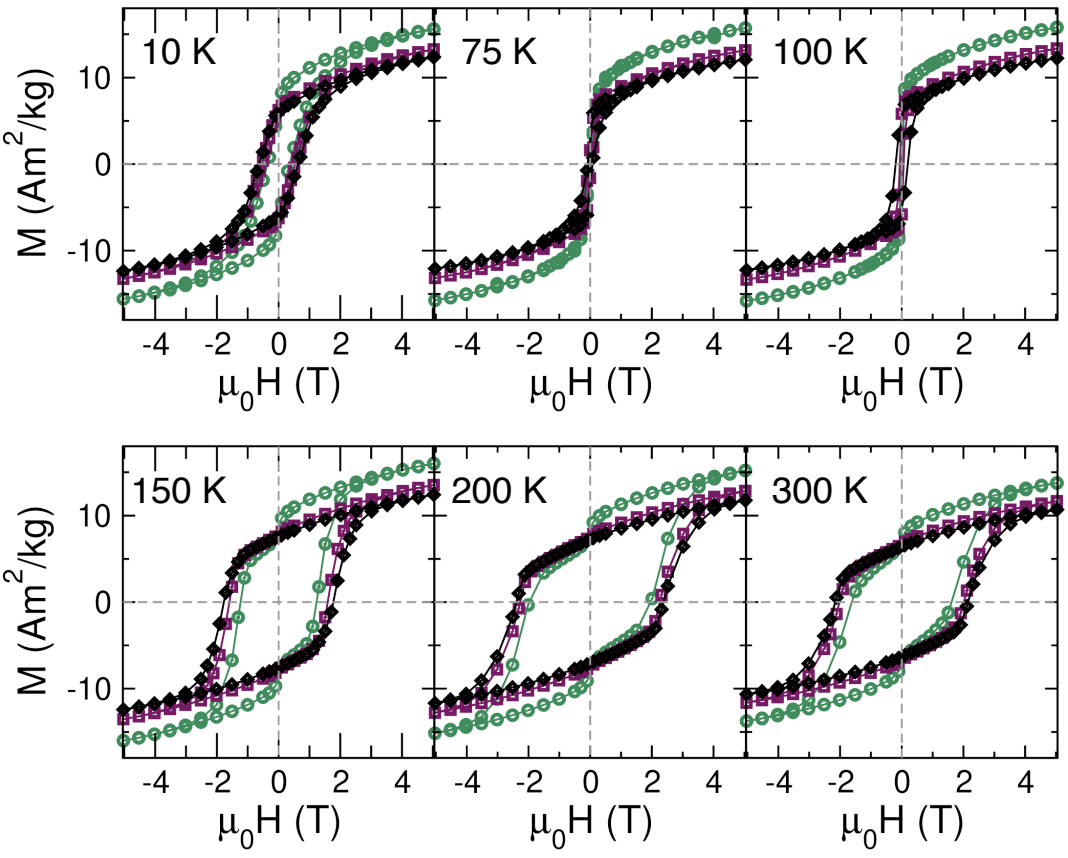

Figure 4.7: Hysteresis loops of 15 nm (green circles), 20 nm (purple squares) and 30 nm (black diamonds) ϵ-Fe_2O_3 nanoparticles at 10, 75, 100, 150, 200 and 300 K. Reprinted with permission from R Nickel, *et al.* Nano Letters, 2023. Copyright 2023 American Chemical Society.

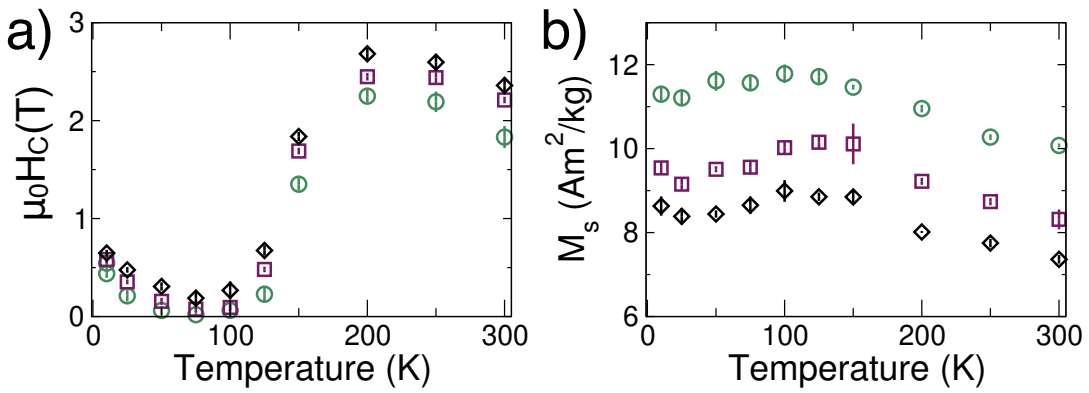

Figure 4.8: Temperature dependent coercive field ($\mu_0 H_C$) and d) magnetic saturation (M_S) of 15 nm (green circles), 20 nm (purple squares) and 30 nm (black diamonds) ϵ-Fe_2O_3 nanoparticles. Reprinted with permission from R Nickel, *et al.* Nano Letters, 2023. Copyright 2023 American Chemical Society.

component of the sample. Since these slopes do not vary significantly with either temperature or nanoparticle size, their removal affects the magnitude of M_S, but does not impact either the temperature or size dependences.

Overall, the temperature dependent behaviour of M_S and $\mu_0 H_C$ is identical between the different sizes. As the size of the ϵ-Fe_2O_3 nanoparticles increase, M_S decreases and $\mu_0 H_C$ increases. As with χ_{DC}, the decrease in $M_S(T)$ corresponds to the decrease in broken coordination as nanoparticle size increases. Different insights are obtained from $\mu_0 H_C(T)$ where the increases with increasing size indicates that the spin-orbit coupling (e.g. m_s/m_l)[49] is increased (discussed below).

4.4 Phase Transition

Magnetic characterization clearly reveals the transition between the low temperature incommensurate and high temperature ferrimagnetic phase. However, it does not

provide insights into the underlying mechanism that generates this phase transition. For better understanding, additional temperature dependent characterization of the ϵ-Fe_2O_3 nanoparticles is required.

First, temperature dependent x-ray diffraction is used to track the overall structure. Patterns were collected on the 15 nm ϵ-Fe_2O_3 nanoparticles while warming from 20 to 300 K on an Oxford Cryosystems PheniX closed cycle refrigeration stage. In the Reitveld refinements atomic positions and peak broadening were fixed, while the lattice parameters and 12-coefficient Chebychev background were fit. Refinements examined the effect of fitting atomic positions, but no significant changes were observed. Results are located in figure 4.9 and show linear expansion of the *b* and *c* axes upon warming from 20 K to 300 K, while the *a* axis exhibits reduced expansion below

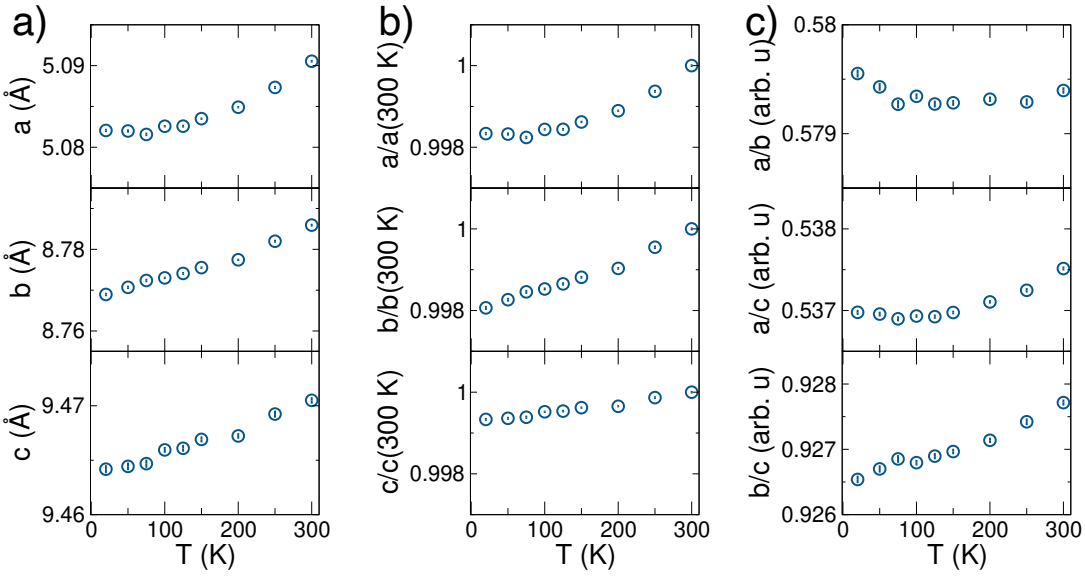

Figure 4.9: a) Temperature dependent lattice parameters of 15 nm ϵ-Fe_2O_3, b) lattice parameters normalized to 300 K, and c) unit cell parameter ratios. Reprinted with permission from R Nickel, *et al.* Nano Letters, 2023. Copyright 2023 American Chemical Society.

150 K. Such behaviour is consistent with the formation of Fe-O octahedral chains between DO_{h1} atoms along the a axis as pictured in figure 1.8b.

Note that these results differ from those reported in the literature which combine x-ray and neutron diffraction.[41,109] Because the XRD patterns reported here used a Cu anode, there is limited sensitivity to the O atoms in the crystal. Thus, the shifts in O atomic position reported by Gich et al.[41] could be present. Regardless, these results reveal considerably different temperature dependent lattice parameters than those of Tseng et al.,[109] where increased contraction in the c axis was observed between 75 and 150 K. The source of these differences is unclear, though variations in morphology or composition are most likely, particularly because the sample in reference 41 contained α-Fe_2O_3 and phase purity was not established in reference 109.

Again EXAFS is used as an improved local probe of the structure. The temperature dependent Fourier transformed EXAFS spectra of the 30 nm ϵ-Fe_2O_3 nanoparticles is shown in figure 4.10a. The same four path model described previously was

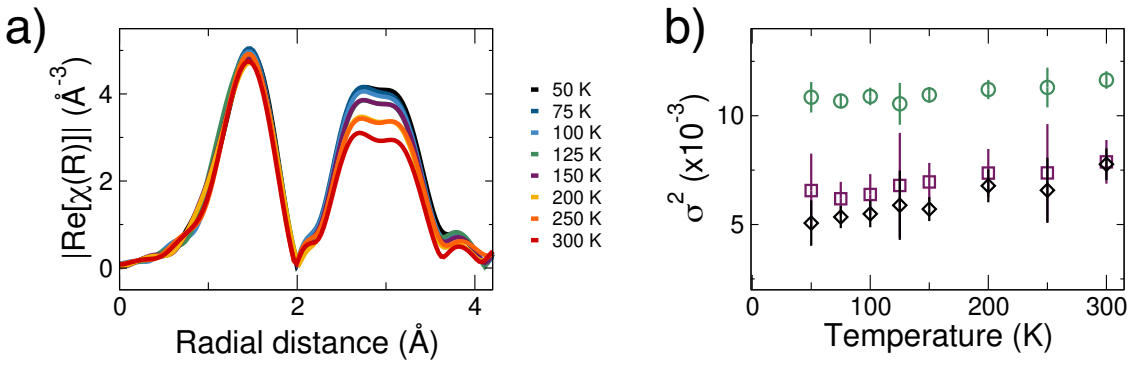

Figure 4.10: a) Temperature dependent Fourier transformed EXAFS spectra in real space of 30 nm ϵ-Fe_2O_3 nanoparticles. b) Debye-Waller parameters of Fe-O (green circles), Fe-Fe_1 (purple squares) and Fe-Fe_2 (black diamonds) paths as a function of temperature. Path length and multiplicities as listed in table 4.2.

used to fit the data; however, now the path multiplicities were fixed and the Debye-Waller parameters were fit. Alternative fits were explored where the path lengths were also fit; however, visual inspection of the spectra reveals this to be unnecessary as only the relative amplitudes of the peaks change with temperature and not their positions. The temperature dependent Debye-Waller parameters are shown in figure 4.10b, where all three increase linearly with increasing temperature. As this parameter reflects disorder in path length, such behaviour is a reflection of both the expansion of the crystal lattice observed via XRD and an increase in thermal energy of the individual atoms. Notably there is no evidence of a structural change in the temperature range where the phase transition is observed (between 100 and 150 K). In particular the absence of increased disorder in σ^2 of the Fe-O paths discredits the possibility of a shift in an O atomic position.

From the XRD and EXAFS analysis, there is no evidence that a structural transition underpins the magnetic transition. Thus we shift to XAS to study how the elemental coordination evolves as a function of temperature. Fe $L_{3,2}$ spectra of the three sizes at 50, 150, and 250 K are shown in figure 4.11. No significant differences are evident with respect to ϵ-Fe_2O_3 nanoparticle size at any of the measured temperatures.

Crispy[77] was used to simulate the Fe $L_{3,2}$ spectrum. Three components were used in the model, corresponding to the T_d, RO_h and DO_h sites and their relative contributions to the XAS spectrum were fixed at 1:1:2 in keeping with both the established structure and the experimental Mössbauer results. Within this constraint, simulation parameters were optimized to reproduce the line shape of both the XAS

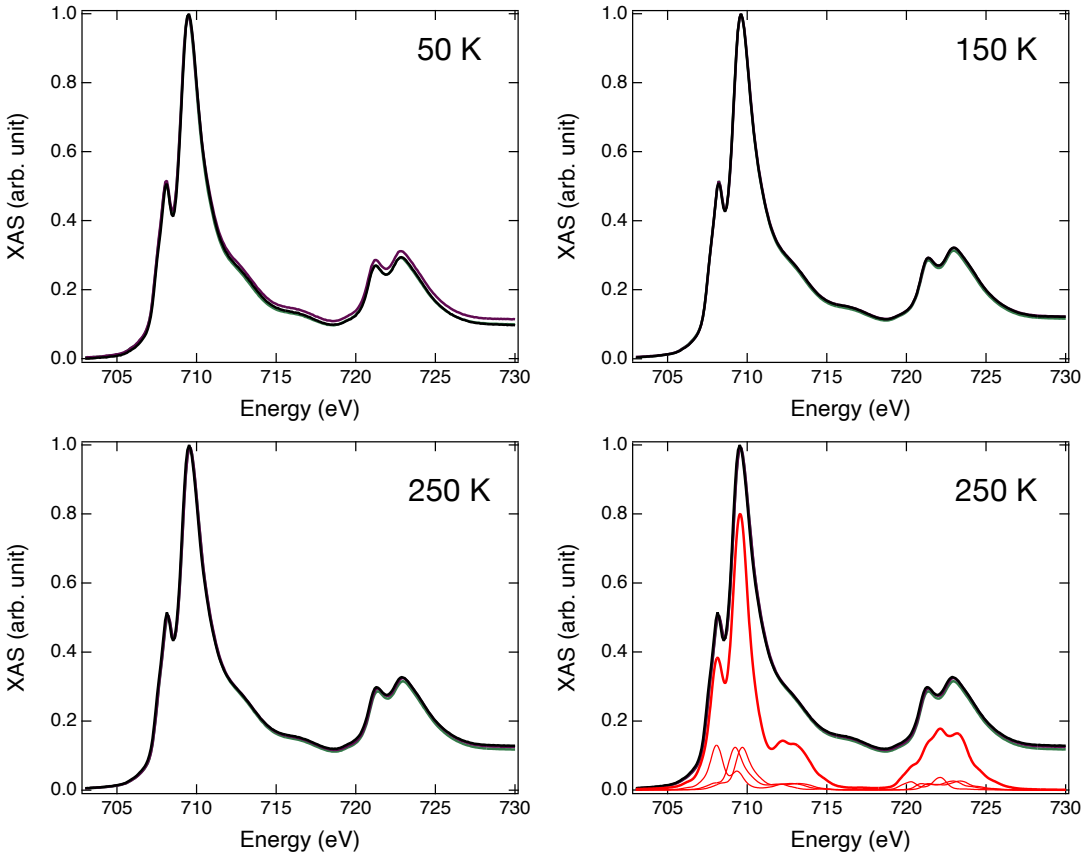

Figure 4.11: Fe $L_{3,2}$ spectra at 50, 150 and 250 K of 15 nm (green), 20 nm (purple) and 30 nm (black) nanoparticles. Simulated spectrum (reduced to 80% magnitude) is shown in red with individual components as described in the text.

and artifact-free XMCD spectra. For all three components the scale factor of the direct radial Slater integrals (F_k) were set to 75% of the atomic values. This reduction is used to approximate covalency effects, and is only slightly stronger than the 80% reduction used for simulating most $3d$ spectra. All components also used spin-orbit coupling scale factor (ζ) of 0.98 and Gaussian broadening with FWHM of 0.4 eV. Maximum amplitude of the T_d site is located at 708.1 eV, while the RO_h and DO_h are at 709.2 eV and 709.7 eV, respectively. Crystal field splitting ($10D_q$) of the T_d

site was determined to be 0.5 eV, while both O_h sites had $10D_q$ of 0.8 eV. This value is significantly smaller than ∼1.3 eV reported for both γ- and α-Fe_2O_3. Finally, the Slater parameter F_2, which describes the core hole ($2p$)-valence hole ($3d$) multipole interactions[112] was set to 40% of the *ab initio* atomic value (F_2=4.817 eV) for both O_h components. Such a reduction translates to weaker multiplet effects and is a sign of enhanced covalency at the O_h sites.[113] Overall the simulations reproduce the general shape of both the L_3 and the L_2 edges reasonably well. Mismatch in the region between these edges is attributed to hybridization and orbital intermixing – the simulation of which is beyond the scope of this work.[114]

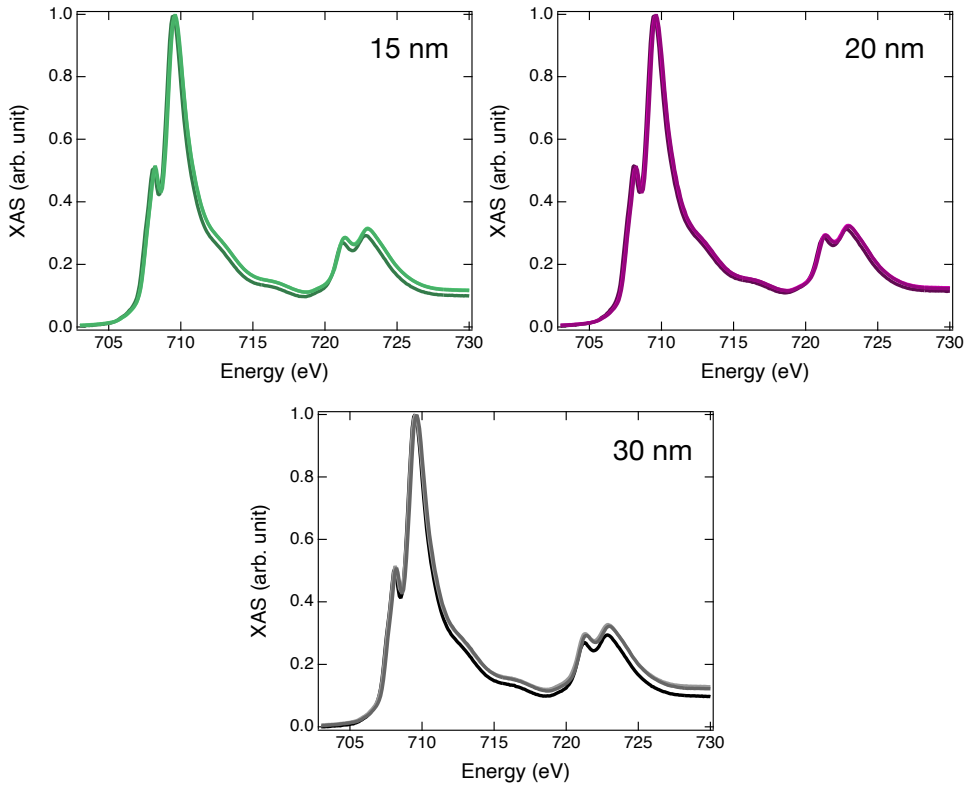

Figure 4.12: Fe $L_{3,2}$ spectra at 15 nm (green), 20 nm (purple) and 30 nm (black) nanoparticles at 50 K (dark), 150 K (medium) and 250 K (light).

Figure 4.12 shows the same Fe $L_{3,2}$ spectra as figure 4.11, displayed to better show how the spectra evolve as a function of temperature. Subtle changes are visible in the 150 and 250 K spectra compared to those at 50 K. The L_2 edges are shifted up in energy by ∼0.1 eV, and both $L_{3,2}$ edge tails are broadened. Such variations are consistent with with increased hybridization and orbital intermixing.[114]

The XAS-normalized XMCD spectra of the ϵ-Fe_2O_3 nanoparticles are located in figure 4.13. The line shape of all XMCD spectra are the same, and reproduced well by

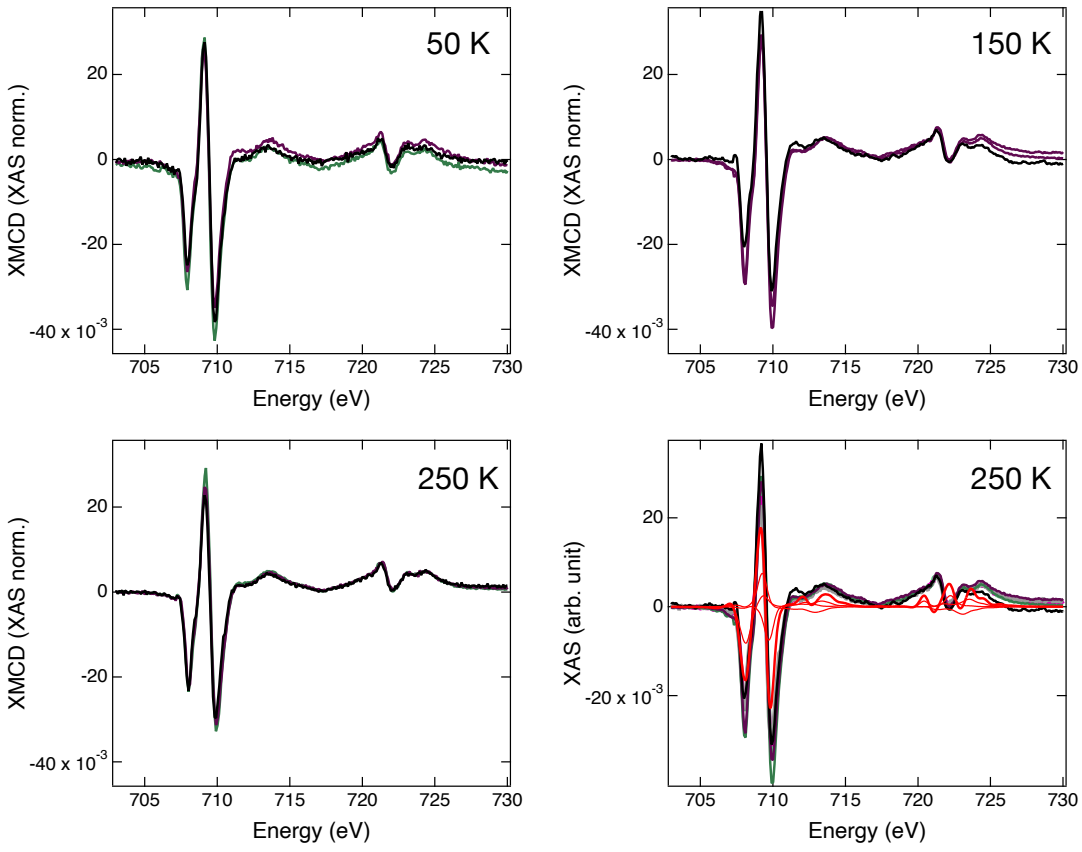

Figure 4.13: Fe $L_{3,2}$ spectra at 50, 150 and 250 K of 15 nm (green), 20 nm (purple) and 30 nm (black) nanoparticles. Simulated spectrum shown in red (reduced to 80% magnitude) with individual components as described in the text.

the simulation (shown in red). Unlike the XAS spectra, clear differences between the sizes are evident, with the amplitude of the features decreasing with increasing size. Such behaviour is consistent with bulk magnetometry measurements where reduced net magnetization with increasing size was observed.

In contrast to the subtle variations of the Fe $L_{3,2}$ edge, the O K edge changes significantly with both nanoparticle size and temperature. The spectrum can be divided into two overall regions – the first located from 528-532 eV reflects $2p - 3d$ hybridization and the second from 532-545 eV speaks to $2p - 4sp$ hybridization.[115] As shown in figure 4.14, both of these regions in the 50 K spectra are impacted by nanoparticle size. First, absorption in the $2p - 3d$ region decreases with increasing

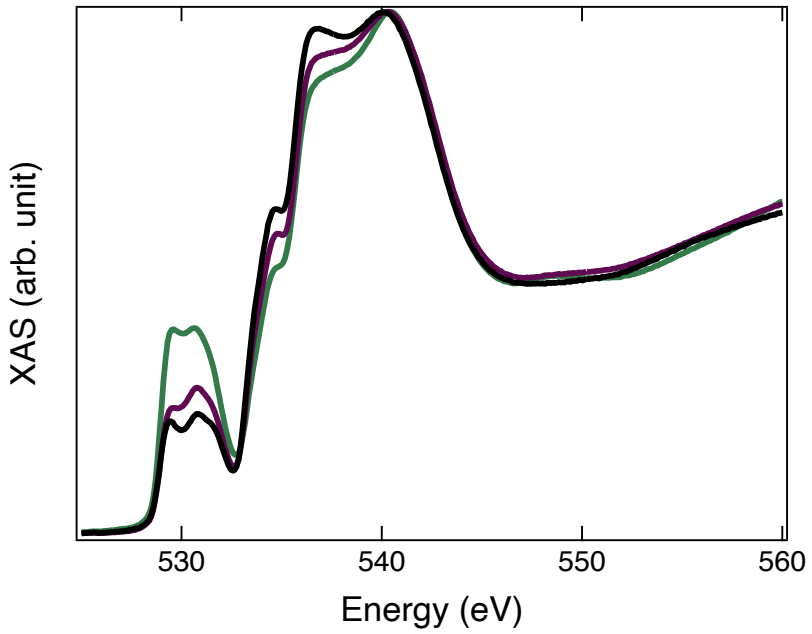

Figure 4.14: O K edge spectra of 15 nm (green), 20 nm (purple) and 30 nm (black) nanoparticles at 50 K. Reprinted with permission from R Nickel, *et al.* Nano Letters, 2023. Copyright 2023 American Chemical Society.

size with the relative absorption of 39% for the 15 nm particles, compared to 28% and 23% for the 20 nm and 30 nm. The $2p-4sp$ region shows the opposite behaviour with increasing absorption at both the 534.7 eV and 536.6 eV shoulders with increased particle size. Overall, these variations correspond to reduced $2p-3d$ and increased $2p-4sp$ hybridization as the size of the ϵ-Fe_2O_3 nanoparticles are increased. Such behaviour is consistent with the 10 K Mössbauer hyperfine parameters, and is a possible signature of longer range ordering along the O_h site chains.

As the temperature increases, figure 4.15 shows that the O K edge evolves for all three sizes in three stages. These changes are most obvious for the 15 nm particles. The 50 and 75 K spectra are nearly identical – indicating that the Fe-O hybridization in the low temperature incommensurate phase is stable. At 100 K the absorption of the $2p-3d$ peak is significantly reduced, with the maximum amplitude shifted to higher energy as the low temperature phase electronic structure is weakened and new $2p-3d$ hybridization is established. Further increases in temperature strengthen this hybridization as revealed by increased absorption of the $2p-3d$ region in the 125 K and 150 K spectra. Above 150 K, the O K edge spectra look dramatically different. Absorption in the $2p-3d$ hybridization region is further increased and the shoulders at 534.7 eV and 536.6 eV in the $2p-4sp$ region that showed a size dependence are reduced. Most interestingly, the main peak at 539.6 eV appears broadened due to substantial absorption at 547 eV. Overall, these high temperature spectra indicate strong Fe-O hybridization –both of $2p-3d$ and $2p-4sp$ nature in the ferrimagnetic phase.

Thus far, it has been established that the magnetic transition corresponds to

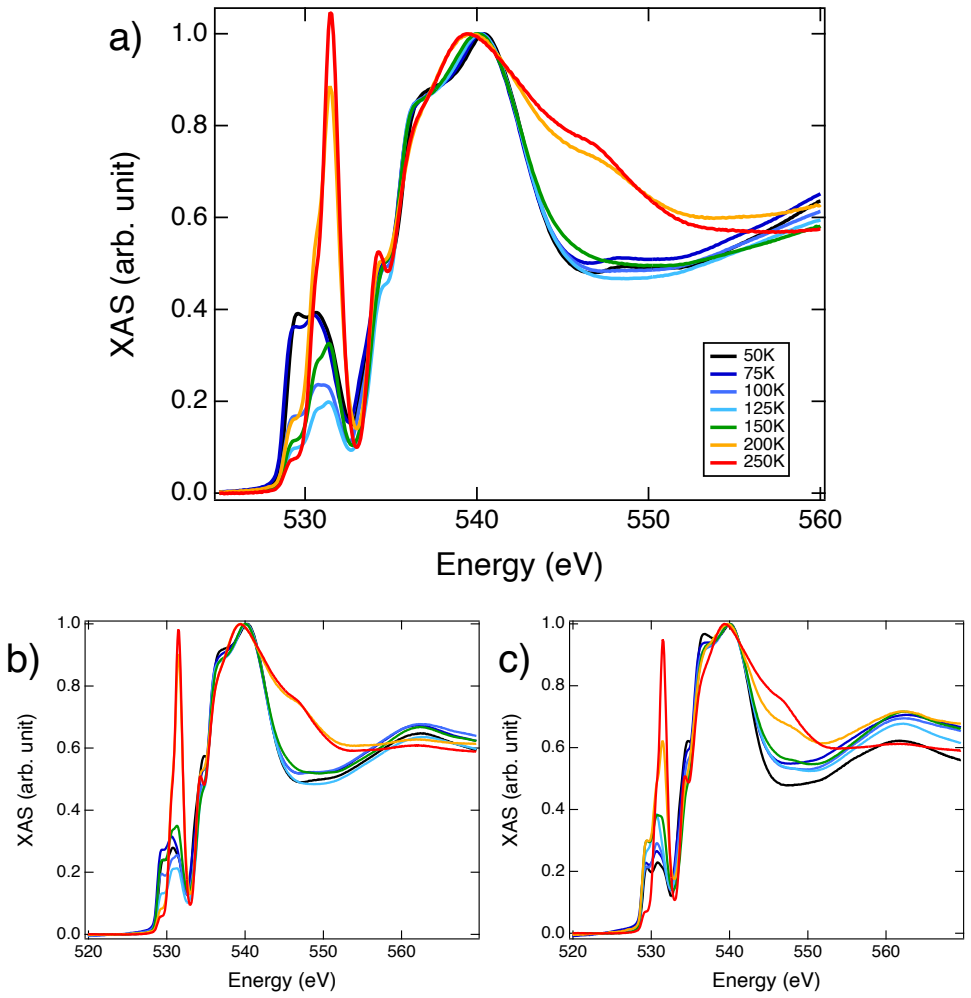

Figure 4.15: O K edge spectra of a) 15 nm, b) 20 nm and c) 30 nm nanoparticles at 50 K (black), 75 K (navy blue), 100 K (blue), 125 K (light blue), 150 K (green), 200 K (orange) and 250 K (red).

changes in Fe-O hybridization with no sign of any structural transition. However, after exposure to a 4 T magnetic field, the XAS O K edge TEY data shown in figure 4.16 reveal surprising behaviour. These spectra are normalized to the incident beam (I0) to minimize beam effects, but not to the maximum spectral amplitude. Note that the horizontal position of the beam on the sample was kept constant, while the vertical position was chosen to maximize the TEY signal. To account

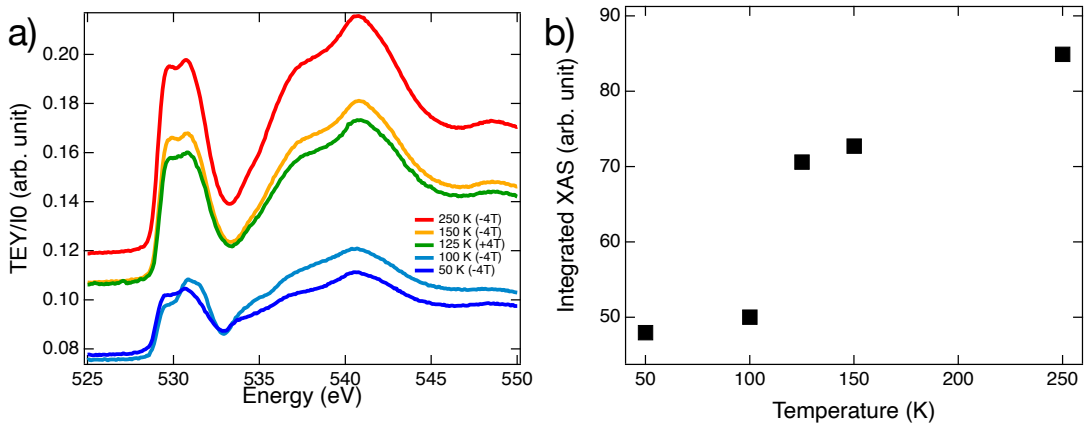

Figure 4.16: a) O K edge XAS spectra of 15 nm ϵ-Fe_2O_3 nanoparticles at 50 K (dark blue), 100 K (light blue), 125 K (green), 150 K (yellow) and 250 K (red) normalized only to I0. b) Integrated XAS signal (TEY/I0) as a function of temperature, measured in 4 T magnetic field.

for contraction of the copper sample holder with temperature, the optimal vertical position was verified at each temperature. With these considerations taken, we are confident that the differences in the TEY signal are real. As such, the discontinuity in the integrated XAS spectra between 100 K and 125 K in figure 4.16b is the result of a change in the electric conductivity of the ϵ-Fe_2O_3. The insulating behaviour at low temperatures was particularly apparent during flying scan data acquisition as sample charging caused rapid deterioration of the scan quality. Overall, from these results ϵ-Fe_2O_3 undergoes a metal-insulator transition in addition to its well-reported change in magnetic behaviour.

These insights indicate that further tracking of the local environment of the Fe ions is necessary and so temperature dependent Mössbauer spectroscopy was done to observe how the local Fe environment evolves through the magnetic transition. From these spectra, the relative absorption (or f-factor) was calculated to quantify

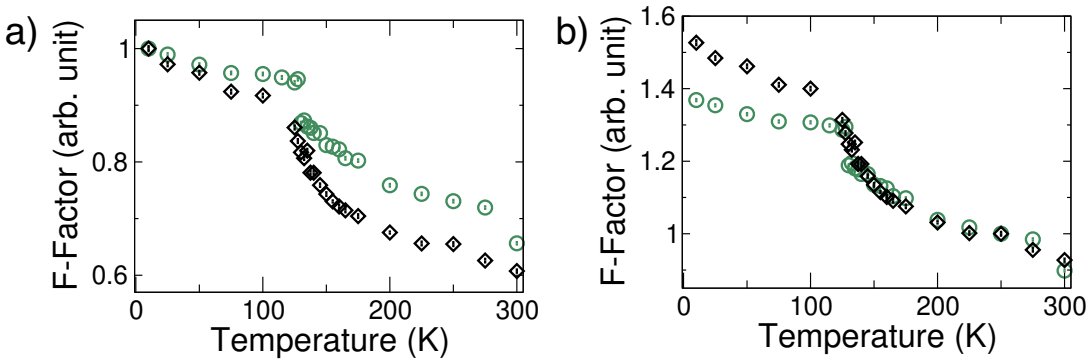

Figure 4.17: Temperature dependent f-factor of 15 nm (green circles) and 30 nm (black diamonds) ϵ-Fe_2O_3 nanoparticles normalized to a) 10 K and b) 250 K. Reprinted with permission from R Nickel, *et al.* Nano Letters, 2023. Copyright 2023 American Chemical Society.

resonant photon absorption. Figure 4.17 shows the temperature dependent f-factor of the 15 nm and 30 nm ϵ-Fe_2O_3 nanoparticles, normalized to the 10 K values. Both sizes exhibit a decrease in f-factor at 127.5 K upon warming courtesy of the transition, coinciding with the change in conductivity. Such behaviour reflects the changing electronic structure and Fe-O hybridization impacting the lattice vibrational modes. A similar change in the temperature dependent f-factor was observed in chapter 3 for the Verwey transition in Fe_3O_4.

With this conventional normalization to the base temperature spectrum, the 30 nm sample exhibits a reduced f-factor compared to that of the 15 nm in the high temperature phase. Note that this observation is entirely dependent on the f-factor normalization and assumes that the 10 K vibrational modes are comparable between the two sizes and that they evolve to different high temperature states. In light of the O K edge XAS spectra that reveal identical Fe-O hybridization at 250 K and sizeable differences at 50 K, this assumption is probably not appropriate.

Thus, a different normalization scheme could be considered where the f-factor data is rescaled to reflect the similar hybridization at 250 K. With this model (shown in figure 4.17b), the f-factor of the 30 nm particles in the incommensurate phase becomes larger than that of the 15 nm particles, while the high temperature values are comparable. Such an increase in low temperature f-factor would be the natural consequence of the enhanced hybridization observed in the 30 nm particles.

In addition to the f-factor quantification, the temperature dependent Mössbauer spectra were fit to obtain their hyperfine parameters. Figure 4.18 shows δ, Δ and B_{hf} for the 15 nm and 30 nm particles. The overall temperature dependence is similar to that reported by reference 48 which examined ϵ-Fe_2O_3 nanoparticles that were synthesized using a similar method. However, the observed transition is sharper than other reports,[41,46–49] and reveals new insights into the local environment of the T_d sites through the transition. The isomer shifts (δ) of both the DO_h and RO_h sites are in agreement throughout the measured temperatures, and are consistent with the Fe^{3+} identified from the XAS spectra. Unlike the O_h sites, the T_d isomer shift changes significantly with temperature. Below 150 K δ_{Td} is relatively constant with values $\sim$0.32 mm/s as expected for tetrahedral Fe^{3+}.[69] As the temperature increases, δ_{Td} first decreases to 0.13 ± 0.03 mm/s at 132.5 K, then increases to 0.24 ± 0.1 mm/s at 150 K. These shifts represent changes to the electronic density at the nucleus, with δ decreasing as d electrons are pulled away from the nucleus and vice versa. Further warming above 150 K causes a gradual decrease in δ_{Td} in keeping with the second order doppler shift.

The quadrupole splitting (Δ) of the three components provides further insights.

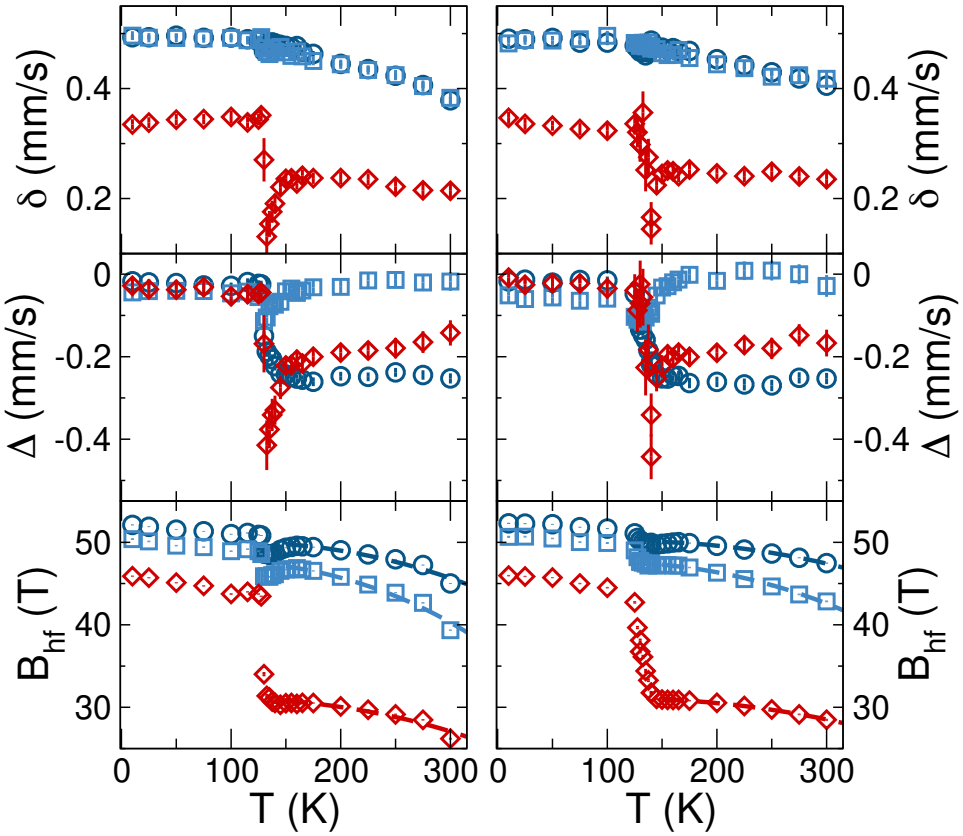

Figure 4.18: Temperature dependent isomer shift (δ, top), quadrupole splitting (Δ, centre) and hyperfine field (B_{hf}, bottom) of 15 nm (left) and 30 nm (right) ϵ-Fe_2O_3. DO_h, RO_h and T_d sites shown as dark blue circles, light blue squares and red diamonds, respectively. Dashed lines in B_{hf} panels show Brillouin fit. Reprinted with permission from R Nickel, *et al.* Nano Letters, 2023. Copyright 2023 American Chemical Society.

Below 130 K, all sites have very small Δ, indicating that the electronic environment around the Fe nuclei is isotropic. Immediately above 130 K, the behaviour of Δ_{Td} matches that of δ_{Td} with a rapid decrease to -0.41 ± 0.06 mm/s at 132.5 K and subsequent increase to -0.22 ± 0.02 mm/s at 150 K. Because Δ quantifies the electric field gradient, this temperature dependent behaviour describes the asymmetry introduced by the pulling away of electrons and increased symmetry from their return.

Unlike δ, Δ of both the octahedral components are impacted by the transition with Δ_{DOh}decreasing to -0.24 ± 0.01 mm/s at 150 K, while Δ_{ROh} decreases slightly at 132.5 K to -0.11 ± 0.02 mm/s before returning to -0.04 ± 0.02 mm/s at 150 K. Overall, the behaviour of δ and Δ creates a picture of the T_d electrons being rearranged as the system undergoes its phase transition, causing minor perturbations at the RO_h site and lasting distortions to the DO_h.

Unlike the other hyperfine parameters, the temperature dependence of B_{hf} does not show the two-stage transition. Instead the temperature dependence follows that of previous reports, where $B_{hf,Td}$ drops significantly with the phase transition to $\sim$30 T.[41,46–49] This value is unusually low for high spin Fe^{3+}, and instead speaks to an intermediate spin state, caused by the same spin-orbit coupling that yields the gigantic $\mu_0 H_C(T)$ of the ferrimagnetic phase. Brillouin fits of B_{hf} (>150 K) were used to estimate the Curie temperatures (T_C) of the three sites. The DO_h site has the highest T_C of 590 ± 20 K, while RO_h and T_d sites have 490 ± 10 K and 520 ± 20 K, respectively. Because T_C is directly proportional to exchange coupling J_0, this means that the strongest coupling occurs for DO_h sites, followed by T_d and RO_h. This large DO_h coupling compared to RO_h explains why Δ_{DOh} is impacted by the electronic rearrangement of the T_d sites.

Overall, the 30 nm particles show the same temperature dependences as the 15 nm particles; however, the transition extends over a wider range of temperatures. This difference is most evident when comparing the decreases of $B_{hf,Td}$ in figure 4.18. Though the transition begins for both samples at 127.5 K, $B_{hf,Td}$ for the 15 nm particles stabilizes at 132.5 K compared to 140 K for the 30 nm particles. This extended

transition is a consequence of the increased Fe-O hybridization in the low temperature incommensurate phase which then requires more thermal energy to transform into the ferrimagnetic phase. Additionally, T_C of all sites are increased for the 30 nm particles compared to the 15 nm ones, with T_C of the DO_h, RO_h and T_d being ∼680 K, ∼550 K and ∼600 K, respectively. Such an increase is consistent with reduced spin disorder from finite size effects.

4.5 Summary

In order to gain new insights into the physics that controls the ϵ-Fe_2O_3 phase, we have examined three sizes of ϵ-Fe_2O_3 nanoparticles, nominally 15 nm, 20 nm and 30 nm. The aim of this approach is to decouple the impact of nanoparticle morphology from microstructure effects, since all nanoparticles were synthesized using the same method. X-ray diffraction (XRD) and extended x-ray absorption fine structure (EXAFS) reveal that the samples are structurally identical; however, low temperature Mössbauer spectroscopy and O K edge x-ray absorption spectroscopy (XAS) show changes to Fe-O hybridization with nanoparticle size. At 250 K, the size differences disappear as all spectra change significantly as both $2p - 3d$ and $2p - 4sp$ hybridization is altered. Interestingly, the overall magnetic properties are not impacted by the size-dependent hybridization at low temperatures. Instead, the reduced magnetic saturation (M_S) and χ_{DC}, and increased $\mu_0 H_C$ with increasing sample size are a result of finite size effects since broken coordination is present with increasing degree as the nanoparticles get smaller, and the O-Fe-O octahedral chains of the perovskite structure are shortened. Temperature dependent Mössbauer spectroscopy

results present trends similar to other studies; however, we find that the transition between low and high temperature phases is much sharper and the T_d site undergoes two distinct electronic changes in contrast to the monotonic transformations reported previously in smaller nanoparticles.[41,48,49] This multistage transition corresponds to electrons first pulling away from the T_d site as the transition is approached from low temperatures, and then returning with further warming, evidenced by changes to the isomer shift and quadrupole splitting. This rearrangement of the electronic structure around the T_d site also has a lasting impact on the DO_h component as the system stabilizes into its high temperature phase. Compared to the 15 nm particles, the transition of the 30 nm ϵ-Fe_2O_3 shifts to a higher temperature, indicating that the altered Fe-O hybridization strengthens the low temperature phase, likely due to comparatively longer Fe-O octahedral chains present in the larger particles. Overall, this research highlights the importance of transition metal-oxygen hybridization to the mechanisms underlying the interesting properties such as phase transitions and the multiferrocity of perovskites.

Chapter 5

Transition Metal-Doped ϵ-Fe_2O_3

Chapter 4 identified the importance of Fe-O hybridization to the properties of ϵ-Fe_2O_3 and showed that the T_d site drives the magnetic transition. While the temperature dependent Mössbauer hyperfine parameters show that the changes to the T_d site impact the DO_h component, it is unclear which of the DO_h sites is affected and how. Simply studying the ϵ-Fe_2O_3 phase does not provide further insights. To obtain a more complete picture, another approach is required. Controlled disruptions of both the crystal structure and the electronic interactions can be produced by doping ϵ-Fe_2O_3 nanoparticles with other ions. Doped ϵ-Fe_2O_3 nanoparticles have previously been studied with an overall goal of optimizing their properties for applications such as millimeter-wave absorption and magnetic recording media.[116–120] However, such a focus narrows the species of ions used to dope, with rare earth ions (Ga and In), and d^0 transition metals (Al and Ti) attracting the most interest. Because this study aims not to enhance particular properties but to better understand the physics that underpin the ϵ-Fe_2O_3 phase a more systematic approach will be used. To systemat-

ically perturb the ϵ-Fe_2O_3 phase and identify how the overall behaviour is impacted by variations in both dopant species and concentration, ϵ-Fe_2O_3 nanoparticles doped with transition metal ions Cr, Mn, Co, Ni, Cu and Zn are studied.

5.1 Overview of Transition Metal-doped ϵ-Fe_2O_3

5.1.1 Valence & Coordination

Characterization of all the transition metal-doped ϵ-Fe_2O_3 nanoparticles was performed to identify the impact of both the dopant species and dopant concentration. Room temperature XRD patterns were collected to track the evolution of the crystal structure. All XRD patterns are shown in figure 5.1. Reitveld refinements were done using the structure described in reference 41 with space group $Pna2_1$. Atomic positions were fixed and full occupancy was assumed. Lattice parameters, reflection broadening and a Chebychev background were fit for each pattern.

The ϵ-Fe_2O_3 structure describes low doping levels quite well, while deviations become evident with higher doping amounts. Notably as the dopant concentration increases, the relative amplitudes of the reflections at 35.3° and 36.7° change as the 35.3° intensity increases and the reflection broadens. Figure 5.2 shows the refined patterns with residuals for the 1% and 12% Cr-doped samples for comparison. The residuals of the 12% pattern clearly reveal reflections that are not described by the orthorhombic structure of ϵ-Fe_2O_3. Instead, these new reflections are consistent with a spinel structure, and indeed an improved fit of the pattern can be obtained with the inclusion of a secondary spinel phase (see figure 5.2). Note that this two-phase model still does not describe the diffraction pattern well. Further efforts into identifying

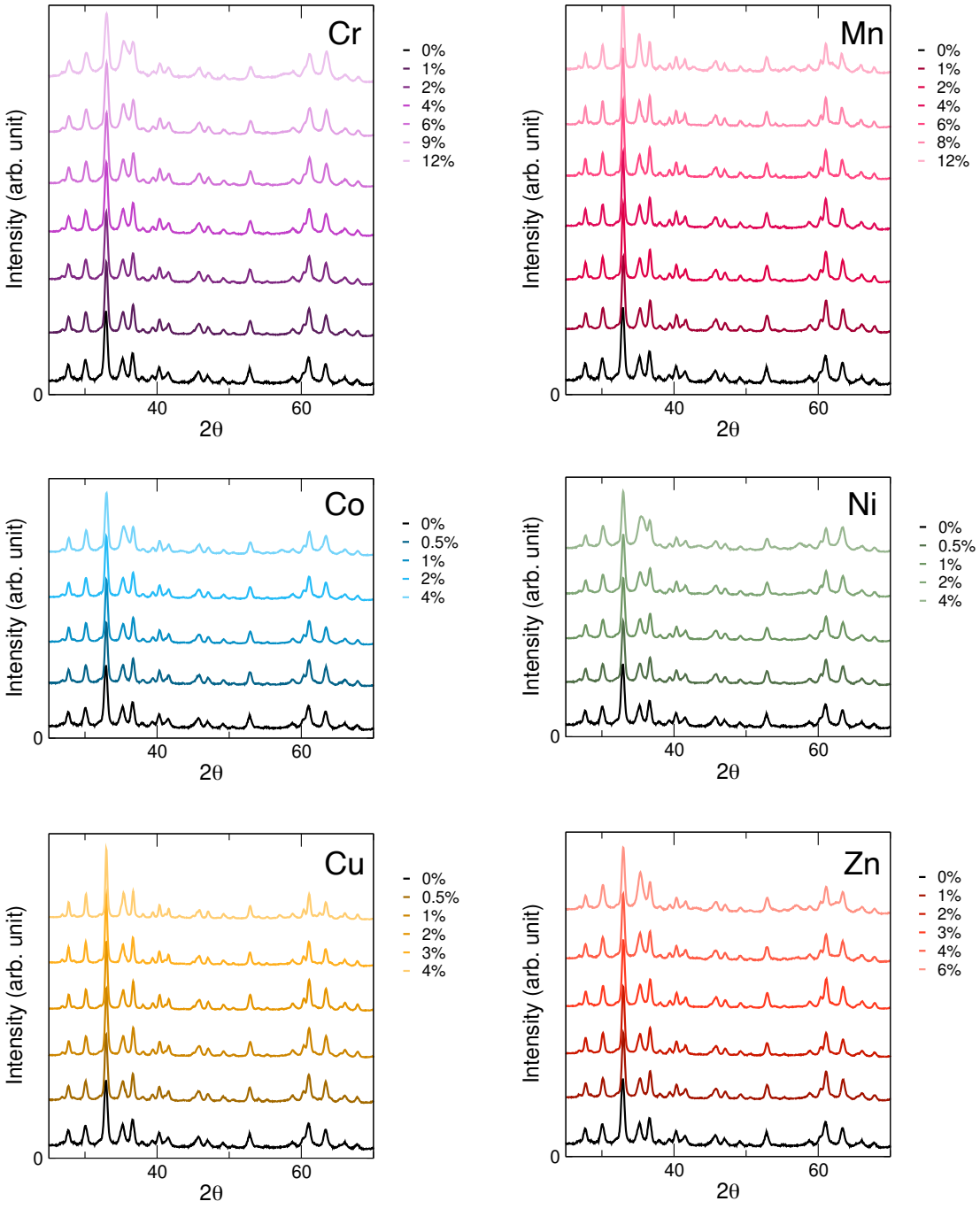

Figure 5.1: Room temperature XRD patterns of transition metal-doped ϵ-Fe_2O_3 nanoparticles.

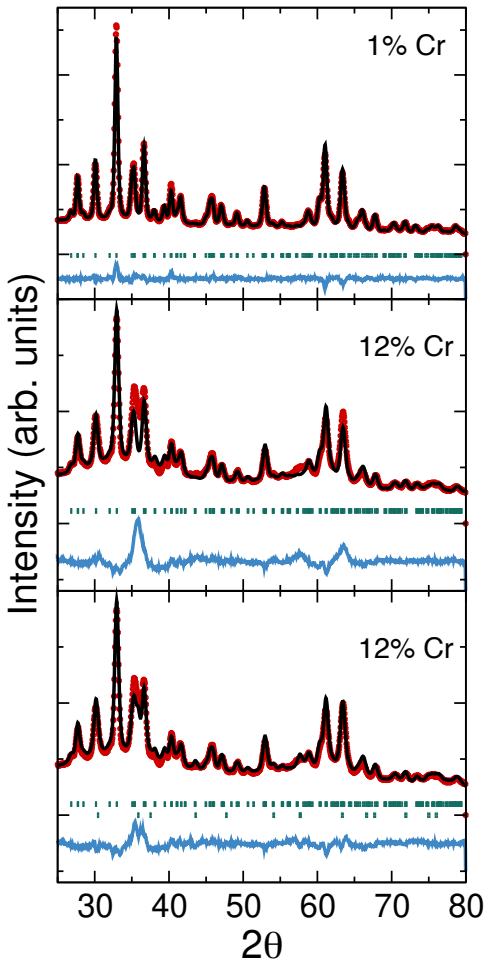

Figure 5.2: Refined XRD patterns of 1% (top) and 12% (centre) Cr-doped ϵ-Fe_2O_3 nanoparticles. Red markers are data and black line indicates fit. The green Bragg markers index the $Pna2_1$ structure while the blue is the residuals of the refinement. Bottom panel shows 12% Cr-doped ϵ-Fe_2O_3 pattern refined with $Pna2_1$ and spinel $Fd\bar{3}m$ spacegroups.

a single space group that would generate a pattern consistent with that measured proved unsuccessful. Local distortions around the dopant ions are the most likely cause of this change in the diffraction patterns.

To gain insights into which site the dopant ions are entering, additional Reitveld analysis was performed. Lattice parameters, background and peak broadening were

fixed to the results of the previous refinements, while dopant ions were incorporated into the structure. Full doping into a single Fe site was assumed and the resulting χ^2 are tabulated.

Table 5.1a tracks how χ^2 varies as Cr ions are substituted into the various Fe sites. Because all χ^2 are reduced when Cr is assumed to enter the DO_{h1} site, this is the most likely location for the dopant ion, although the T_d site is also a possibility. Additionally, the reduction in χ^2 of the RO_h site for the highest concentrations of dopant ions could indicate that the Cr occupies multiple sites. For example, the dopant ions will enter the DO_{h1} site until a critical concentration is achieved, then begin to enter the RO_h site.

Results for similar Reitveld analysis of the Mn-doped ϵ-Fe_2O_3 nanoparticles are located in table 5.1b. The changes in χ^2 are relatively small, though the consistent reduction in χ^2 indicates that the DO_{h2} or T_d sites are the most probable sites for Mn-doping.

% Cr	—	DO_{h1}	DO_{h2}	RO_h	T_d
1	8.431	**8.430**	**8.425**	8.435	**8.425**
2	6.065	**6.062**	**6.064**	6.066	**6.056**
4	8.794	**8.785**	8.796	8.800	**8.782**
6	12.00	**11.98**	12.02	12.01	**11.97**
9	33.47	**33.41**	33.57	**33.46**	**33.45**
12	73.64	**73.55**	73.89	**73.58**	73.67

(a) Cr-doped ϵ-Fe_2O_3

% Mn	—	DO_{h1}	DO_{h2}	RO_h	T_d
1	4.107	4.107	**4.105**	4.110	**4.105**
2	5.974	5.975	**5.971**	5.981	**5.969**
4	4.153	4.154	**4.150**	4.160	**4.149**
6	7.585	7.590	**7.580**	7.594	**7.583**
8	9.823	9.833	**9.822**	9.826	**9.821**
12	24.53	24.56	24.56	**24.51**	24.54

(b) Mn-doped ϵ-Fe_2O_3

Table 5.1: χ^2 for Reitveld analysis of Cr- and Mn-doped ϵ-Fe_2O_3 XRD patterns when theoretical model incorporates full doping into a single site. Bolded values indicate that χ^2 with dopant in a particular site is reduced compared to the fit without any dopant ions included (—).

% Co	—	DO_{h1}	DO_{h2}	RO_h	T_d
0.5	3.089	**3.088**	**3.088**	**3.088**	3.089
1	10.51	10.51	10.51	10.51	10.51
2	9.756	**9.752**	**9.752**	**9.750**	**9.753**
4	55.35	**55.34**	**55.34**	**55.34**	**55.34**

(a) Co-doped ϵ-Fe_2O_3

% Ni	—	DO_{h1}	DO_{h2}	RO_h	T_d
0.5	4.603	**4.602**	**4.602**	**4.602**	**4.602**
1	10.86	**10.85**	**10.85**	**10.85**	**10.85**
2	16.06	**16.05**	**16.05**	**16.05**	**16.05**
4	143.5	143.5	143.5	143.5	143.5

(b) Ni-doped ϵ-Fe_2O_3

Table 5.2: χ^2 for Reitveld analysis of Co- and Ni-doped ϵ-Fe_2O_3 XRD patterns when theoretical model incorporates full doping into a single site. Bolded values indicate that χ^2 with dopant in a particular site is reduced.

Tables 5.2a and 5.2b tabulate the variations of χ^2 for the Retiveld analysis when the dopant ion is incorporated into various sites. Unlike the Cr- and Mn-doped ϵ-Fe_2O_3 nanoparticles, no site preference is identifiable from this analysis for the Co- and Ni-doped ϵ-Fe_2O_3 nanoparticles. The results for the Cu-doped nanoparticles in table 5.3a are only slightly more variable than the Co- and Ni-doped ones. Consistent improvement in χ^2 with T_d site doping suggests that this site is preferable; however, the DO_{h1} is also a possibility.

% Cu	—	DO_{h1}	DO_{h2}	RO_h	T_d
0.5	5.558	**5.557**	5.561	5.562	**5.554**
1	5.454	5.457	5.465	5.476	**6.434**
2	6.101	6.125	6.136	6.158	**6.081**
3	13.19	**13.17**	13.22	13.20	**13.15**
4	52.11	**52.06**	52.17	52.12	**52.05**

(a) Cu-doped ϵ-Fe_2O_3

% Zn	—	DO_{h1}	DO_{h2}	RO_h	T_d
1	4.435	4.439	4.440	4.459	**4.428**
2	25.10	**25.09**	25.12	25.13	25.14
3	8.211	8.230	8.243	8.305	**8.179**
4	22.77	**22.59**	**22.57**	**22.56**	**22.57**
6	100.7	100.7	**110.5**	**110.5**	100.8

(b) Zn-doped ϵ-Fe_2O_3

Table 5.3: χ^2 for Reitveld analysis of Cu- and Zn-doped ϵ-Fe_2O_3 XRD patterns when theoretical model incorporates full doping into a single site. Bolded values indicate that χ^2 with dopant in a particular site is reduced.

Table 5.3b tabulates the variations in χ^2 as Zn ions occupy different sites. For the lower doping concentrations (<4%), no clear improvements in χ^2 are evident; however, the increases that occur when the Zn ions occupy RO_h site indicate that this site is less preferable. Reduced χ^2 for higher Zn-doping into the RO_h sites does make the overall picture inconsistent. The DO_{h1} and T_d seem to be more likely sites; however, no firm conclusions can be drawn for this series from Reitveld analysis . A summary of the possible doping sites based on Reitveld analysis is located in table 5.4.

The XAS $L_{3,2}$ edge spectra were collected for all transition metal dopant ions to provide complementary information about the dopant ions' valence and coordination. As seen in figure 5.3, all the Cr $L_{3,2}$ spectra have the same line shape, indicating that the Cr ions have the same valence and coordination regardless of dopant concentration. The differences in the spectra, particularly the sloping background, are attributed to poor signal-to-noise for low concentrations of Cr. Multiplet simulations were performed using Crispy[77] to identify the valence and coordination of the Cr

Table 5.4: Summary of possible doping sites of transition metal-doped ϵ-Fe_2O_3 nanoparticles based on Reitveld analysis. ↑↑ denotes highly probable site, ↑ denotes probable site, and – is unclear.

Dopant	DO_{h1}	DO_{h2}	RO_h	T_d
Cr	↑↑	–	–	↑↑
Mn	–	↑↑	–	↑↑
Co	–	–	–	–
Ni	–	–	–	–
Cu	↑	–	–	↑
Zn	–	–	–	–

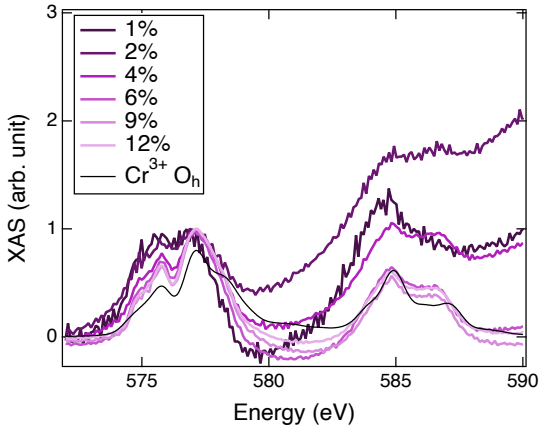

Figure 5.3: Cr $L_{3,2}$ edge XAS spectra of the Cr-doped ϵ-Fe_2O_3 nanoparticles collected at 50 K with simulated spectra.

ions. Spectra are well-reproduced by Cr^{3+} in O_h coordination with $10Dq = 2.0$ eV and ligand-metal charge transfer parameters $\Delta = 1.0$ eV and $V_{eg} = 2.0$ eV. Note that this charge sharing reflects the more ionic nature of the Cr-dopant ions, in contrast to the Fe^{3+}, which required reduced Slater parameters due to the high degree of covalency in ϵ-Fe_2O_3 (see Section 4.4 for further discussion). There is no evidence that Cr enters the T_d sites, in spite of the slightly improved Reitveld analysis. Instead, we conclude the Cr ions occupy the DO_{h1} sites.

Figure 5.4 shows the Mn $L_{3,2}$ edge spectra, which all share the same general features, indicating similar valence and coordination. The lowest concentrations of Mn (1% and 2%) both show reduced amplitude at 641 eV, compared to the ϵ-Fe_2O_3 doped with higher concentrations of Mn. Figure 5.4 shows the simulated spectra for the 12% Mn nanoparticles composed of 67% Mn^{2+} O_h with $10Dq = 0.5$ eV and ligand-metal charge transfer parameters $\Delta = 1.0$ eV and $V_{eg} = 2.0$ eV, and 33% Mn^{3+} O_h with $10Dq = 2.0$ eV with the same charge transfer parameters. The decreased

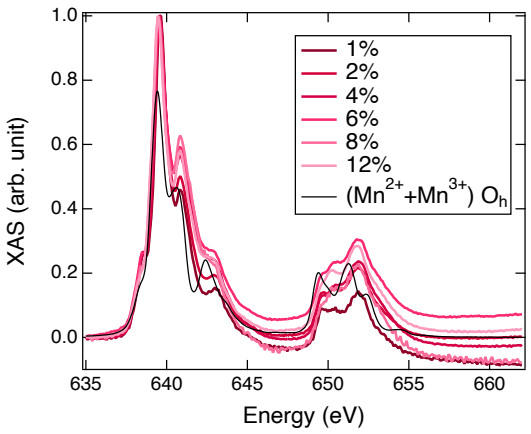

Figure 5.4: Mn $L_{3,2}$ edge XAS spectra of the Mn-doped ϵ-Fe_2O_3 nanoparticles collected at 50 K with simulated spectra.

shoulder observed for low Mn concentrations corresponds to a reduced fraction of Mn^{3+} O_h. Based on the O_h coordination and the Reitveld analysis, the Mn ions occupy the DO_{h2} sites.

The Co $L_{3,2}$ edge spectra have the same line shape for all of the Co-doped ϵ-Fe_2O_3 (see figure 5.5), with the exception of the 0.5% Co-doped spectrum which contains

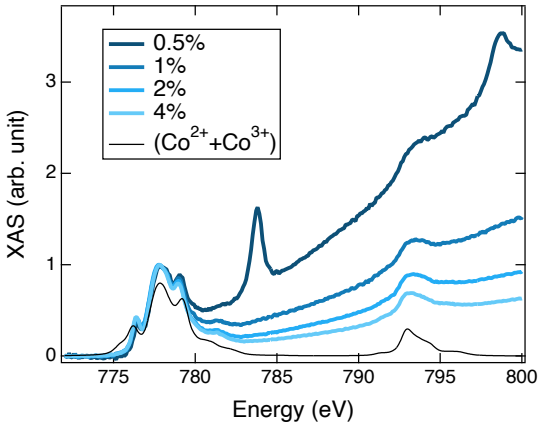

Figure 5.5: Co $L_{3,2}$ edge XAS spectra of the Co-doped ϵ-Fe_2O_3 nanoparticles collected at 50 K with simulated spectra.

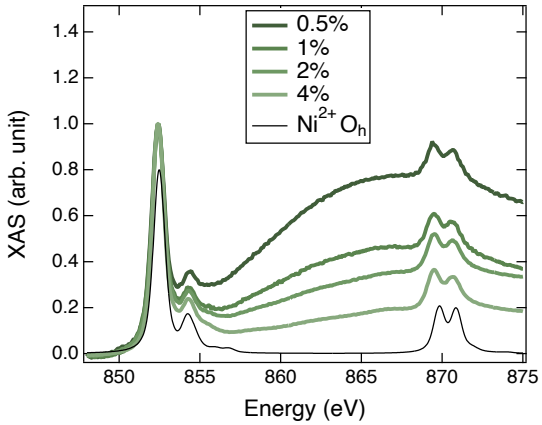

Figure 5.6: Ni $L_{3,2}$ edge XAS spectra of the Ni-doped ϵ-Fe_2O_3 nanoparticles collected at room temperature with simulated spectra.

features at 784 eV and 799 eV. Because these features only appear for the lowest concentration of Co which had a weakest signal, they are most likely artifacts from the beamline. Al is a possible source with an x-ray absorption edge at 1559.6 eV,[121] which is approximately double the energy of the observed feature. The Co $L_{3,2}$ edge spectra were simulated with equal parts Co^{3+} and Co^{2+}, both having O_h coordination with $10Dq = 1.3$ eV.

Figure 5.6 shows the Ni $L_{3,2}$ edge spectra at room temperature. As with the Co-doped ϵ-Fe_2O_3 nanoparticles, the background flattens with increasing dopant concentration as the overall signal improves. The Ni $L_{3,2}$ edge spectra are best simulated using a single Ni^{2+} component in O_h coordination with $10Dq = 1.8$ eV. The same ligand-metal charge transfer parameters $\Delta = 1.0$ eV and $V_{eg} = 2.0$ eV used for the Mn^{2+} simulations were utilized for these Ni^{2+} simulations.

The room temperature Cu $L_{3,2}$ edge spectra are shown in figure 5.7. Features at 933 eV and 953 eV decrease are larger for the low doping concentrations where the

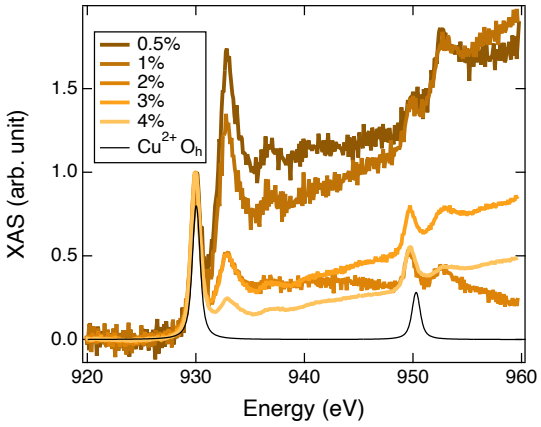

Figure 5.7: Cu $L_{3,2}$ edge XAS spectra of the Cu-doped ϵ-Fe_2O_3 nanoparticles collected at room temperature with simulated spectra.

spectral backgrounds are sloping and the overall signal is very weak, and thus are most likely artifacts. The remaining spectral features are well-described by Cu^{2+} in O_h coordination with $10Dq = 1.6$ eV.

The Zn $L_{3,2}$ edge spectrum for the 6% Zn-doped ϵ-Fe_2O_3 nanoparticles are shown in figure 5.8. Note that the Zn $L_{3,2}$ edge spectra cannot be simulated using Crispy;

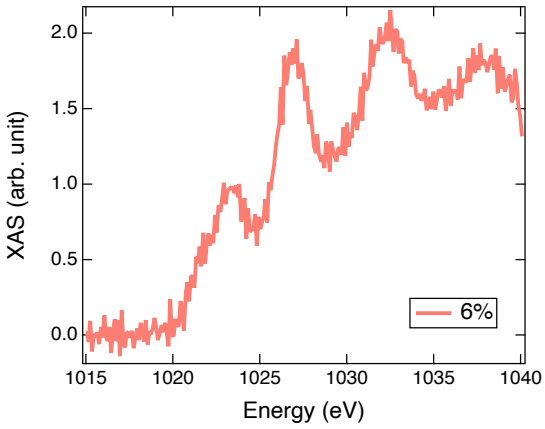

Figure 5.8: Zn $L_{3,2}$ edge XAS spectra of the 6% Zn-doped ϵ-Fe_2O_3 nanoparticles collected at room temperature.

Table 5.5: Summary of dopant ion results for transition metal-doped ϵ-Fe_2O_3 nanoparticles based on XAS $L_{3,2}$ spectra. Ionic radii from reference 122 where LS and HS are low spin and high spin, respectively. The ionic radius of high spin Fe^{3+} O_h is 0.645 Å.

Dopant	Valence	Coordination	$10Dq$ (eV)	Charge transfer	Ionic Radius (Å)
Cr	3+	O_h	2.0	Y	0.615
Mn	3+ (33%)	O_h	2.0	Y	0.58 (LS)/0.645 (HS)
	2+ (67%)	O_h	0.5	Y	0.67 (LS)/0.83 (HS)
Co	3+ (50%)	O_h	1.3	N	0.545 (LS)/0.61 (HS)
	2+ (50%)	O_h	1.3	N	0.65 (LS)/0.745 (HS)
Ni	2+	O_h	1.8	Y	0.69
Cu	2+	O_h	1.6	N	0.73
Zn	2+	O_h	–	–	0.74

however, due to its d^{10} electron configuration, Zn^{2+} is the most stable oxidation state. While other techniques will be necessary to confirm the coordination of the Zn ions, because all of the other dopants occupy O_h sites, the Zn ions most likely do as well. A summary of the XAS results along with the corresponding ionic radii is located in table 5.5.

Once the most probable dopant sites were identified, full Reitveld refinements of the lattice parameters and peak broadening were repeated. No significant differences in these parameters occur for the simulation with the dopant ions incorporated into the crystal structure compared to the initial refinements where all cations were Fe; all result agree within uncertainties. To minimize confusion and for ease of comparison, the subsequent discussion will focus on the initial model containing only Fe ions.

Figure 5.9 shows the a lattice parameter as a function of dopant concentration.

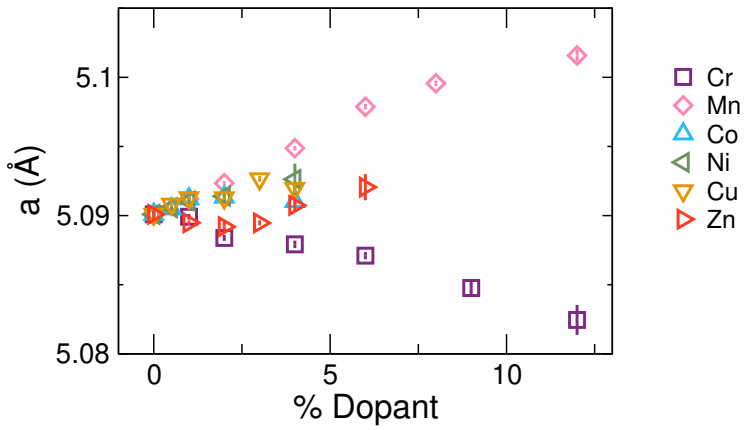

Figure 5.9: Lattice parameter a of transition metal-doped ϵ-Fe_2O_3 nanoparticles as a function of dopant concentration.

This parameter varies with dopant ion, with the most notable impact being the monotonic decrease with Cr concentration and increase with Mn concentration. These behaviours are a consequence of ionic radii of the dopant ions, and the sites they occupy. Because Cr^{3+} O_h has a smaller ionic radius (0.615 Å) than the Fe^{3+} O_h it is displacing in the DO_{h1} site (0.645 Å), the lattice parameter decreases. By extension, the increases in a with Mn-doping implies a larger effective ionic radius of the Mn dopants, compared to Fe^{3+}. Because Mn^{2+} has a relatively small crystal field splitting ($10Dq$=0.5 eV), these ions will be high spin with radius 0.83 Å, while the large crystal field splitting ($10Dq$=2.0 eV) of the Mn^{3+} would tend towards a low spin state. The weighted average of these ions yields a Mn ionic radius of 0.748 Å, consistent with the increased a lattice parameter. Note that these Mn ions will introduce more complexity into the ϵ-Fe_2O_3 system than a simple increase in ionic radius. Mn^{3+} ions are Jahn-Teller active, and have the ability to distort to lift their orbital degeneracy, while charge balancing requires O^{2-} vacancies to form with Mn^{2+} doping. Both of

these factors will impact the overall structure. Like the Mn-doped series, the a lattice parameter of the Ni-doped ϵ-Fe_2O_3 nanoparticles also increases monotonically with concentration albeit with a smaller slope, consistent with its increased ionic radius of 0.69 Å.

More interesting behaviour is measured for the Co-, Cu- and Zn-doped nanoparticles where the a lattice parameter does not change monotonically. For the Co-doped ϵ-Fe_2O_3 the a lattice parameter increases with concentration until 2% Co before decreasing. Such a trend could be the result of the Co ions being initially high spin, with an increased radius, then shifting to a low spin state. Because Co^{2+} ions will also induce O^{2-} vacancies, the interplay between ionic radius, spin state and O^{2-} vacancies compete resulting in the observed non-monotonic behaviour. The situation is somewhat simpler for the Cu- and Zn-doped ϵ-Fe_2O_3 nanoparticles where only high spin states are possible and the ionic radii of both are larger that the original Fe^{3+}. Like Co, the Cu series shows increases in a until 3% Cu, before decreasing. Meanwhile the Zn-doped nanoparticles exhibit the opposite behaviour; decreasing a lattice parameter with increasing concentration until 2% Zn content, before increasing. These series exhibit different responses to the chemical pressure induced by the dopant ions distinct from the ionic size.

Trends in the b lattice parameter (figure 5.10) are less clear. The Mn-doped ϵ-Fe_2O_3 nanoparticles are the only series that exhibits a linear change, with the b lattice parameter decreasing as Mn concentration is increased. The Co series is unique in that b decreases from that of undoped ϵ-Fe_2O_3, but stays constant as the Co concentration increases. Of the other dopant ions (Cr, Ni, Cu and Zn) all show an initial decrease

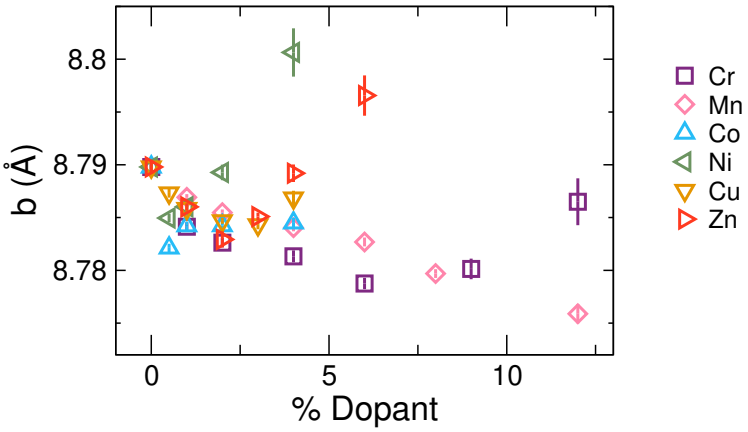

Figure 5.10: Lattice parameter b of transition metal-doped ϵ-Fe_2O_3 nanoparticles as a function of dopant concentration.

in b lattice parameter with increasing doping concentration to a local minima at 1% for the Ni and 2% for the other dopants, followed by an increase. Only the highest doping concentrations of Ni (4%) and Zn (6%) have increased b lattice parameters compared to that of undoped ϵ-Fe_2O_3. Note that the concentration where the b lattice parameter begins to increase for all of these series coincides with the point where the reflection at 35.3° is visibly increased. Such an increase in b could be connected to the ferrite-like distortions.

In contrast to the a and b lattice parameters, the c lattice parameter (shown in figure 5.11) consistently decreases with increased dopant concentration for all dopant ions. Such behaviour reduces the difference between the b and c lattice parameters, so that the unit cell is more tetragonal and less orthorhombic (increasing the overall symmetry of the system). The rate of this decrease does differ between the series, with the dopant ions separating into two groups. Both Mn- and Cu-doped ϵ-Fe_2O_3 decrease more slowly than the other ions (Cr, Co, Ni and Zn). This behaviour does

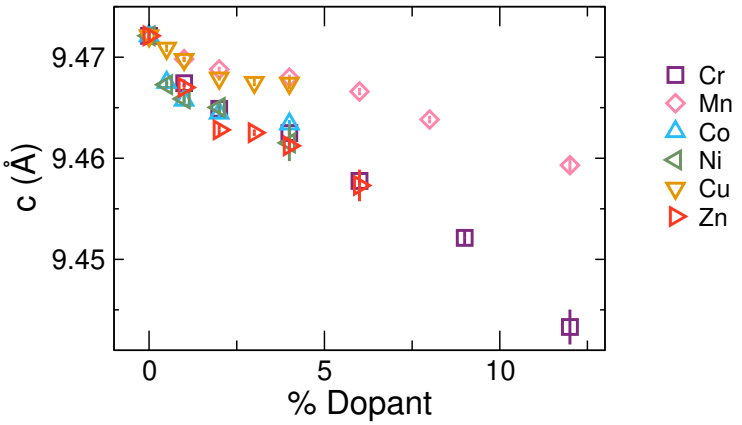

Figure 5.11: Lattice parameter c of transition metal-doped ϵ-Fe_2O_3 nanoparticles as a function of dopant concentration.

not correspond with the ionic radii of the various dopant ions.

Figure 5.12 shows how the unit cell volume behaves as a function of dopant concentration for the different transition metal-doped ϵ-Fe_2O_3 nanoparticles. Unsurprisingly, the volume of the Cr-doped ϵ-Fe_2O_3 unit cell decreases most significantly with increasing dopant concentration –primarily due to the decreases in both the a and c

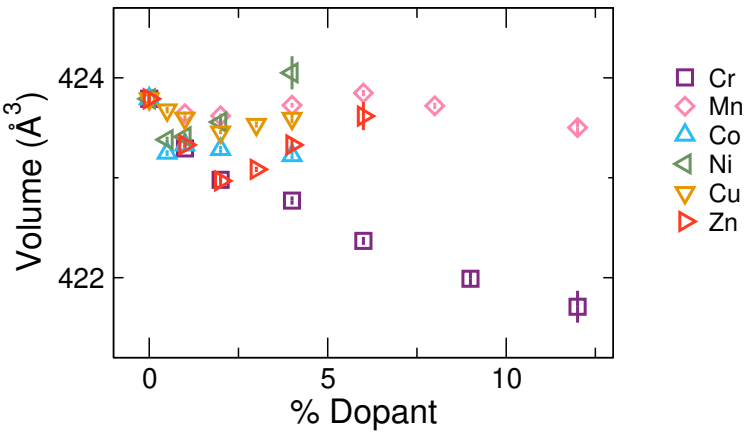

Figure 5.12: Unit cell volume of transition metal-doped ϵ-Fe_2O_3 nanoparticles as a function of dopant concentration.

parameters. Such behaviour is consistent with the Cr^{3+} ions having a smaller ionic radius than any of the other dopant ions and indicates that the Cr-doping causes a negative chemical pressure in the ϵ-Fe_2O_3 nanoparticles. In contrast, the monotonic increase of the a lattice parameter and decreases of the b and c lattice parameters combine such that the overall unit cell volume is relatively unchanged from that of undoped ϵ-Fe_2O_3 for the Mn-doped ϵ-Fe_2O_3. The unit cell volumes of both the Co- and Ni-doped nanoparticles decrease when 0.5% dopant is present. Increased concentrations have no impact on the volume of the Co-doped series, while the volume of the Ni-doped ϵ-Fe_2O_3 increases significantly. The difference in trends between the Co- and Ni-doped nanoparticles are related to the b lattice parameters as the a and c lattice parameters behave similarly. Both the Cu- and Zn-doped ϵ-Fe_2O_3 nanoparticles show a decrease in unit cell volume to a 2% dopant concentration, then an increase with increased concentration. As with the Co- and Ni-doped ϵ-Fe_2O_3 this behaviour follows that of the b lattice parameter, with the differences in magnitude generated by the c lattice parameter.

5.1.2 Doping and Crystallite Size

In addition to the information about the unit cell, Reitveld refinements quantify the average crystallite size of the nanoparticles. As shown in Chapter 4 the crystallite size is directly related to the average nanoparticle size, and affects both the electronic structure and overall magnetic properties of a sample. For this study the undoped ϵ-Fe_2O_3 nanoparticles have an average crystallite size of 24.4±0.1 nm. The majority of the transition metal-doped ϵ-Fe_2O_3 crystallite sizes are within 10% of the undoped.

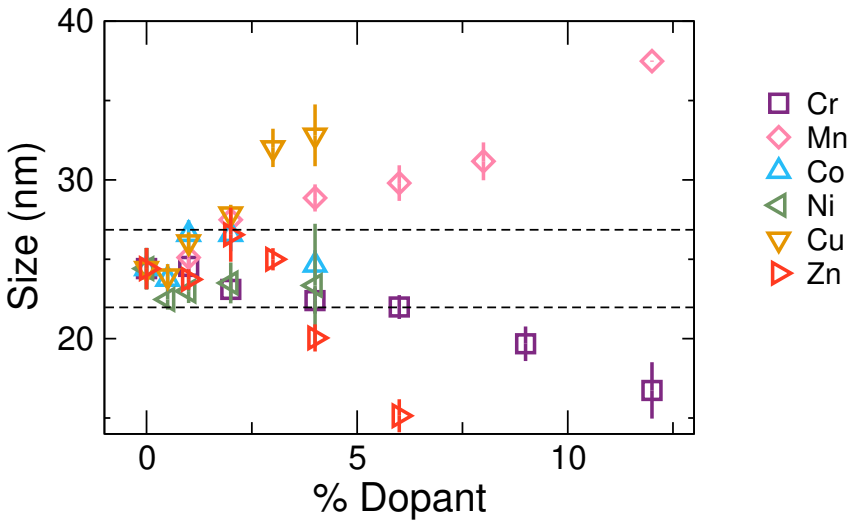

Figure 5.13: Crystallite size of transition metal-doped ϵ-Fe_2O_3 nanoparticles as a function of dopant concentration. Dashed lines indicate sizes within $\pm 10\%$ of undoped ϵ-Fe_2O_3 nanoparticles.

In particular, all of the Co- and Ni-doped samples have crystallite sizes in this range. Meanwhile the Mn- and Cu-doped crystallites increase in size with increased dopant concentration, becoming >10% larger than the undoped crystallites for concentrations $\geq$2%. In contrast, both the Cr- and Zn-doped nanoparticles show a decrease in crystallite size for their highest doping concentrations. Note that all samples were prepared using the same synthesis protocol including identical annealing temperatures in the same furnace. As a result, the variations in crystallite size are a reflection not of the different external parameters but of the nucleation and growth kinetics of the system.

While the mechanisms of nanoparticle nucleation and growth in solution are understood,[123] it is unclear if this theory is applicable to the ϵ-Fe_2O_3 nanoparticle synthesis. Regardless, if the dopant ions change the free energy of either the surface or the bulk crystal, then crystallite nucleation and growth will be affected. If the solu-

tion model is assumed to be applicable to the ϵ-Fe_2O_3 nanoparticles, then an increase in the surface free energy is directly proportional to the critical radius – the minimum size at which a crystallite can survive in solution without being redissolved. An increase in the critical radius will correspond to an increase in the average crystallite size because smaller crystallites can redissolve and contribute to the growth of larger crystallites. Overall, this means that Mn and Cu dopant ions increase the free energy of the surface, while Cr and Zn ions reduce it. Such an effect on the surface energy is intriguing because the low surface energy of ϵ-Fe_2O_3 is believed to cause this phase's size constraints.[10] The increased surface energy of the Mn- and Cu-doped nanoparticles could then allow for the size constraints of undoped ϵ-Fe_2O_3 nanoparticles to be exceeded.

From a practical perspective, the variations in crystallite size with transition metal-doping complicate the overall landscape of this study because nanoparticle size is highly convolved with other parameters, such as the electronic structure and overall magnetic properties. Even the observed trends in the microstructure (i.e. lattice parameters and unit cell volume) can be impacted by strain and finite size effects. Future studies where the annealing temperature has been tuned for each sample to produce identically sized nanoparticles could prove useful.

5.1.3 Electronic Changes with Doping

Mössbauer spectra were collected on all of the transition metal-doped ϵ-Fe_2O_3 nanoparticles at 10 K, 150 K and 300 K to characterize the local electronic environment around the Fe ions. The 10 K spectra are shown in figure 5.14. Consistent with the XRD

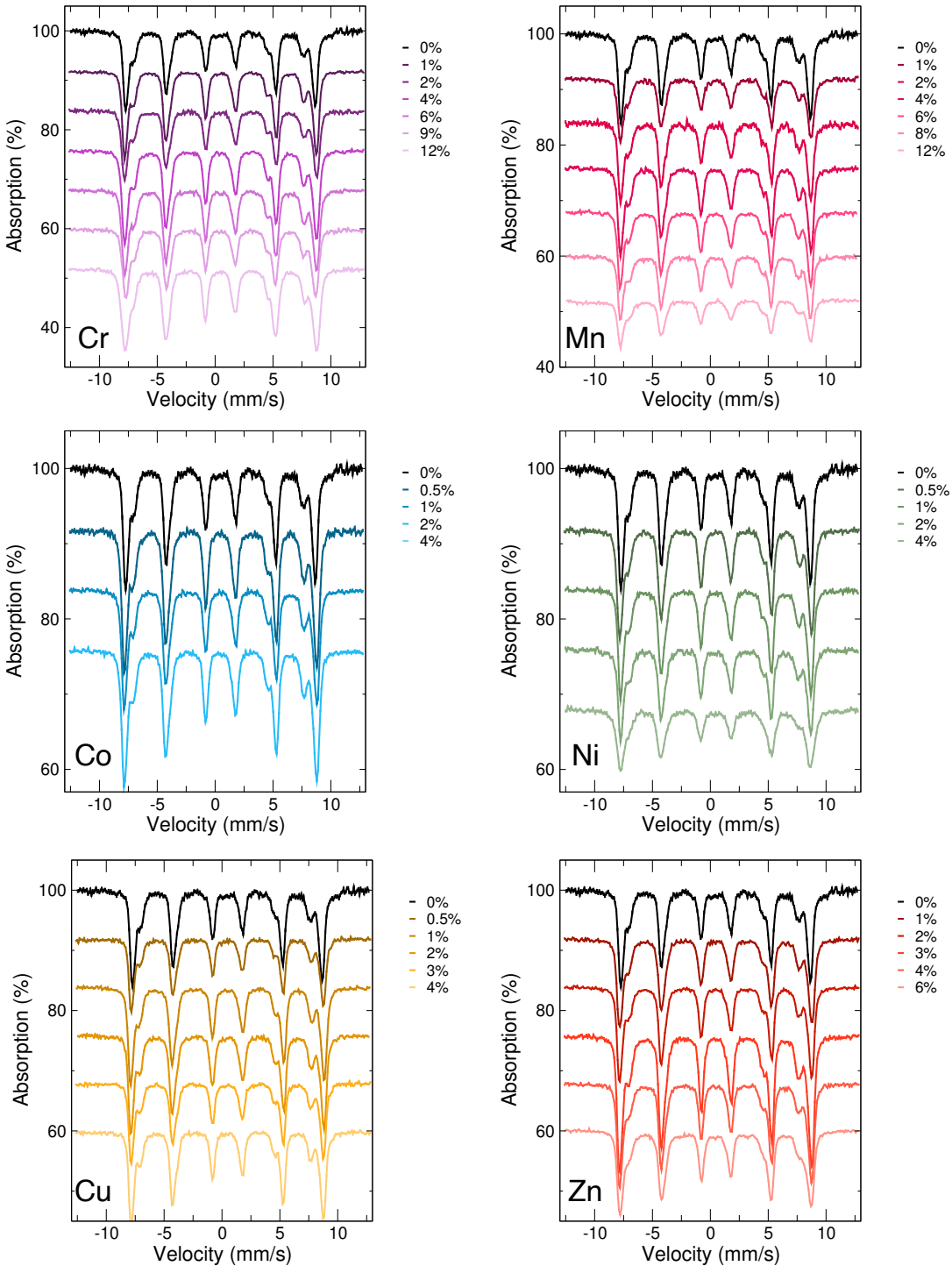

Figure 5.14: 10 K Mössbauer spectra of transition metal-doped ϵ-Fe_2O_3 nanoparticles.

results, spectra corresponding to low levels of doping are similar to that of the undoped ϵ-Fe_2O_3, while differences, particularly broadening of the spectral lines, are more evident for higher doping concentrations. All spectra were well-fit using three components corresponding to the DO_h, RO_h, and T_d sites of single-phase ϵ-Fe_2O_3. The Mössbauer spectra reveal no indication of a spinel-like secondary phase.

Figure 5.15 shows the hyperfine parameters as a function of dopant concentration for the Cr-doped ϵ-Fe_2O_3 nanoparticles. The isomer shifts (δ) of both O_h components show relatively small variations with Cr concentration, while δ_{Td} increases. Such an increase indicates that d electrons shift towards the Fe T_d nucleus as Cr is added

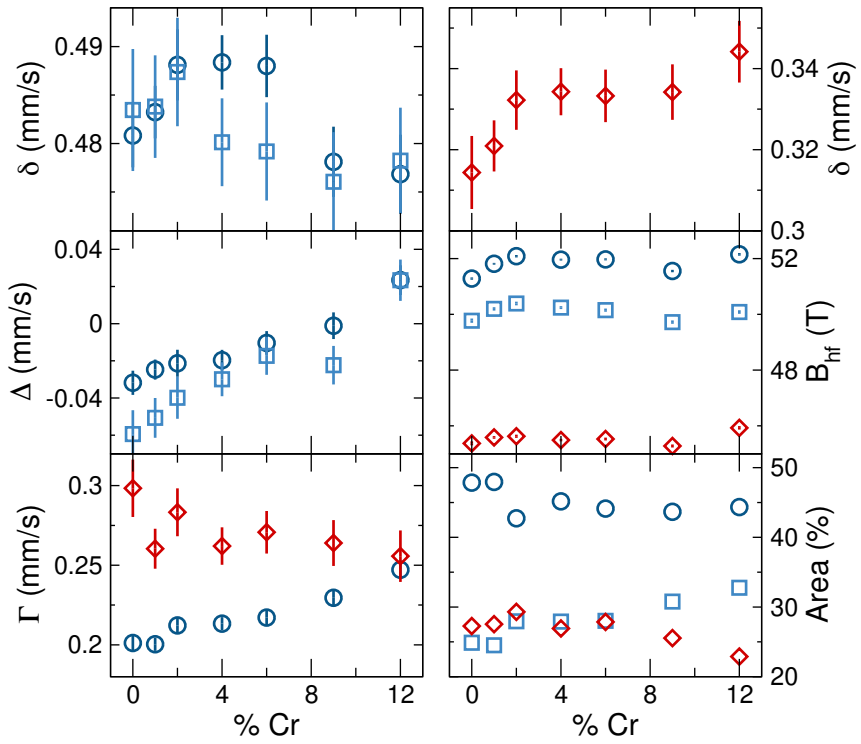

Figure 5.15: 10 K hyperfine parameters of Cr-doped ϵ-Fe_2O_3 nanoparticles. Dark blue circles are DO_h component, light blue squares are RO_h and red diamonds are T_d. Line width (Γ) of both O_h sites are identical, and so only $\Gamma_{DOh}(T)$ is presented.

to the structure; however, this increase is not linear. Instead, δ_{Td} plateaus when the Cr concentration is between 2% and 9%. The quadrupole splittings (Δ) of both octahedral components (DO_h and RO_h) increase linearly with Cr doping. This trend translates to the electric field gradient around the O_h sites becoming more isotropic as the T_d electrons are more localized. Such behaviour indicates that the delocalized T_d electrons contribute to the anisotropy of the O_h electric field gradient. Additionally, the line widths (Γ) of the O_h sites increase while Γ_{Td} decreases with increased Cr concentration, meaning that the O_h sites become more disordered with increased Cr, while the T_d sites become less.

Interestingly, the concentration dependent behaviour of the magnetic hyperfine field (B_{hf}) of all sites follows that of δ_{Td}, suggesting that the changes to the nuclear electronic density at the T_d sites are coupled to variations in the Fermi-contact term or valence orbital motion.[70] The reduction in the relative site area of the DO_h component supports the previous conclusions that the Cr ions enter the DO_{h1} site. Overall, the changes observed in the hyperfine parameters of the Cr-doped ϵ-Fe_2O_3 nanoparticles indicate that Cr doping pushes electrons toward the T_d sites, resulting in altered local environment around the O_h sites. This new configuration changes the hybridization and thus the exchange interactions between the different Fe sites.

The hyperfine parameters at 10 K for the Mn-doped ϵ-Fe_2O_3 are shown in figure 5.16. δ_{Oh} fluctuates for low concentrations of Mn ($\leq$4%), with both parameters decreased when the Mn concentration $\geq$6%. δ_{Td} shows a similar trend with increases for low Mn concentrations and a decrease back to the δ_{Td} of the undoped ϵ-Fe_2O_3 nanoparticles for Mn concentrations $\geq$6%. Overall, for low concentrations of Mn,

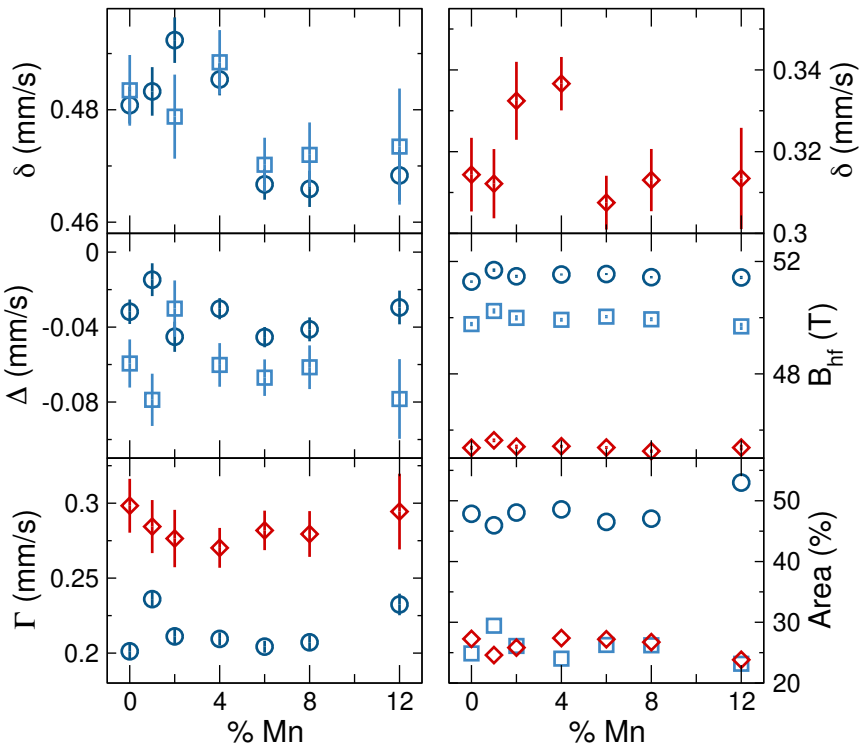

Figure 5.16: 10 K hyperfine parameters of Mn-doped ϵ-Fe_2O_3 nanoparticles. Dark blue circles are DO_h component, light blue squares are RO_h and red diamonds are T_d. Both Γ_{Oh} are identical, and so only $\Gamma_{DOh}(T)$ is presented.

the nuclear electronic density around the O_h sites is fairly constant, while electrons are pushed slightly towards the T_d sites. Then when the Mn concentration is $\geq$6% the electrons shift away from all of the Fe sites, returning the T_d to the undoped electronic density and resulting in modified O_h sites. With no significant variations in Δ_{Oh}, these shifts in electrons must occur symmetrically. No clear trends in either Γ or the relative site areas as a function of Mn concentration are evident, with only the increased Γ for 12% Mn concentration indicating increased local disorder.

The hyperfine parameters at 10 K for the Co- and Ni-doped ϵ-Fe_2O_3 are shown in figure 5.17. Slight differences are evident in the concentration dependence of δ_{Oh}.

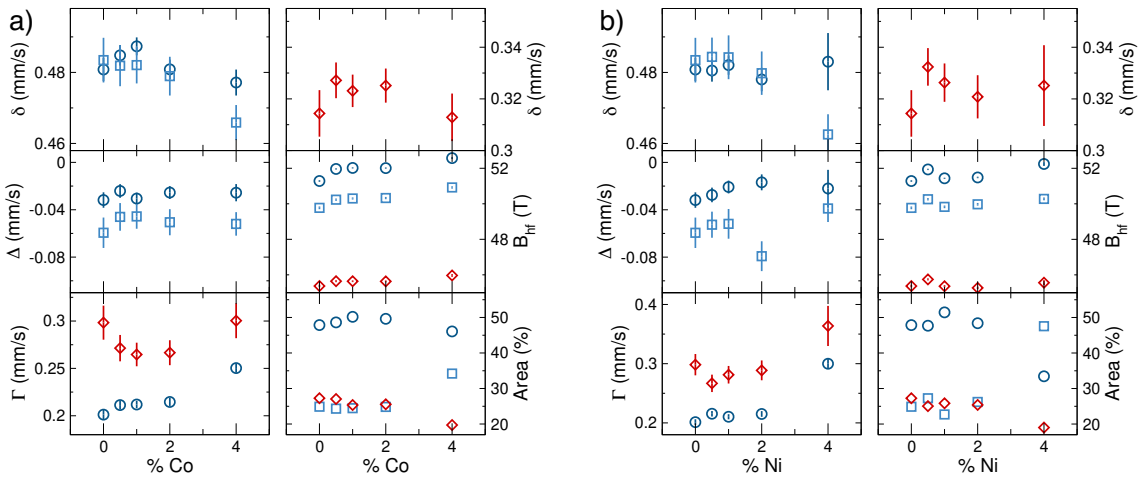

Figure 5.17: 10 K hyperfine parameters of a) Co- and b) Ni-doped ϵ-Fe_2O_3 nanoparticles. Dark blue circles are DO_h component, light blue squares are RO_h and red diamonds are T_d. Both Γ_{Oh} are identical, and so only $\Gamma_{DOh}(T)$ is presented.

The Co-doped series shows increased δ_{ROh} with dopant concentration to 1% Co before decreasing, while δ_{ROh} is constant for all of the Ni-doped ϵ-Fe_2O_3. δ_{DOh} is independent of dopant concentration other than the highest concentration (4%), where it decreases significantly. Such a change in δ_{DOh} means that the DO_h and RO_h sites have distinct nuclear electronic densities due to electrons pulling away from the RO_h sites. This separation of δ_{Oh} occurs with an increase in Γ of all the sites, reflecting increased local disorder in the system. Additionally, the relative site areas become significantly different from that expected for ϵ-Fe_2O_3. This behaviour is unique to the 4% Co- and Ni-doped nanoparticles and does not appear in any of the other dopant series. Finally, B_{hf} of all components increase with doping, except for the T_d site of the Ni-doped nanoparticles.

Figure 5.18 shows the hyperfine parameters for the Cu- and Zn-doped ϵ-Fe_2O_3 at 10 K. The Cu-doped spectra do not show any significant changes in δ or Δ, indicating

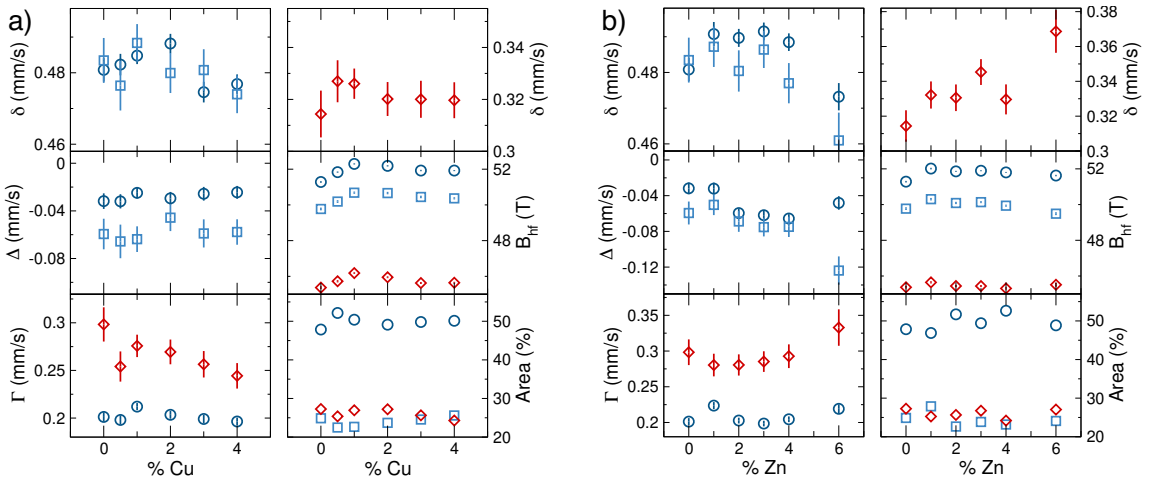

Figure 5.18: 10 K hyperfine parameters of a) Cu- and b) Zn-doped ϵ-Fe_2O_3 nanoparticles. Dark blue circles are DO_h component, light blue squares are RO_h and red diamonds are T_d. Both Γ_{Oh} are identical, and so only $\Gamma_{DOh}(T)$ is presented.

that the local electronic environment around the Fe sites are minimally impacted by Cu doping. Changes are evident in the increased B_{hf} of all sites, reflecting an increased magnetic hyperfine field. Unlike the other transition metal-doped samples, Γ does not increase with increased dopant concentration, and Γ_{Td} actually decreases. Such a decrease indicates the T_d site becomes more ordered as Cu is incorporated into the ϵ-Fe_2O_3 structure. δ of the Zn-doped samples show a decrease in δ_{Oh} and increase in δ_{Td} with doping; electrons are pulled away from the O_h sites −particularly the RO_h, and pushed toward the T_d. The decrease in Δ_{ROh} reveals that these changes increase the asymmetry of the electric field gradient. B_{hf} of all sites increase slightly, as does Γ as the system exhibits increased disorder.

Overall each dopant ion impacts the hyperfine parameters slightly differently. Because the magnetism of these transition metal-doped ϵ-Fe_2O_3 systems is of significant interest, further examination of the behaviour of B_{hf} is warranted. This parameter

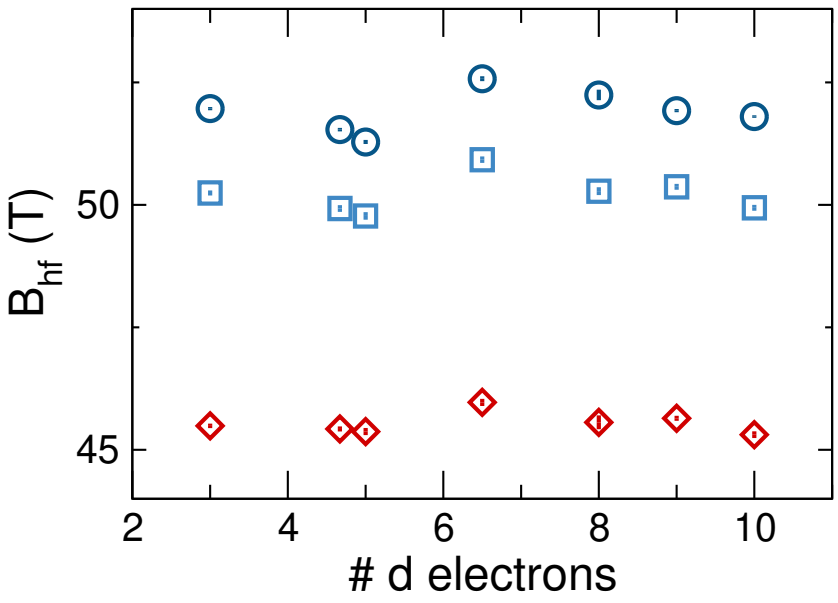

Figure 5.19: B_{hf} of the 4% transition metal-doped ϵ-Fe_2O_3 nanoparticles at 10 K as a function of the dopant ion's number of d electrons. Dark blue circles are DO_h component, light blue squares are RO_h and red diamonds are T_d. Note that B_{hf} for d^5 corresponds to the undoped ϵ-Fe_2O_3.

describes the local magnetic hyperfine field originating from the difference between spin-up and spin-down densities at the nuclei and contains contributions from both core and valence orbitals.[124] From the effects on δ of the transition metal-doped ϵ-Fe_2O_3, the dopant ions serve to push and pull the electronic nuclear density without changing the number of d electrons of the Fe itself. One source of such shifts in electronic density is the different number of d electrons in the doped sites. Figure 5.19 shows how the B_{hf} of 4% transition metal-doped ϵ-Fe_2O_3 nanoparticles at 10 K change with the number of dopant ion d electrons. While both the DO_h and RO_h B_{hf} are increased for all dopant ions, $B_{hf,Td}$ shows minimal changes. Such behaviour indicates that the shorter Fe^{3+} T_d–O^{2-} bonds and their hybridization are less sensitive to the perturbations introduced by the dopant ions than the longer Fe^{3+}

O_h−O^{2-} ones.[125] The exception to this is the increased $B_{hf,Td}$ with Co-doping, which is somewhat expected because Co doping is known to impact spin-orbit coupling.

Overall, the $B_{hf,Oh}$ as a function of d electrons can be divided into two regimes. The first consists of dopant ions with fewer d electrons than Fe (d <5), where the Cr^{3+} ions with d^3 have the largest $B_{hf,Oh}$, followed by the $Mn^{2+/3+}$ ions with d^5/d^4. Note that XAS simulations indicate that the Mn^{2+} is high spin, having the same electronic configuration as the Fe^3+, while the low spin Mn^{3+} will have the empty e_g orbitals like the Cr^{3+} albeit with one of the t_{2g} orbitals now doubly occupied. Since the relative increase in B_{hf} of the Mn-doped nanoparticles is ∼33% of that of the Cr-doped nanoparticles, and the Mn^{3+} accounts for ∼33% of the Mn ions, it seems like the impact of the Cr^{3+} and Mn^{3+} ions on B_{hf} are very similar −likely due to their empty e_g orbitals.

The second regime is of dopant ions with d >5, where again B_{hf} decreases as d increases. The Co-doped ϵ-Fe_2O_3 nanoparticles have the largest B_{hf} of all the nanoparticles, at least partially due to interactions with the spin-orbit coupling. The $Co^{2+/3+}$ ions have d^7/d^6; however, the $10Dq$ of the XAS simulations do not unambiguously identify the spin state. It is possible that the Co^{3+} (d^6) ions are low spin (with empty e_g orbitals), and so increase B_{hf} via the same mechanism as the Cr^{3+} and Mn^{3+}. For the remaining ions, only a high spin configurations (with filled e_g orbitals) are possible. The reduction in B_{hf} with increasing d is thus a reduction in the difference between spin-up and spin-down densities as the number of unpaired electrons decreases.

5.1.4 Overall Magnetism with Doping

Hysteresis loops were acquired at a variety of temperatures to measure the field-dependent response of the transition metal-doped ϵ-Fe_2O_3 nanoparticles. Figures 5.20 and 5.21 show the 10 K, 150 K and 300 K hysteresis loops. Overall, all of the different transition metal-doped series show the expected evolution in loop shape with temperature. Notably the 150 K loops show a larger coercive field ($\mu_0 H_C$) than that of the 10 K loops with a similar magnetic saturation (M_S), while the 300 K loops show further increases in $\mu_0 H_C$ and decreased M_S. Nanoparticles with the highest doping concentrations for all dopant ions have wasp-waisted loops. Note that while these systems have very small values of $\mu_0 H_C$, the overall loop shape does reveal high anisotropy for a fraction of the spin population. None of the doped ϵ-Fe_2O_3 nanoparticles reveal behaviour consistent with superparamagnetism.

The impact of the loop shape is quantified in the temperature dependent coercive field (shown in figure 5.22a), where the 9% Cr and 12% Cr samples have significantly smaller $\mu_0 H_C$ compared to the other samples. $\mu_0 H_C$ of the Cr-doped ϵ-Fe_2O_3 is decreased from that of the undoped ϵ-Fe_2O_3 in both the incommensurate phase (<100 K) and ferrimagnetic phase (>200 K), and increased for Cr<9% through the phase transition. Such an increase in $\mu_0 H_C$ at intermediate temperatures is consistent with the transition temperature decreasing as a function of Cr-doping, similar to the change that was observed in Section 4.4 where the largest particles exhibited an increased transition temperature due to enhanced hybridization in the incommensurate phase. With decreases to nanoparticle size as a function of Cr concentration (see figure 5.13), reduced long-range interactions will play a similar role to that observed

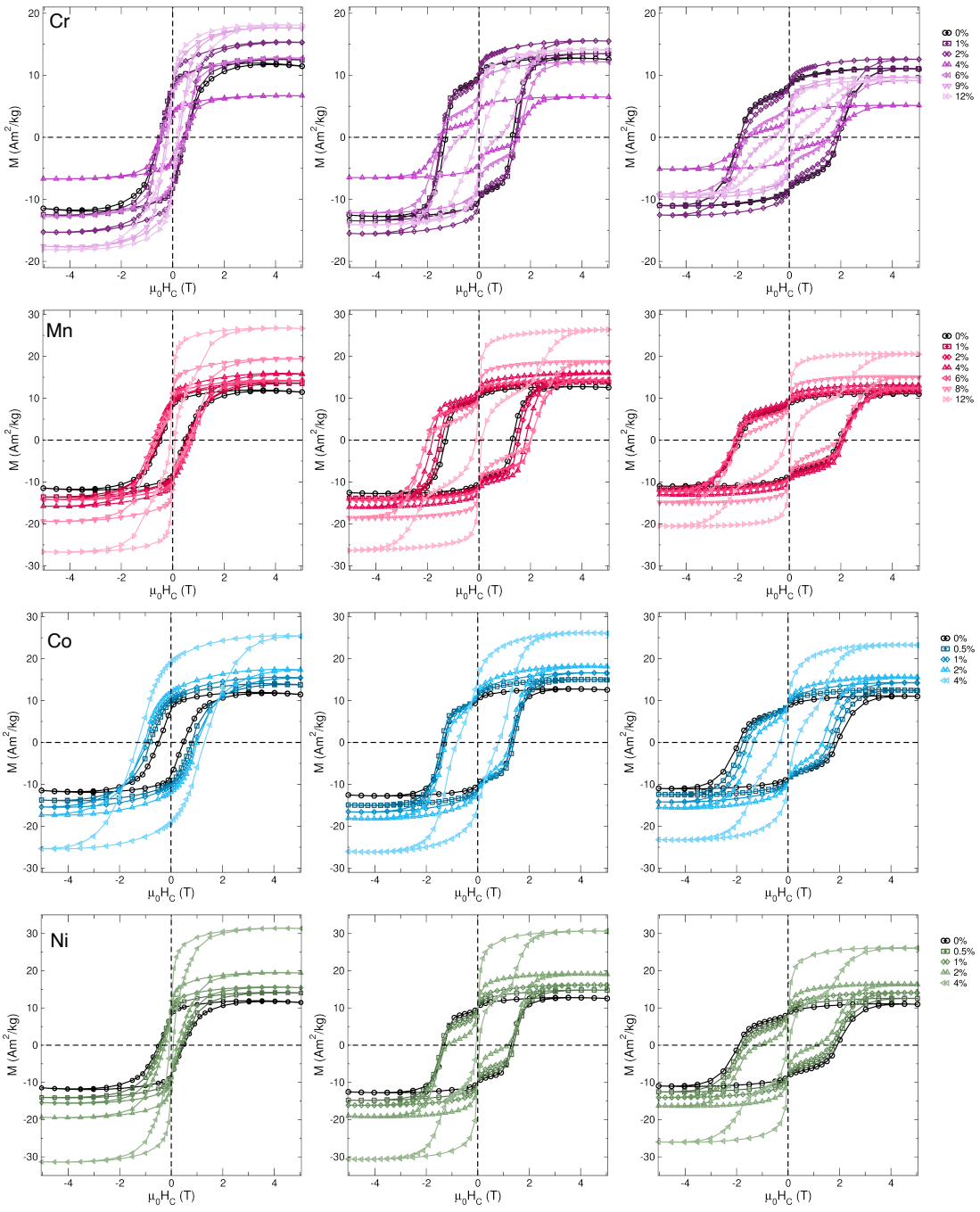

Figure 5.20: Hysteresis loops at 10 K (left), 150 K (centre) and 300 K (right) of Cr-, Mn-, Co-, and Ni-doped ϵ-Fe_2O_3 nanoparticles.

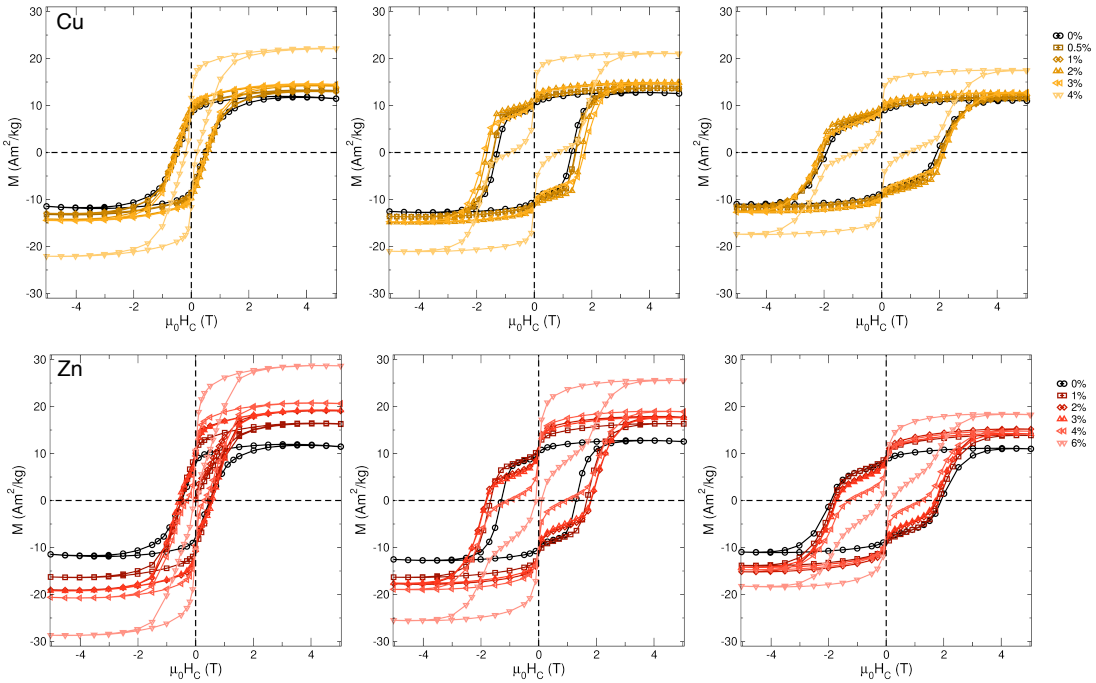

Figure 5.21: Hysteresis loops at 10 K (left), 150 K (centre) and 300 K (right) of Cu-, and Zn-doped ϵ-Fe_2O_3 nanoparticles.

for the different sizes of ϵ-Fe_2O_3 nanoparticles in Chapter 4. Additionally, changes to the local electronic structure – particularly the localization of T_d electrons and disruption of the DO_{h1} chains, alter the short-range interactions. Combined, these effects reduce the spin-orbit coupling in the system, lowering the magnetic transition temperature and decreasing $\mu_0 H_C$ of both phases.

The behaviour of the magnetic saturation ($M_S(T)$) shown in figure 5.22b is not so straightforward to explain. $M_S(T)$ is practically identical for the undoped and 1% Cr-doped ϵ-Fe_2O_3 nanoparticles, while 2% Cr-doping increases $M_S(T)$ by ~20% in the incommensurate phase and ~15% in the ferrimagnetic phase. Such a change in $M_S(T)$ is significant considering the low dopant concentration. The magnetic structure of ϵ-Fe_2O_3 is composed of the DO_{h1}, DO_{h2}, RO_h and T_d sites with magnetic

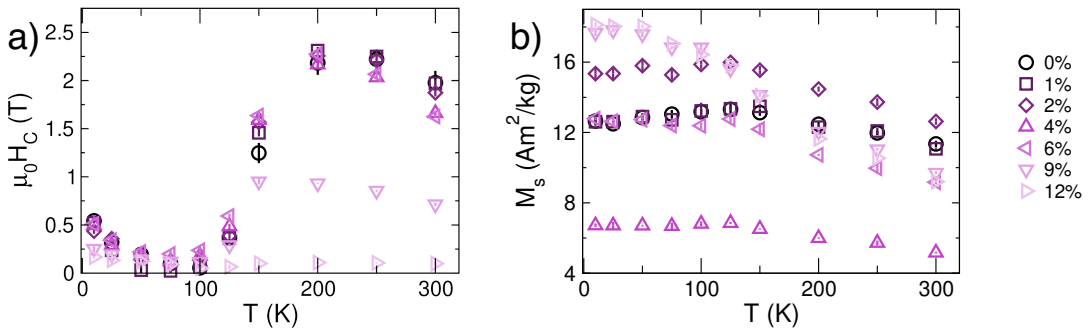

Figure 5.22: a) $\mu_0 H_C(T)$ and b) $M_S(T)$ of Cr-doped ϵ-Fe_2O_3 nanoparticles.

moments -3.9 μ_B, +3.9 μ_B, +3.7 μ_B, and -2.4 μ_B,[41] respectively, resulting in a net moment of 0.325 μ_B per Fe^{3+}. If all of the Cr^{3+} ions that substitute into the DO_{h1} site have moment -3.85 μ_B,[126] and all else remains constant, then the net moment would only increase to 0.3255 μ_B per cation (0.15% increase) – orders of magnitude smaller than the 20% measured experimentally. Higher concentrations of doping serve to illustrate the complexity of the system, with $M_S(T)$ decreasing by ~50% for the 4% Cr-doped ϵ-Fe_2O_3, before increasing closer to the undoped ϵ-Fe_2O_3 values for the 6% Cr nanoparticles. Meanwhile both the 9% Cr and 12% Cr samples show increased $M_S(T)$ in the incommensurate phase, and decreased $M_S(T)$ in the ferrimagnetic phase compared to undoped ϵ-Fe_2O_3. Such variations as a function of dopant ion clearly show that the incorporation of Cr ions into the ϵ-Fe_2O_3 structure significantly alters the exchange interactions that determine the overall magnetization

Compared to the Cr-doped ϵ-Fe_2O_3, the hysteresis loops Mn-doped ϵ-Fe_2O_3 nanoparticles reveal a much simpler picture. Figure 5.23 shows $\mu_0 H_C(T)$ and $M_S(T)$. With the exception of the 12% Mn sample (which becomes wasp-waisted), both $\mu_0 H_C$ and M_S increase with increased Mn concentration for all of the samples across the entire temperature range; however, the mechanism behind this increase are unclear.

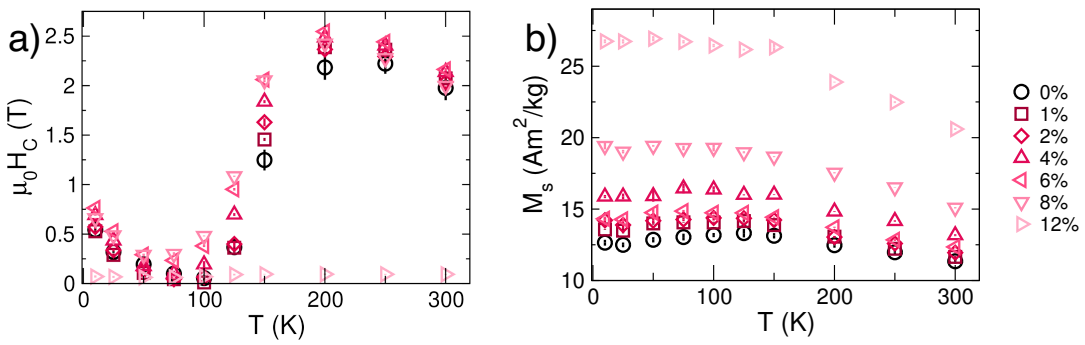

Figure 5.23: a) $\mu_0 H_C(T)$ and b) $M_S(T)$ of Mn-doped ϵ-Fe_2O_3 nanoparticles.

Mössbauer hyperfine parameters do not show obvious trends indicating direct modifications to the Fe local electronic environment due to Mn-doping. Meanwhile XRD reveals a direct relationship between crystallite size and Mn-dopant concentration. Because crystallite size has been shown to increase $\mu_0 H_C$ (see Chapter 4), the observed behaviour is not due to the Mn ions directly modifying the spin-orbit coupling, but an indirect response from changes in particle size. As with the Cr-doped ϵ-Fe_2O_3 nanoparticles, the observed increases in $M_S(T)$ are larger than would be expected, and so the Mn ions must perturb the existing Fe-Fe exchange interactions. With strong evidence that the Cr and Mn ions dope into different structural sites, different

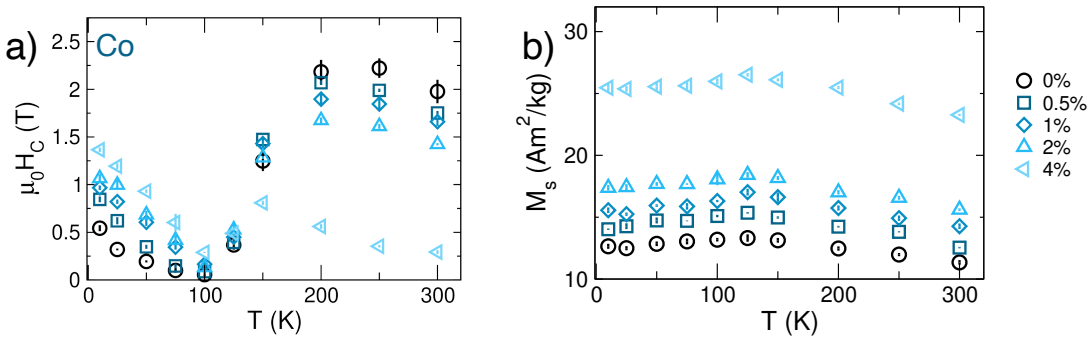

Figure 5.24: a) $\mu_0 H_C(T)$ and b) $M_S(T)$ of Co-doped ϵ-Fe_2O_3 nanoparticles.

magnetic trends are not unexpected.

Of all the transition metal-dopants, Co is the one which most significantly affects $\mu_0 H_C$. Increased Co concentrations increase $\mu_0 H_C$ in the low temperature incommensurate phase, and decrease $\mu_0 H_C$ in the ferrimagnetic phase. These changes speak directly to the impact of the Co dopant ions on the spin-orbit coupling of the ϵ-Fe_2O_3 phase, consistent with the increased B_{hf} from Mössbauer spectroscopy. A similar effect on $\mu_0 H_C$ is observed for Co-doped γ-Fe_2O_3.[127] Like the Mn-doped ϵ-Fe_2O_3, increases in M_S are monotonic with respect to Co ion concentration; however, the magnitude is significantly larger. While 4% Mn doping increases M_S by ~20% of the undoped values, 4% Co substitution increases M_S by 100%. Such an increase cannot be attributed directly to the dopant ions and must rely on perturbation of the existing exchange interactions. Note that neither XRD nor Mössbauer spectroscopy analysis were able to identify a single site for the Co occupation. Based on the change to the magnetic saturation, it seems that the Co ions occupy a different site than either the DO_{h1} of the Cr or the DO_{h2} of the Mn. Because the XAS spectra show the Co ions are in O_h coordination, they must occupy the RO_h site.

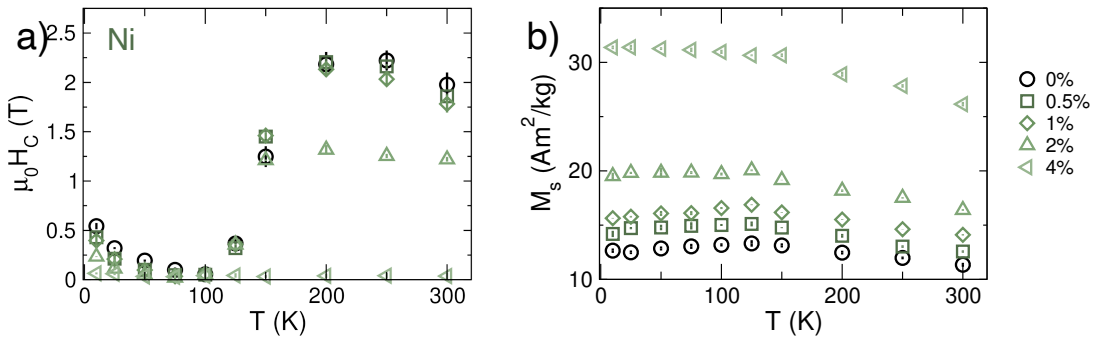

Figure 5.25: a) $\mu_0 H_C(T)$ and b) $M_S(T)$ of Ni-doped ϵ-Fe_2O_3 nanoparticles.

The effects of Ni-doping on $\mu_0 H_C$ are similar to those observed for the Cr-doped ϵ-Fe_2O_3 where small increases are observed at ∼150 K, but otherwise $\mu_0 H_C$ is decreases with increased doping. Because the crystallite size of the Ni-doped ϵ-Fe_2O_3 nanoparticles does not change significantly, these changes can be directly attributed to the effects of Ni-doping and not extrinsic size effects. The reduction of $\mu_0 H_C$ in both the high and low temperature phases indicate a reduction to the spin-orbit coupling, while the increased in $\mu_0 H_C$ through the magnetic transition is consistent with a reduction in the transition temperature. Such behaviour indicates that the Ni-dopants disrupt hybridization and lower the energy barrier to the ferrimagnetic state. Interestingly, $\mu_0 H_C$ begins to collapse at much lower concentrations of Ni-doping than the other dopant ions, with the 2% Ni-doped ϵ-Fe_2O_3 nanoparticles having a significantly reduced $\mu_0 H_C$ of 1.5 T compared to the ∼2 T of the nanoparticles with lower Ni concentrations

M_S of this series of nanoparticles increases monotonically with Ni concentration. These increases are larger than those observed for Cr- and Mn-doping, though closest to the Co-doped ϵ-Fe_2O_3, with 4% Ni-doped exhibiting M_S ∼140% larger than that of undoped ϵ-Fe_2O_3. The similarities between the Co- and Ni-doped nanoparticles' M_S is consistent with these dopant ions occupying the same site (RO_h). With similar sized crystallites, the differences between these series are the result of the different dopant species.

Like the Mn-doped ϵ-Fe_2O_3 nanoparticles, the Cu-doped samples have increased $\mu_0 H_C$ in the high temperature ferrimagnetic phase; however, $\mu_0 H_C$ in the incommensurate phase is unchanged. With larger crystallites with increased Cu-doping (see

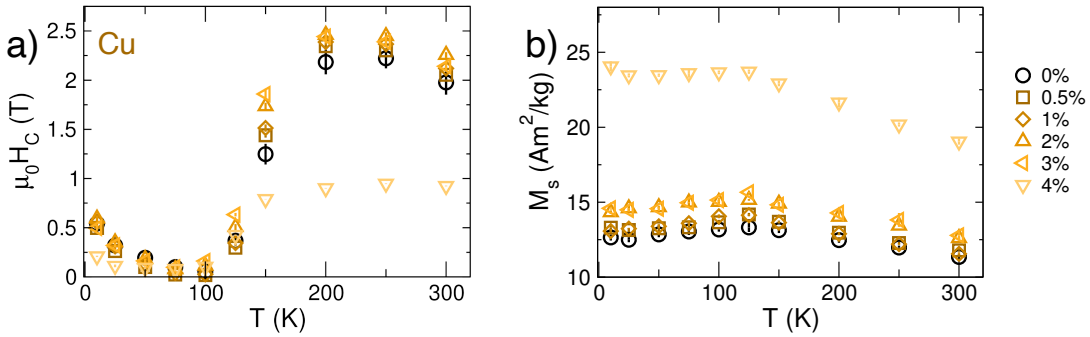

Figure 5.26: a) $\mu_0 H_C(T)$ and b) $M_S(T)$ of Cu-doped ϵ-Fe_2O_3 nanoparticles.

figure 5.13), the increase in high temperature $\mu_0 H_C$ is likely a consequence of size effects. Such an increase would also be expected to appear in the incommensurate phase, so the constant $\mu_0 H_C$ indicates a reduction of the spin-orbit coupling. M_S of the Cu-doped ϵ-Fe_2O_3 nanoparticles shows relatively small increases with doping for concentrations up to 3% Cu-doping. These increases are in line with those observed for the Mn-doped nanoparticles, suggesting Cu ions occupy the DO_{h2} sites. The nanoparticles containing 4% Cu show a significant increase in M_S such that these values are more consistent with the Co- and Ni-doped ϵ-Fe_2O_3. Such behaviour is consistent with the Cu ions beginning to occupy the RO_h sites as well.

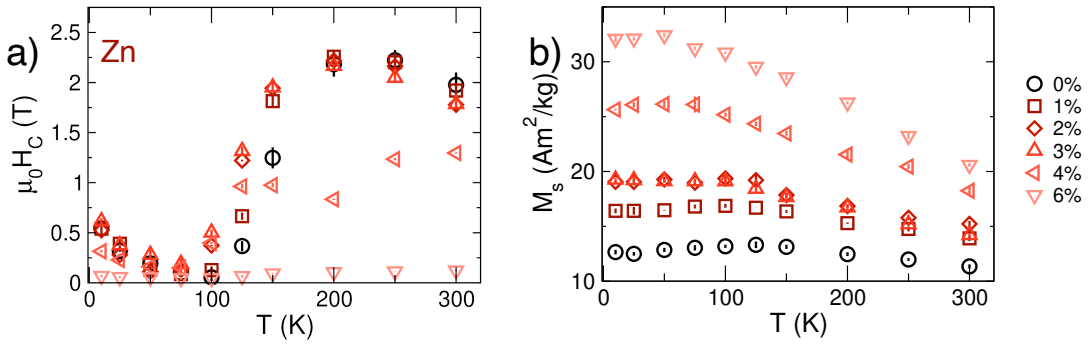

Figure 5.27: a) $\mu_0 H_C(T)$ and b) $M_S(T)$ of Zn-doped ϵ-Fe_2O_3 nanoparticles.

The Zn-doped ϵ-Fe_2O_3 show minimal changes to $\mu_0 H_C$ in both the incommensurate and ferrimagnetic phases for Zn concentrations <4% (where the loops become wasp-waisted). Differences in $\mu_0 H_C(T)$ through the intermediate temperatures indicate that the Zn-doping reduces the transition temperature slightly. Overall, the incorporation of Zn ions does not change the spin-orbit coupling in either the high or low temperature phases. As with all the transition metal dopants except Cr, M_S tends to increase with increased dopant concentration, with the exceptions of the 2% Zn and 3% Zn-doped ϵ-Fe_2O_3 nanoparticles which have practically identical M_S. Such a change in behaviour is consistent with the Zn ions beginning to occupy a second site, which causes different perturbations of the exchange interactions. Overall, the increases to M_S correspond closely to the behaviour of the Co- and Ni-doped ϵ-Fe_2O_3, indicating the Zn ions primarily occupy the RO_h sites.

To enable comparison between the different dopant ions, figure 5.28 shows how $\mu_0 H_C$ at 10 K and 300 K change as a function of the number of d electrons in the dopant ion. Like figure 5.19 which shows B_{hf} as a function of the number d electrons

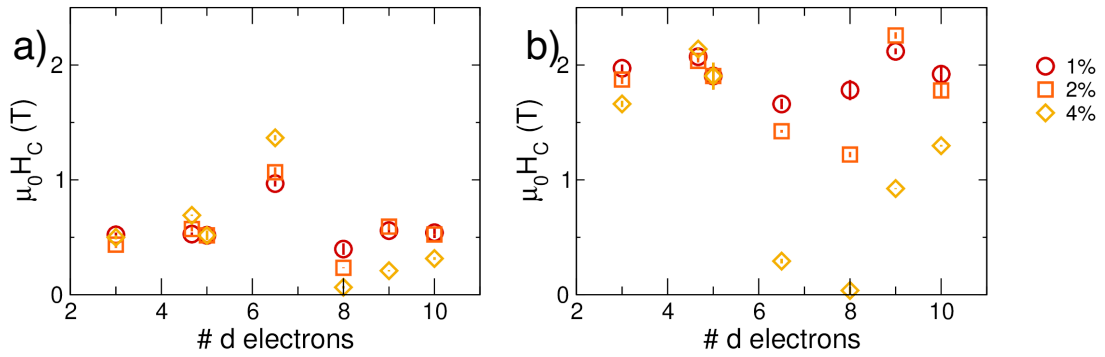

Figure 5.28: $\mu_0 H_C$ of transition metal-doped ϵ-Fe_2O_3 nanoparticles as a function of d electrons in dopant ion at a) 10 K and b) 300 K.

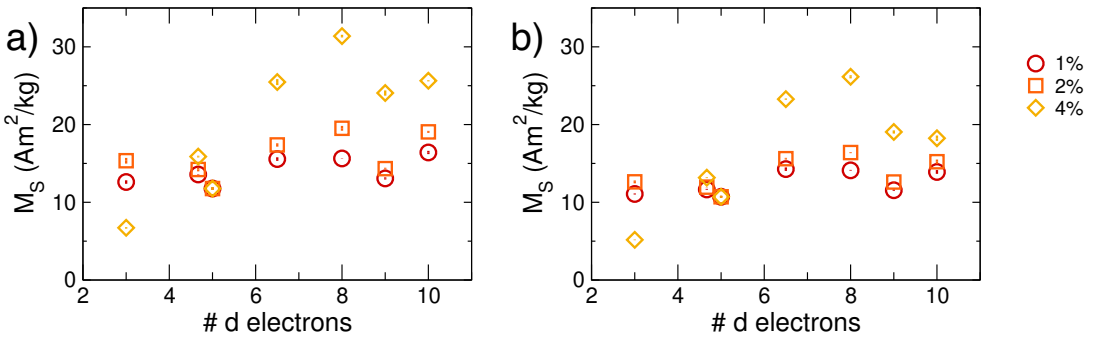

Figure 5.29: $M_S(T)$ of transition metal-doped ϵ-Fe_2O_3 nanoparticles as a function of d electrons in dopant ion at a) 10 K and b) 300 K.

of dopant ion, the Cr- and Mn-doped samples show similar behaviour, with $\mu_0 H_C$ values relatively unchanged from those of the undoped ϵ-Fe_2O_3. While the Co-doped samples exhibit unique behaviour, all of the $\mu_0 H_C$ show large changes with respect to dopant concentration when $d > 5$ (Co, Ni, Cu and Zn). Such results are a consequence of the hysteresis loops becoming wasp-waisted at lower dopant concentrations than when $d < 5$, corresponding to the appearance of ferrite-like distortions in XRD. The breakdown of ϵ-Fe_2O_3 for these dopants is also apparent in M_S as a function of d electrons (shown in figure 5.29), where these systems exhibit larger changes to M_S with doping. Overall, this trend confirms that the ϵ-Fe_2O_3 structure and magnetism breaks down with the addition of relatively low concentrations of high d transition metal ions into the RO_h site. The most intriguing behaviour remains that of the Cr-doped ϵ-Fe_2O_3. While the other dopant ions tend to affect the magnetic properties in a similar manner, Cr-doping causes non-monotonic variations in M_S and is notably the only ion to cause a decrease.

5.2 Cr-doped ϵ-Fe_2O_3

Because the Cr-doped ϵ-Fe_2O_3 nanoparticles show unusual magnetic behaviour, they are the focus for further investigation. XAS spectra acquired over the Fe $L_{3,2}$, Cr $L_{3,2}$ and O K edges at 50 K are shown in figure 5.30. The Cr $L_{3,2}$ spectra in figure 5.30c are the same ones shown in figure 5.3, with the simulated spectrum in figure 5.30d as described previously revealing Cr^{3+} in O_h coordination. No significant changes are

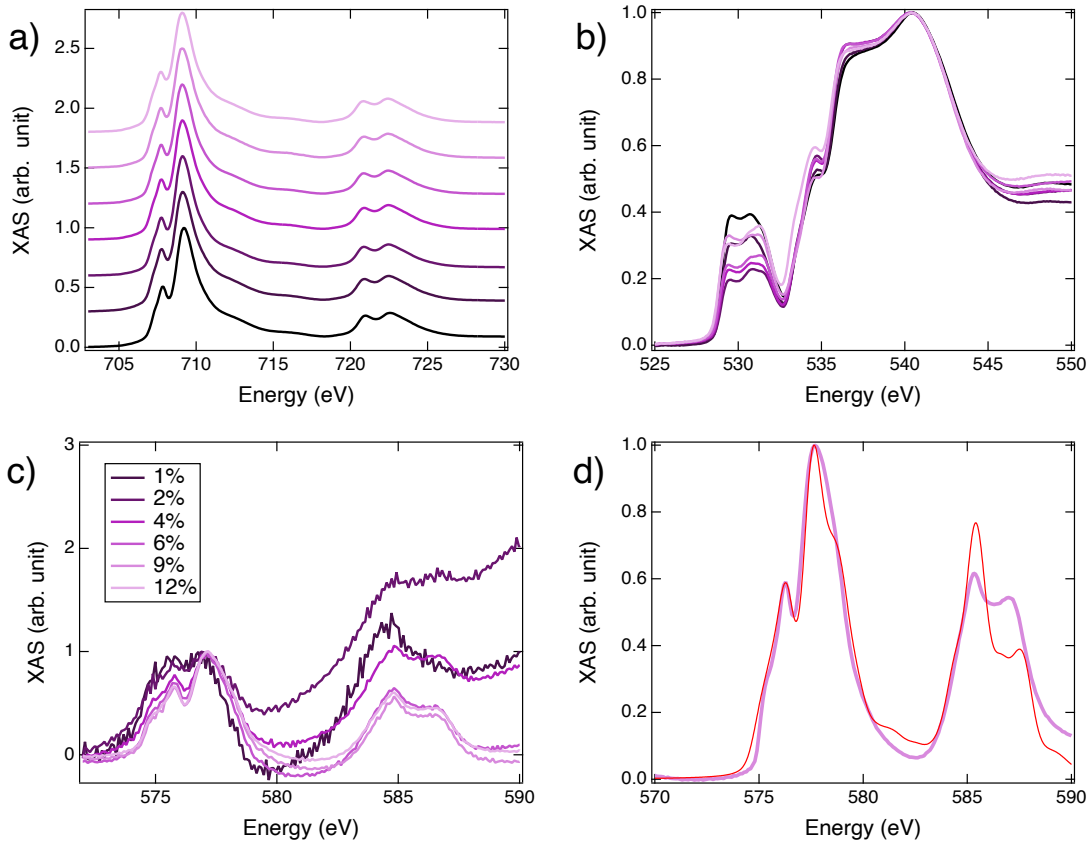

Figure 5.30: XAS spectra of Cr-doped ϵ-Fe_2O_3 nanoparticles collected at 50 K of a) Fe $L_{3,2}$ edge, b) O K edge, and c) Cr $L_{3,2}$ edge. d) Cr $L_{3,2}$ edge of 9% Cr sample with simulated spectrum (red) as described in the text.

observed in the Fe $L_{3,2}$ edge as a function of Cr concentration, indicating that the valance and coordination of the Fe ions is unaffected. In contrast, clear changes to the $2p-3d$ hybridization region are evident in the O K edge spectra. Such changes to hybridization are the source of the variations in local electronic environment around the Fe ions quantified via the Cr-concentration dependent Mössbauer hyperfine parameters (figure 5.15). The maximum amplitude of the O K edge pre-peak first decreases with Cr concentration, reaching a minimum amplitude for the 2% Cr-doped nanoparticles before increasing with further doping. This coincides with the concentrations where δ_{Td} in the 10 K Mössbauer spectra plateaus (see figure 5.15) as the nuclear electronic density becomes constant with additional Cr content. So while the density of electrons around the T_d site are constant for Cr concentrations >2%, enhanced hybridization and orbital overlap occurs. With the Fe $L_{3,2}$ edge showing no change to the Fe electronic structure, the O orbitals must be altered by the incorporation of Cr ions.

As with the undoped ϵ-Fe_2O_3, temperature dependent Mössbauer spectra of the 4% Cr-doped nanoparticles were collected across the magnetic transition. The goal for these measurements is to identify differences in the evolution of the local electronic environment due to Cr-doping. This particular concentration of Cr was chosen because both the Mössbauer and O K edge XAS spectra show modified hybridization due to Cr-doping, yet the Mössbauer spectral line width (Γ) at 10 K remains small enough for differences to be identified.

As discussed in Section 5.1.3, the 10 K spectrum of the 4% Cr-doped ϵ-Fe_2O_3 nanoparticles is well-described with a three component fit corresponding to the known

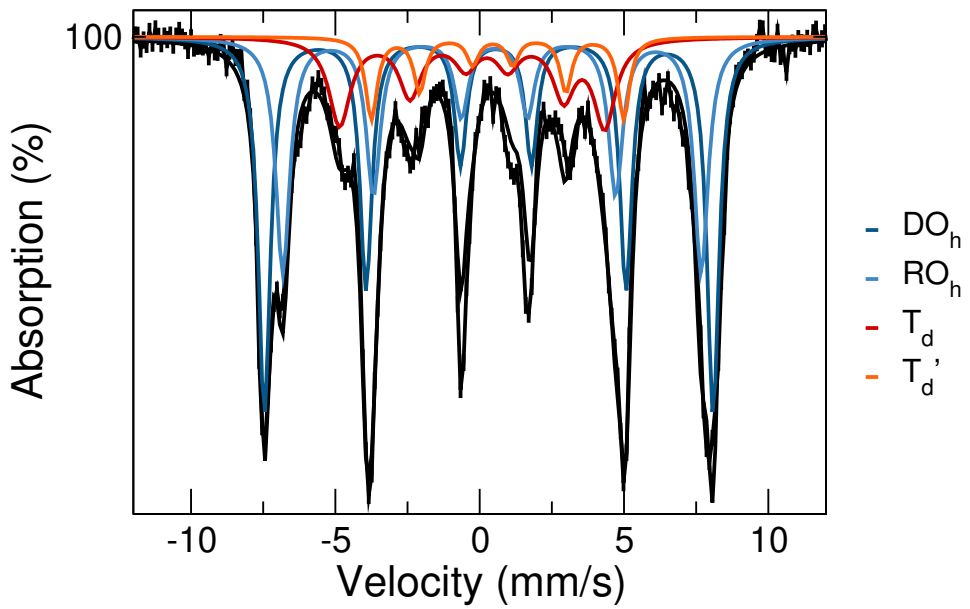

Figure 5.31: Mössbauer spectrum of the 4% Cr-doped ϵ-Fe_2O_3 nanoparticles at 200 K with fit (solid black). Dark blue, light blue, red and orange lines are the individual DO_h, RO_h, T_d and T_d' components as described in the text.

structure of ϵ-Fe_2O_3. Such a model holds true throughout the low temperature incommensurate phase. However, at 135 K (the start of the electronic phase transition) a fourth component is required. Figure 5.31 shows the fit 200 K spectrum of the 4% Cr-doped ϵ-Fe_2O_3. From its anomalously small B_{hf}, and fact that its relative site area is directly proportional to the reduced area of the original T_d component, this new component has T_d coordination and will be referred to as T_d'.

Figure 5.32 shows the temperature dependent isomer shifts ($\delta(T)$) of both the undoped and 4% Cr-doped ϵ-Fe_2O_3. In the low temperature regime (<135 K), $\delta(T)$ of the 4% Cr nanoparticles are the same as the undoped ϵ-Fe_2O_3, and all values are consistent with Fe^{3+}. Small differences between δ_{Oh} and δ_{ROh} do indicate that the nuclear electronic density of the RO_h sites is slightly reduced from that of the

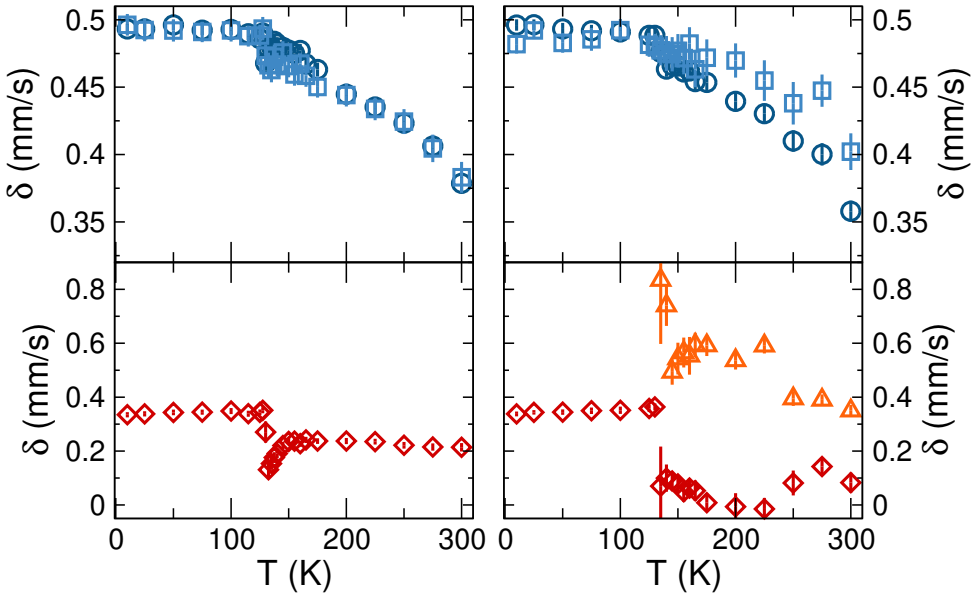

Figure 5.32: Temperature dependent isomer shifts ($\delta(T)$) of the undoped (left) and 4% Cr-doped (right) ϵ-Fe_2O_3 nanoparticles. Dark blue circles are DO_h component, light blue squares are RO_h and red diamonds are T_d. Orange triangles are new T_d' component.

DO_h sites. Such a change is consistent with the reduced $2p-3d$ hybridization seen in the O K edge. Above 135 K $\delta(T)$ of the 4% Cr-doped nanoparticles show clear differences for all but the DO_h component. δ_{ROh} is consistently increased, while the original T_d component no longer shows the two-stage electronic rearrangement seen in the undoped ϵ-Fe_2O_3 nanoparticles. Instead, δ_{Td} decreases and remains very small – consistent with Fe^{4+}-like behaviour. Interestingly, the new T_d' component has a very high δ of 0.8 ± 0.2 mm/s at 135 K, before settling to ~0.55 mm/s between 150 K and 250 K –consistent with Fe^{2+}. The splitting of δ_{Td} in this manner is a sign of charge ordering amongst the T_d sites, where the rearrangement of electrons yields two distinct local environments.

The effect of this charge ordering is apparent in the quadrupole splitting (Δ)

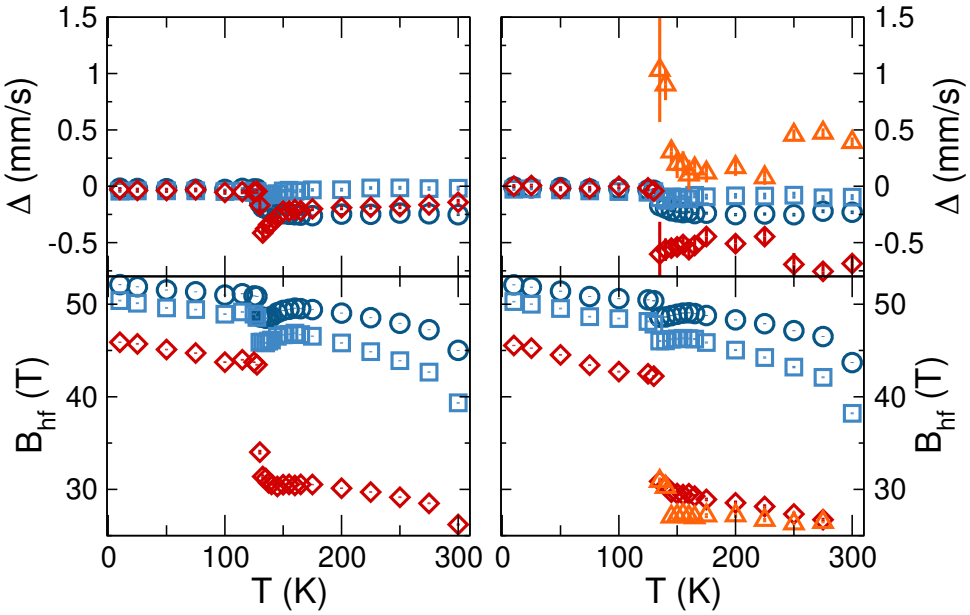

Figure 5.33: Temperature dependent quadrupole splitting ($\Delta(T)$) and hyperfine field ($B_{hf}(T)$) of the undoped (left) and 4% Cr-doped (right) ϵ-Fe_2O_3 nanoparticles. Dark blue circles are DO_h component, light blue squares are RO_h and red diamonds are T_d. Orange triangles are new T_d' component.

shown in figure 5.33 above 135 K (no differences are visible in the low temperature phase). The magnitudes of both Δ_{Td} and $\Delta_{Td'}$ are increased compared to that of the undoped ϵ-Fe_2O_3 indicating increased distortion to the local environment. Meanwhile, the signs are related to the shape of this anisotropy. The negative values of Δ_{Td} describe the distortion being elongated in the direction of the spin, while the positive values of $\Delta_{Td'}$ indicate the gradient is flattened in the spin direction. Regarding the O_h components, Δ_{ROh} is slightly reduced compared to that of undoped ϵ-Fe_2O_3, while Δ_{DOh} is unchanged. Neither O_h component shows variations in B_{hf}. All the T_d component B_{hf} are in agreement below 145 K, above which B_{hf} of both T_d sites in the Cr-doped ϵ-Fe_2O_3 nanoparticles are reduced. With both Fe^{2+} and Fe^{4+} containing

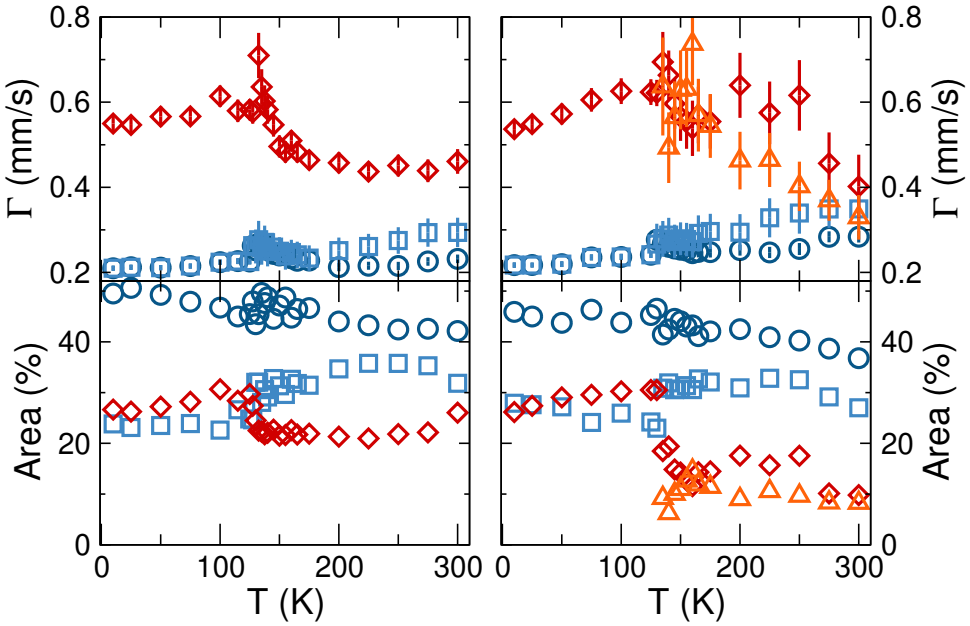

Figure 5.34: Temperature dependent line width ($\Gamma(T)$) and area of the undoped (left) and 4% Cr-doped (right) ϵ-Fe_2O_3 nanoparticles. Dark blue circles are DO_h component, light blue squares are RO_h and red diamonds are T_d. Orange triangles are new T_d' component.

fewer unpaired valence electrons than Fe^{3+}, such a decrease is expected for this charge-ordered state because the difference between spin-up and spin-down densities will be reduced.

As with the other hyperfine parameters, Γ of the 4% Cr-doped ϵ-Fe_2O_3 nanoparticles does not differ from the undoped ϵ-Fe_2O_3 in the low temperature phase (see figure 5.34). Above 135 K both Γ_{Oh} are increased, indicating that the addition of Cr ions increases disorder to these sites. $\Gamma(T)$ is increased for both T_d components, with the Fe^{4+}-like component being the most disordered. The relative site area of the DO_h component is consistently decreased compared to the undoped ϵ-Fe_2O_3 nanoparticles as expected for Cr-doping into the DO_{h1} site. Meanwhile the areas for the T_d and T_d' sites account for nearly equal spectral weights revealing that the low tempera-

ture Fe^{3+} T_d component splits evenly into Fe^{4+}-like and Fe^{2+}-like components above 135 K.

To see if this T_d site charge ordering occurs for ϵ-Fe_2O_3 nanoparticles doped with other transition metal ions, temperature dependent Mössbauer spectra were collected for both the 4% Mn- and 2% Co-doped nanoparticles. Both of these systems are well-described by the usual three components (DO_h, RO_h and T_d), and so confirm that the Cr-doped ϵ-Fe_2O_3 nanoparticles are unique. Temperature dependent hyperfine parameters shown in figure 5.35 reveal that as with the Cr-doped ϵ-Fe_2O_3, the T_d hyperfine parameters above 135 K are most impacted by the addition of the

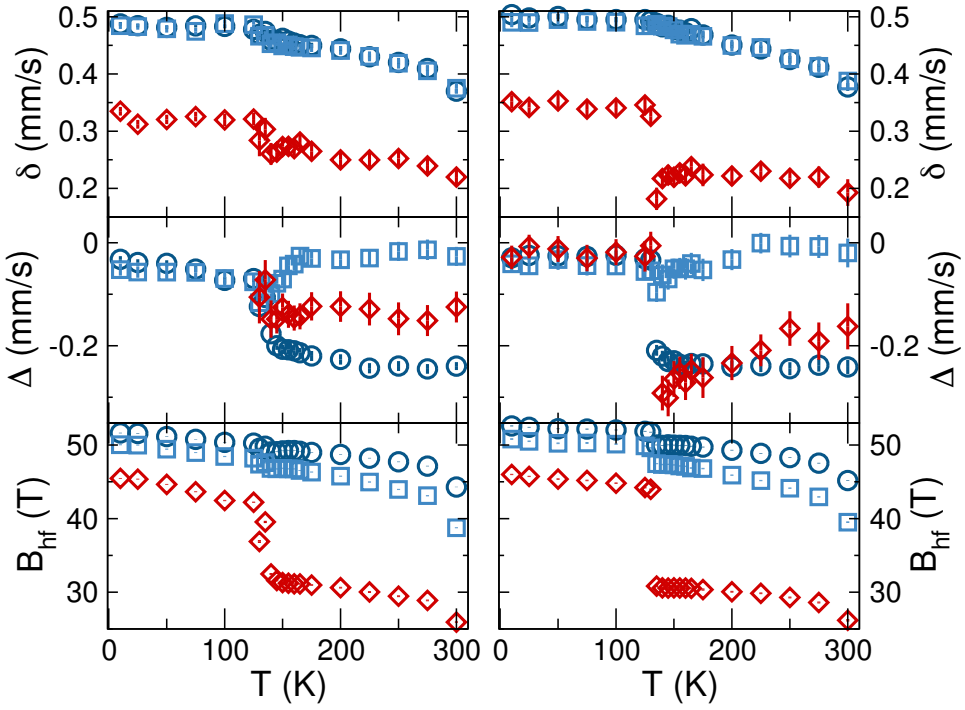

Figure 5.35: Temperature dependent isomer shifts ($\delta(T)$), quadrupole splitting ($\Delta(T)$) and hyperfine field ($B_{hf}(T)$) of the 4% Mn- (left) and 2% Co-doped (right) ϵ-Fe_2O_3 nanoparticles. Dark blue circles are DO_h component, light blue squares are RO_h and red diamonds are T_d.

transition metal ions. Neither the Mn- or Co-doped $\delta_{Td}(T)$ show the clear two-stage transition of undoped ϵ-Fe_2O_3. Instead the 4% Mn-doped $\delta_{Td}(T)$ exhibits only a small decrease at 135 K due to its reduced low temperature $\delta_{Td}(T)$ and increased high temperature $\delta_{Td}(T)$ compared to those of undoped ϵ-Fe_2O_3. $\Delta_{Td}(T)$ of the 4% Mn-doped nanoparticles is consistent with $\delta_{Td}(T)$ with its reduced magnitude reflecting a weaker electric field gradient above 135 K. $B_{hf}(T)$ of the RO_h site is increased throughout the measured temperature range, and neither $B_{hf,Oh}(T)$ show the dip immediately above 135 K seen in the undoped or 4% Cr-doped ϵ-Fe_2O_3.

The values for $\delta_{Td}(T)$ of the 2% Co-doped nanoparticles are very similar to those of the undoped nanoparticles in both the high and low temperature regimes, albeit with a much smaller dip at the transition due to a reduced pull-push of electrons around the T_d site. $\Delta_{Td}(T)$ indicates a significant electric field gradient just above 135 K; however, it linearly decreases in magnitude with increasing temperature. This behaviour contrasts with all of the other samples measured, where $\Delta_{Td}(T)$ is practically constant above 150 K. $B_{hf}(T)$ of all components are increased throughout the low temperature range as discussed previously (see figure 5.17); however, no such increases are observed above 135 K. Like the 4% Mn-doped nanoparticles, the 2% Co-doped $B_{hf,Oh}(T)$ do not show the dip immediately above the transition.

Note that these Mössbauer hyperfine parameters only provide information about the local electronic environment around the Fe ions. To form a better understanding the different systems, the dopant ions themselves need to be considered. Table 5.6 summarizes our understanding of the Cr, Mn and Co dopants. Of these dopant ions Cr^{3+} is the only one that is not mixed valence; however, it is also the only dopant

Table 5.6: Summary of dopant ion results for transition metal-doped ϵ-Fe_2O_3 nanoparticles. Ionic radii from reference 122 where LS and HS indicate the radius for low spin and high spin, respectively.

Dopant	Valence	# d Electrons	Site	Ionic Radius (Å)
Cr	3+	3	DO_{h1}	0.615
Mn	3+ (33%)	4	DO_{h2}	0.58 (LS)
	2+ (67%)	5	DO_{h2}	0.83 (HS)
Fe	3+	5	O_h	0.645 (HS)
Co	3+ (50%)	6	RO_h	0.545 (LS)/0.61 (HS)
	2+ (50%)	7	RO_h	0.65 (LS)/0.745 (HS)

that causes the Fe^{3+} T_d to split into different valences in the high temperature phase. Such a significant disruption to the local electronic environment would be expected to impact the Cr-doped ϵ-Fe_2O_3's unique magnetic behaviour, as charge ordering would modify the exchange interactions. However, the effects of Cr-doping on $M_S(T)$ are consistent throughout the entire temperature range (10-300 K), not just above 135 K where the T_d site shows charge ordering. Thus the origin of the altered magnetism cannot just be the charge ordering in the high temperature phase.

Of all the transition metal ions studied, Cr^{3+} is unique in that it is the only dopant ion that occupies the DO_{h1} sites. While both the DO_{h1} sites and RO_h sites form edge-shared O_h chains along the a-axis, the temperature dependent hyperfine parameters of the undoped ϵ-Fe_2O_3 (specifically $\Delta(T)$ −see figure 4.18) show that the DO_h component's local electronic environment is significantly affected by the reorganization of electrons around the T_d site. The combination of structure and interactions with the T_d sites makes the DO_{h1} sites critical to the overall behaviour of ϵ-Fe_2O_3. The relatively reduced impact of doping into the DO_{h2} (Mn) or RO_h (Co,

Ni, Cu, Zn) sites emphasizes that these sites play a lesser role.

5.3 Summary

Transition metal-doped ϵ-Fe_2O_3 nanoparticles were examined to better understand the ϵ-Fe_2O_3 phase. Six series of nanoparticle samples were prepared, each doped with a single transition metal ion: Cr, Mn, Co, Ni, Cu or Zn. XAS spectra of the dopant ions were used to identify their valence and coordination. All of the dopant ions are O_h coordination, and so the T_d site that transforms with the magnetic transition is not directly altered. Instead Cr^{3+} ions occupy the DO_{h1} site, $Mn^{2+/3+}$ ions occupy DO_{h2} site, and $Co^{2+/3+}$, Ni^{2+}, Cu^{2+} and Zn^{2+} ions all occupy the RO_h site. Based on the concentrations where spinel-like reflections appear, both of the DO_h sites are able to accommodate more dopant ions than the RO_h sites.

The impact of the transition metal dopants on the magnetism of ϵ-Fe_2O_3 nanoparticles is remarkably independent of the dopant species, and all samples exhibit the characteristic magnetic transition. Most of the changes to $\mu_0 H_C(T)$ can be ascribed to either size effects or the breakdown of the perovskite structure. The Co ions are an exception, with increased low temperature and decreased high temperature $\mu_0 H_C(T)$ reflecting changes to the spin-orbit coupling. For $M_S(T)$, all but the Cr-doped ϵ-Fe_2O_3 nanoparticles show increased $M_S(T)$ with increased dopant concentration. In contrast, the dependent of M_S on Cr doping concentration is non-monotonic. Temperature dependent Mössbauer spectroscopy shows that the Cr-doped ϵ-Fe_2O_3 have a charge-ordered T_d site above 135 K. Because the unusual behaviour of $M_S(T)$ with Cr concentration extends to the low temperature phase as well, the T_d charge ordering is

not the origin. Instead, both are the result of perturbing the DO_{h1} sites which form O_h chains and are coupled to the T_d sites. These results reveal that the DO_{h1} site is critical to the overall magnetic properties of ϵ-Fe_2O_3, and presents a mechanism to tune this novel multiferroic phase.

Chapter 6

Discussion

In the previous chapters, the roles of hybridization in Fe_3O_4 nanorods (chapter 3) and ϵ-Fe_2O_3 nanoparticles (chapters 4 and 5) have been considered independently. As discussed in chapter 3, the full transformation of the Fe_3O_4 nanorods is well-described by the trimeron model. In this chapter the results of chapters 4 and 5 will be used to put forward a model for the ϵ-Fe_2O_3 transition. A comparison of these systems will further enhance our understanding of the physics that underpins the iron oxides.

Both the Verwey transition of Fe_3O_4 and the magnetic transition of ϵ-Fe_2O_3 show clear changes to the local Fe environment via their temperature dependent hyperfine parameters (see figures 3.13 and 4.18). In Fe_3O_4, the Verwey transition occurs via the transformation of the O_h sites. The nature of this transformation is such that the hyperfine parameters of the single high temperature O_h component are nearly the average of the multiple low temperature components. Intuitively this behaviour makes sense because the low temperature ordered Fe^{2+} and Fe^{3+} components become

$Fe^{2.5+}$-like via electron hopping above T_V.

The transition is ϵ-Fe_2O_3 is quite different. In the undoped ϵ-Fe_2O_3, only a single Fe^{3+} T_d component describes the entire temperature range, though these hyperfine parameters do vary across the transition. In particular, $\delta_{Td}(T)$ shows clear variations at the transition and $B_{hf}(T)$ above the transition is strangely low for Fe^{3+}. The rearrangement of electrons that changes $\delta_{Td}(T)$ also creates anisotropy in the electric field gradient (tracked by $\Delta(T)$). Complementary techniques provide further insights by showing no changes to the crystal structure or the valence and coordination of the Fe ions. However, Fe $L_{3,2}$ XAS spectra reveal that ϵ-Fe_2O_3 shows strong covalency, meaning that electrons can be shifted and shared between ions.

From the temperature dependent hyperfine parameters of the undoped and Cr-doped ϵ-Fe_2O_3 nanoparticles (Figures 5.32, 5.33, and 5.34), the incorporation of dopant ions alters this covalency. The most notable consequence is the appearance of charge ordering with Cr^{3+} doping into the DO_{h1} site. Careful examination of these two T_d components (with apparent valences of 2+ and 4+) reveals that the average $\delta(T)$ and $\Delta(T)$ of these components map almost perfectly onto $\delta(T)$ and $\Delta(T)$ of the undoped ϵ-Fe_2O_3. Such behaviour indicates that the T_d site of the undoped ϵ-Fe_2O_3 above the transition is similar to that of the O_h site in Fe_3O_4 where one component is sufficient to describe a mixed valence system. In the Cr-doped ϵ-Fe_2O_3, the Cr^{3+} ions perturb the T_d sites such that two Fe valences appear at the time scale of the Mössbauer measurement. We propose that the Fe^{2+}/Fe^{4+} character is also present in the undoped ϵ-Fe_2O_3. Such a model is supported by the strangely low $B_{hf,Td}$ above the transition since both Fe^{2+} and Fe^{4+} will have a smaller difference between spin-up

and spin-down densities than Fe^{3+}.

In Fe_3O_4, the electronic configuration is relatively straightforward: distinct Fe^{2+} and Fe^{3+} valence occurs when the d electrons are localized, while $Fe^{2.5+}$ valence appears when the lone minority spin t_{2g} electron hops between the double exchange-coupled Fe^{2+} and Fe^{3+} sites. In ϵ-Fe_2O_3 a more complicated mechanism is necessary because the T_d sites are ferromagnetically coupled and all d orbitals are half-filled. With this configuration, Hund's rules indicate that the simple transfer of electrons between d orbitals is not permitted[11] and the charge transfer must occur via another mechanism.

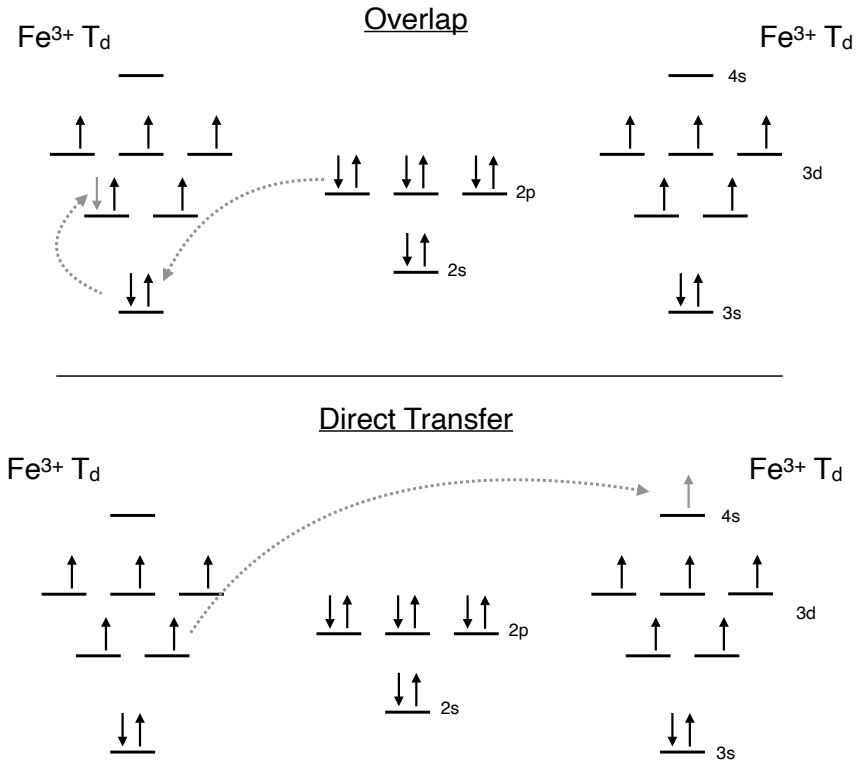

Figure 6.1: Mechanisms of overlap (top) and direct transfer (bottom) hyperfine interactions between T_d Fe^{3+}, mediated by O^{2-}.

Because ϵ-Fe_2O_3 has a covalent nature, cation-cation (Fe1-O-Fe2) supertransferred hyperfine interactions need to be considered, of which there are two possible mechanisms (shown in figure 6.1). The first occurs when overlap between O σ (p or s) orbitals and Fe2 core σ orbitals cause the unpairing of Fe2 spins. This unpaired spin density is caused by the transfer of a ligand σ electron to Fe1. For the second mechanism, a $3d$ electron is transferred from Fe1 into an empty s orbital of Fe2 via either a direct process or through the O ligands. Both of these processes change the effective valency/spin density between the Fe1 and Fe2 ions in a manner consistent with charge transfer while not splitting δ.[128]

The overall impact on δ does differ between these two hyperfine interactions. Overlap distortions cause core electrons to shift outwards, lowering $\rho_s(0)$ and increasing δ.[129] In contrast, increased mobility of d electrons via direct transfer causes $\rho_s(0)$ to increase and δ to decrease.[130] Based on the initial sharp decrease of $\delta_{Td}(T)$ at the transition, direct transfer interactions occur initially then overlap interactions appear. Note that if both interactions are equally present, the impact on δ is minimal. Thus the decrease in $\delta_{Td}(T)$ above 150 K reflects ϵ-Fe_2O_3 favouring direct transfer interactions. However, both these interactions impact the other hyperfine parameters. B_{hf} decreases via a reduction in the difference between spin-up and spin-down densities (see figure 6.1) while distortions to both the Fe T_d and neighbouring O^{2-} orbitals alter Δ of the DO_h sites. Overall, these hyperfine interactions create the unique local environment of the T_d site above 150 K in ϵ-Fe_2O_3.

Note that of the transition metal-doped nanoparticles where full temperature dependent hyperfine parameters were acquired (see Figures 5.32, 5.33, 5.34, and 5.35),

only the Cr-doped sample shows the splitting of the T_d site. Much of the unique behaviour of the Cr-doped ϵ-Fe_2O_3 nanoparticles has been attributed to its occupancy of the DO_{h1} site, and this may indeed play a role. However, the other dopants studied were Mn and Co – both of which are occupied by mixed 2+/3+ valence, and have more mechanisms to interact with ϵ-Fe_2O_3. For example, the incorporation of 2+ ions requires O^{2-} vacancies to form to maintain charge balancing requirements. The location of these vacancies will have consequences for the hyperfine interactions that underpin the changes to the local T_d environment. Additionally, both Mn^{3+} and Co^{2+} are orbitally degenerate and thus Jahn Teller-active resulting in the potential to generate either structural or dynamic electronic local distortions. The importance of these effects (vacancies, distortions etc.) will be convolved with how strongly the different transition metal ions couple to the existing Fe ions.

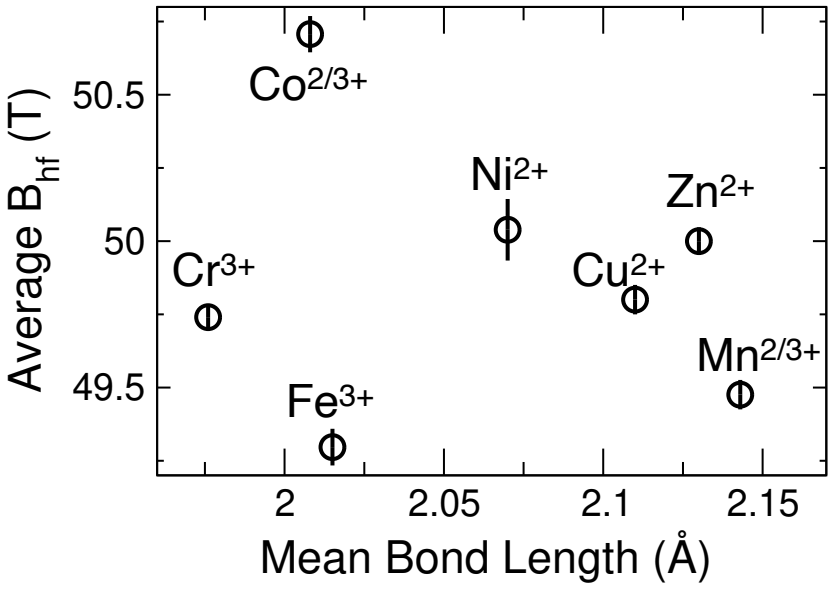

Figure 6.2: Average $B_{hf}(10\ K)$ of 4% transition metal-doped ϵ-Fe_2O_3 nanoparticles as a function of mean M-O bond length in O_h coordination.

One means to assess how the transition metal ions interact with the Fe ions is to examine the correlation between B_{hf} and the average M-O bond length. Because the external $\vec{B}$ field experienced by an Fe site decreases as the distance between ions increases, changes to B_{hf} should also decrease as the M-O bond length increases. While reflection broadening in the XRD patterns makes experimental determination of these bond lengths impossible for the nanoparticle samples, average M-O bond lengths are known.[125] The relationship between the average B_{hf} of the three Fe components as a function of the mean M-O bond length is shown in figure 6.2.[1]

Most of the transition metal ions follow the expected trend with the average B_{hf} value decreasing to reach that of the undoped ϵ-Fe_2O_3 as the mean bond length increases. Notably, the relatively short M-O bond lengths for Co and Ni dopant ions correspond to increased B_{hf}, indicating that the M-O-Fe interactions are fairly strong. In contrast, the ϵ-Fe_2O_3 nanoparticles doped with Cr^{3+} ions show different behaviour. With a smaller M-O bond length than the Fe^{3+} ions, a large change to B_{hf} is predicted; however, only a small increase is measured. This deviation from expectations is consistent with the reduced $2p - 3d$ Fe-O hybridization visible in the pre-peak of the O K edge spectra in figure 5.30 and indicates weak Cr-O-Fe interactions. Such reduced hybridization interferes with the ϵ-Fe_2O_3 supertransferred hyperfine interactions and leads to the appearance of T_d site charge ordering in the Cr-doped ϵ-Fe_2O_3 nanoparticles above the magnetic transition.

Thus far, much of the focus has been on the more common Fe-O $2p - 3d$ hybridization; however, changes to the $2p - 4sp$ region of the O K edge spectra are

[1] A weighted average of the two valences was used for Mn and Co corresponding to the XAS results.

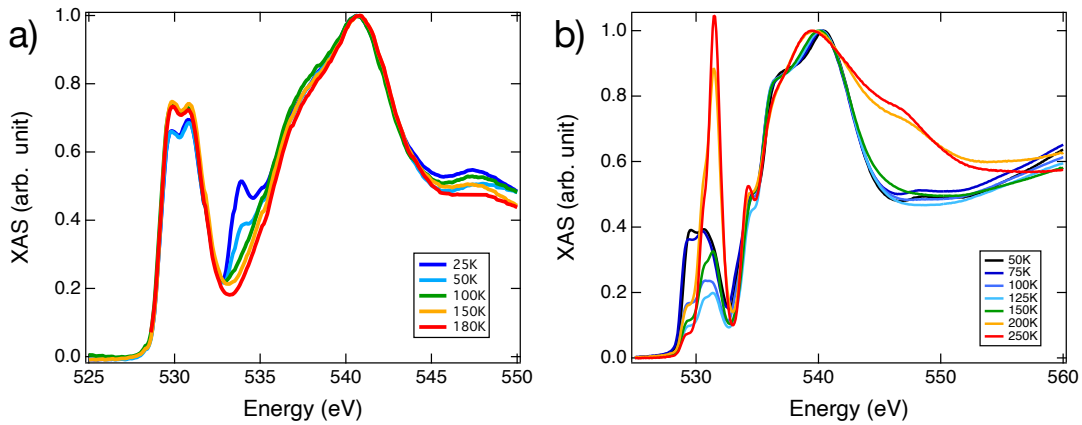

Figure 6.3: Temperature dependent O K edge of a) 700 nm Fe_3O_4 nanorods and b) 15 nm ϵ-Fe_2O_3 nanoparticles.

also visible in ϵ-Fe_2O_3. Figure 6.3 shows the temperature dependent O K edge of the Fe_3O_4 nanorods and ϵ-Fe_2O_3 nanoparticles for comparison. Both of these systems show changes to the pre-peak across their respective transitions as the $2p-3d$ hybridization changes. Temperature dependent Mössbauer hyperfine parameters (see Figures 3.13 and 4.18) provide complementary information about the changes to the local Fe environment and show how Fe-O hybridization controls both the Verwey transition in Fe_3O_4 and the magnetic transition in ϵ-Fe_2O_3. However, no such change in hyperfine parameters occurs in the ϵ-Fe_2O_3 at 200 K when the $2p-4sp$ spectral changes occur. Although the $2p-3d$ pre-peak also transforms, the absence of variations in the Fe local environment indicates that this behaviour must originate from the O ions. To explain why the $2p-4sp$ variations occur in ϵ-Fe_2O_3 and not Fe_3O_4, the individual structures need to be considered.

While Fe_3O_4 and ϵ-Fe_2O_3 both contain only Fe and O atoms, their structures are very different (as shown in figure 6.4). Fe_3O_4 is composed of two interpenetrating

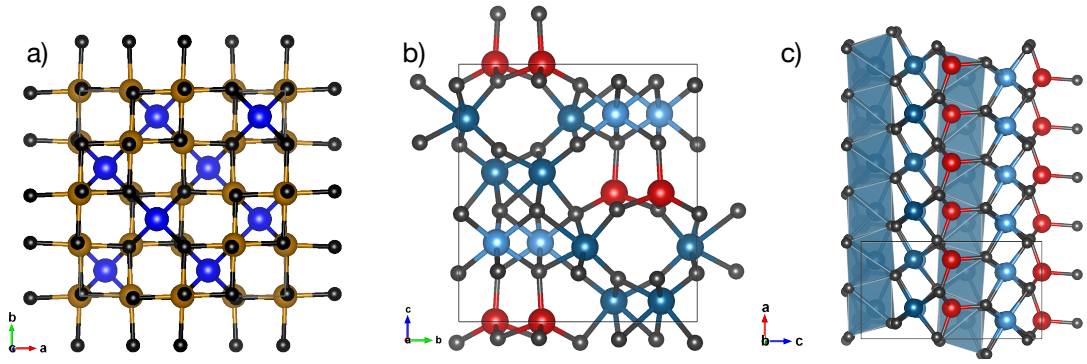

Figure 6.4: a) Structure of Fe_3O_4 where Fe T_d are blue, Fe O_h are gold, and O are black. b) Structure of ϵ-Fe_2O_3 where Fe T_d are red, Fe DO_h are dark blue, Fe RO_h are light blue and O are black c) ϵ-Fe_2O_3 structure showing DO_{h1} chains where surrounding O ions can interact.

lattices – one of Fe^{3+} in T_d coordination and the other of Fe^{2+} and Fe^{3+} in O_h coordination. These combine to form an ordered, high-symmetry spinel structure. In contrast, ϵ-Fe_2O_3 has much lower symmetry. None of the O_h sites show the ideal 180° O-Fe-O bond angles, and two of the three O_h sites (the DO_h sites) exhibit disordered bond lengths. These distortions combine to yield a complex structure – most notably, O-O nearest neighbours appear. These are located alongside the DO_{h1} chains (shown in figure 6.4c) that were found to be critical to the magnetism of ϵ-Fe_2O_3. Overall, the perovskite structure of ϵ-Fe_2O_3 permits O-O interactions, which are not possible in the Fe_3O_4 structure. These correlated O are most like the source of the $2p - 4sp$ variations in the ϵ-Fe_2O_3 O K edges.

The role of O-O hybridization in ϵ-Fe_2O_3 is unclear. Temperature dependent susceptibilities (see figure 4.6) only reveal a single transition ending at 150 K which maps on to the changing $2p - 3d$ hybridization. The temperature dependent f-factor and Mössbauer hyperfine parameters (Figures 4.17 and 4.18) show the same behaviour, and even the conductivity of the O K edge XAS signal (figure 4.16) exhibits

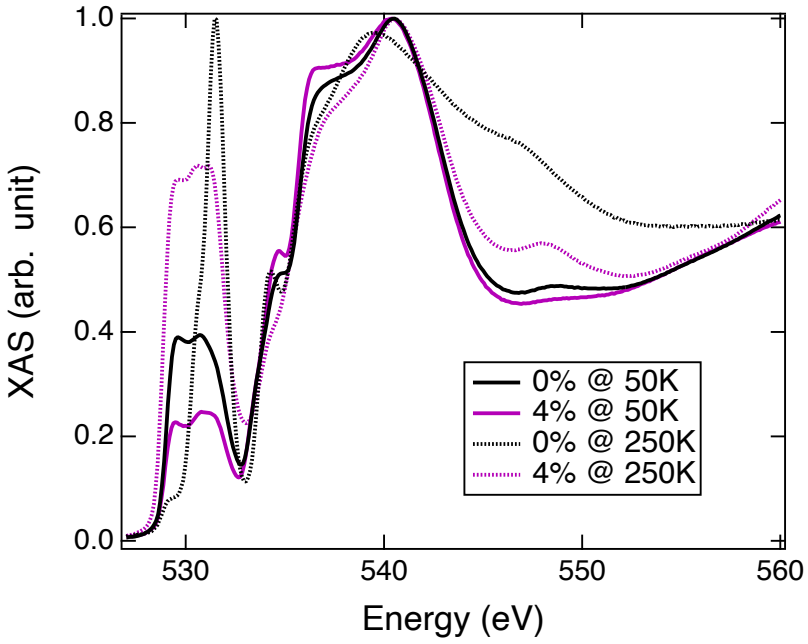

Figure 6.5: O K edge XAS spectra of undoped and 4% Cr-doped ϵ-Fe_2O_3 nanoparticles at 50 K and 250 K.

a single discontinuity between 100 K and 125 K. As with the Verwey transition in Fe_3O_4, Fe-O hybridization explains most of the temperature dependent behaviour of ϵ-Fe_2O_3.

For further insights, we turn to the Cr-doped ϵ-Fe_2O_3 nanoparticles. Because O-O nearest neighbours occur alongside the DO_{h1} chains, perturbation of this site should impact the neighbouring O ions. O K edge XAS spectra at 50 K and 250 K of the undoped and 4% Cr-doped ϵ-Fe_2O_3 nanoparticles are shown in figure 6.5. Clear differences in spectral shape are apparent, specifically at 250 K. The $2p-3d$ pre-peak of the 4% Cr-doped ϵ-Fe_2O_3 spectrum does not narrow and shift to higher energies, while the overall shape of the $2p-4sp$ feature is more consistent with the 50 K spectra than the undoped ϵ-Fe_2O_3 at 250 K. Thus the 4% Cr-doped ϵ-Fe_2O_3 spectrum does

not show evidence of O-O interactions. Interestingly, their absence is not noticeable in the overall magnetic properties, confirming that Fe-O hybridization has a greater impact on magnetism, leaving the role of O-O hybridization undefined.

ϵ-Fe_2O_3 does have one notable property that has yet to be discussed: its multiferroic behaviour. In addition to ferrimagnetism, this phase is reported to exhibit ferroelectric behaviour at room temperature.[44,131,132] Having neither d^0 or lone pair configuration (see section 1.5 for explanation of these configurations), ϵ-Fe_2O_3 must exhibit novel ferroelectricity. This property could be affected by the O-O hybridization. Mössbauer spectra were collected on undoped ϵ-Fe_2O_3 in an applied electric field. Figure 6.6 shows δ_{Td} and the relative site areas as a function of applied field strength. Variations in δ_{Td} are consistent with the theory that O-O hybridization along the DO_{h1} chains plays a role in the ferroelectricity of ϵ-Fe_2O_3 because the T_d and DO_{h1} sites are coupled through these O ions. The cause of the relative site area variations is less clear; however, it could be due to the electric field affecting the

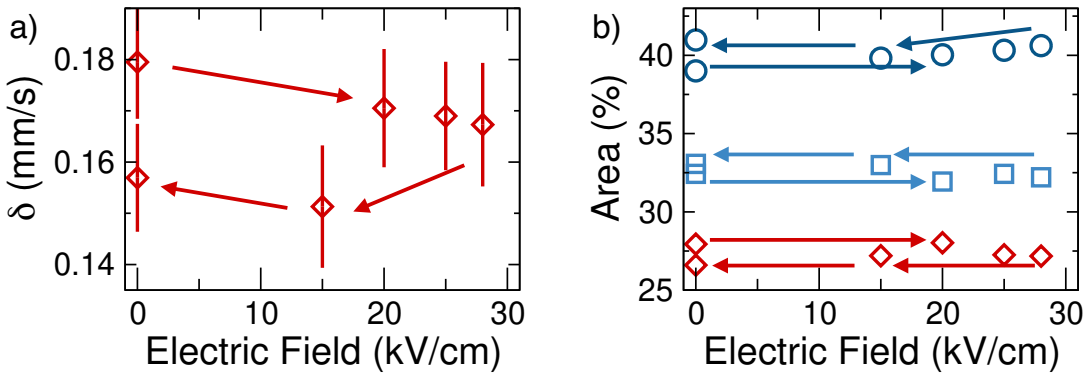

Figure 6.6: a) δ_{Td} and b) relative site areas as a function of applied electric field. DO_h, RO_h and T_d sites shown as dark blue circles, light blue squares and red diamonds, respectively. Arrows used to indicate hysteresis.

lattice coupling of the sites differently. This data suggests that the applied electric field weakens the coupling of the T_d sites to the lattice. Future measurements using stronger applied electric fields will provide further insights into ϵ-Fe_2O_3's ferroelectric behaviour, while measurements of the Cr-doped ϵ-Fe_2O_3 nanoparticles will confirm the role of O-O interactions.

Chapter 7

Conclusions & Future Work

The polymorphs of iron oxide exhibit astonishing complexity considering their simple chemical composition. Variations in structure, electron correlations and competing degrees of freedom result in a wide range of unique states. In this work, Fe_3O_4 and the novel ϵ-Fe_2O_3 phase were examined. Both of these iron oxide phases exhibit temperature dependent transitions driven by Fe-O hybridization. By characterizing the evolution of these transitions, insights into the underlying physics are obtained.

In chapter 3, three different sizes of Fe_3O_4 nanorods were studied to examine the relationship between strain and the Verwey transition – the archetypal metal-insulator transition. Both the 40 nm and 50 nm nanorods, which exhibit isotropic compressive crystal strain show reduced T_V of 40 K and 80 K, respectively, compared to the $\sim$120 K observed in bulk crystals. In contrast, the 700 nm nanorods with uniaxial tensile strain exhibit an increased T_V of 150 K. Detailed examination of the 700 nm nanorods was performed to better understand the relationship between T_V and strain. A variety of spectroscopic techniques were used to confirm the formation of orbitally-ordered

trimerons in the low temperature insulating phase; however, deviations from the expected microstructure of bulk Fe_3O_4 are evident. These shifts in microstructure are the result of crystal strain, and result in altered hybridization in the trimeron phase. Such variations in hybridization change the overall energy landscape of the system and result in the shifted T_V observed for the Fe_3O_4 nanorods. These results reveal that crystal strain is a potential mechanism to tune the metal-insulator transition, and conversely, that the metal-insulator transition temperature can be used as an indicator of crystallite strain.

Chapters 4 and 5 both examined ϵ-Fe_2O_3-based nanoparticles. Compared to Fe_3O_4, this phase is not well understood and so comprehensive characterization was performed. Because this phase is only stable in the nanoscale, the initial goal was to decouple the effect of nanoparticle morphology from the overall behaviour of the ϵ-Fe_2O_3 phase. Three different sizes were examined (15, 20, and 30 nm), and variations in Fe-O $2p - 3d$ hybridization at low temperatures (<150 K) are apparent. This altered hybridization has negligible impact on the overall magnetic properties when comparing the three nanoparticle samples, and instead the variations in M_S, χ_{DC} and $\mu_0 H_C$ are due to finite size effects from broken surface coordinate and reduced long-range ordering. Similar to the behaviour observed in the Fe_3O_4 nanorods, the strengthened hybridization of the 30 nm ϵ-Fe_2O_3 nanoparticles does shift the characteristic transition to slightly higher temperatures. However, the behaviour of the hyperfine parameters does not change as a function of nanoparticle size, with the samples exhibiting multistage electronic rearrangement of the T_d sites with the characteristic transition.

For further insights into the underlying mechanism behind this transition ϵ-Fe_2O_3 phase, a perturbed system is required. Transition metal-doped ϵ-Fe_2O_3 nanoparticles, where low concentrations of Cr, Mn, Co, Ni, Cu or Zn were incorporated into the crystal, were studied. All of the dopant ions occupy O_h coordination, and all samples exhibit the characteristic magnetic transition. Remarkably, systems where the dopant ions occupy the DO_{h2} and RO_h sites (Mn, Co, Ni, Cu and Zn) induce similar changes to the ϵ-Fe_2O_3 phase; however, the Cr-doped nanoparticles are unique and demand further invesitgation. This series is the only one that exhibits non-linear variations of $M_S(T)$ with respect to doping, indicating significant disruption of exchange interactions. Such disruption occurs because the Cr ions occupy the DO_{h1} site, which forms octahedral chains and is closely coupled to the T_d sites which drive the transition. Because the Cr ions have relatively weak interactions with Fe ions, the effects of Cr-doping provide insights into the interactions that control ϵ-Fe_2O_3. Full tracking of the Cr-doped temperature dependent hyperfine parameters reveal charge ordering of the T_d site above 135 K where the valence appears to be Fe^{2+}/Fe^{4+}, rather than the expected Fe^{3+}. Comparison of the Cr-doped and undoped ϵ-Fe_2O_3 temperature dependent hyperfine parameters reveals that the characteristic transition occurs with the onset of supertransferred hyperfine interactions between T_d sites. It is a combination of these direct transfer and orbital overlap interactions which gives ϵ-Fe_2O_3 its unique properties. Overall, this work provides a physical model of how $2p-3d$ hybridization evolves in ϵ-Fe_2O_3.

In contrast, the changing $2p-4sp$ hybridization (most evident in O K edge XAS spectra) is still not well understood. While this behaviour is proposed to play a role

in the ferroelectric coupling of the ϵ-Fe_2O_3 phase, additional studies are required. Mössbauer spectra collected at room temperature in an applied electric field revealed some changes to the Fe local environment; however, these are only preliminary measurements. Full tracking of the hyperfine parameters in applied electric fields as a function of temperature would identify if the change in $2p - 4sp$ hybridization at 200 K is tied to the ferroelectric coupling. Increasing the electric field strength from that used previously should induce larger changes which will clarify how the Fe local environment responds to the applied electric field. As a more direct probe, measurements of the O K edge XAS spectrum in an applied electric field should reveal any correlations between $2p - 4sp$ hybridization and ferroelectric coupling; however, a compatible beamline will need to be located. For all experimental techniques, comparison of the undoped ϵ-Fe_2O_3 with the transition metal-doped Fe_2O_3 will assist in understanding the mechanisms at play.

Further insights would be obtained via simulations, particularly of the O K edge spectrum. First principle calculations using a program such as Quantum ESPRESSO[133] could be used to develop a model of the electronic structure. Such calculations have been used to simulate the comparatively simpler α-Fe_2O_3 phase reasonably successfully.[134] However, the complexity of the ϵ-Fe_2O_3 structure makes these simulations highly non-trivial. Agreement between the experimental and theoretical results will signal a solid understanding of the novel ϵ-Fe_2O_3 phase.

Bibliography

[1] Rochelle M Cornell, Udo Schwertmann, et al. *The iron oxides: structure, properties, reactions, occurrences, and uses*, volume 664. Wiley-VCH Weinheim, 2003.

[2] JH Ngai, FJ Walker, and CH Ahn. Correlated oxide physics and electronics. *Annual Review of Materials Research*, 44:1–17, 2014.

[3] EJW Verwey. Electronic conduction of magnetite (Fe_3O_4) and its transition point at low temperatures. *Nature*, 144(3642):327–328, 1939.

[4] Friedrich Walz. The Verwey transition – a topical review. *Journal of Physics: Condensed Matter*, 14(12):R285, 2002.

[5] Joaquín García and Gloria Subías. The Verwey transition – a new perspective. *Journal of Physics: Condensed Matter*, 16(7):R145, 2004.

[6] Mark S Senn, Jon P Wright, and J Paul Attfield. Charge order and three-site distortions in the Verwey structure of magnetite. *Nature*, 481(7380):173–176, 2012.

[7] Jean-Louis Dormann, Dino Fiorani, and Elisabeth Tronc. Magnetic relaxation in fine-particle systems. *Advances in Chemical Physics*, 98:283–494, 1997.

[8] Steen Mørup, Daniel E Madsen, Cathrine Frandsen, Christian RH Bahl, and Mikkel F Hansen. Experimental and theoretical studies of nanoparticles of antiferromagnetic materials. *Journal of Physics: Condensed Matter*, 19(21):213202, 2007.

[9] Xavier Batlle and Amílcar Labarta. Finite-size effects in fine particles: Magnetic and transport properties. *Journal of Physics D: Applied Physics*, 35(6):201, 2002.

[10] Jiri Tucek, Radek Zboril, Asuka Namai, and Shin-ichi Ohkoshi. ε-Fe_2O_3: An advanced nanomaterial exhibiting giant coercive field, millimeter-wave ferromagnetic resonance, and magnetoelectric coupling. *Chemistry of Materials*, 22(24):6483–6505, 2010.

[11] Robert C O'Handley. *Modern magnetic materials: Principles and applications*. Wiley, 2000.

[12] John MD Coey. *Magnetism and magnetic materials*. Cambridge University Press, 2010.

[13] John B Goodenough. Theory of the role of covalence in the perovskite-type manganites [La,M(II)]MnO_3. *Physical Review*, 100(2):564, 1955.

[14] Junjiro Kanamori. Superexchange interaction and symmetry properties of electron orbitals. *Journal of Physics and Chemistry of Solids*, 10(2-3):87–98, 1959.

[15] Stephen Blundell. Magnetism in condensed matter, 2003.

[16] Hongxin Yang, Jinghua Liang, and Qirui Cui. First-principles calculations for Dzyaloshinskii–Moriya interaction. *Nature Reviews Physics*, 5(1):43–61, 2023.

[17] Ivan A Sergienko and E Dagotto. Role of the Dzyaloshinskii-Moriya interaction in multiferroic perovskites. *Physical Review B*, 73(9):094434, 2006.

[18] Igor Dzyaloshinsky. A thermodynamic theory of "weak" ferromagnetism of antiferromagnetics. *Journal of Physics and Chemistry of Solids*, 4(4):241–255, 1958.

[19] E H Frei, S Shtrikman, and D Treves. Critical size and nucleation field of ideal ferromagnetic particles. *Physical Review*, 106(3):446, 1957.

[20] EC Stoner and EP Wohlfarth. A mechanism of magnetic hysteresis in heterogeneous alloys. *IEEE Transactions on Magnetics*, 27(4):3475–3518, 1991.

[21] Alberto P Guimarães and Alberto Passos Guimaraes. *Principles of nanomagnetism*, volume 7. Springer, 2009.

[22] Y Labaye, O Crisan, L Berger, Jean-Marc Greneche, and JMD Coey. Surface anisotropy in ferromagnetic nanoparticles. *Journal of Applied Physics*, 91(10):8715–8717, 2002.

[23] R Yanes, O Chubykalo-Fesenko, RFL Evans, and RW Chantrell. Temperature dependence of the effective anisotropies in magnetic nanoparticles with Néel surface anisotropy. *Journal of Physics D: Applied Physics*, 43(47):474009, 2010.

[24] Keith Gilmore, Yves U Idzerda, Michael T Klem, Mark Allen, Trevor Douglas, and Mark Young. Surface contribution to the anisotropy energy of spherical magnetite particles. *Journal of Applied Physics*, 97(10):10B301, 2005.

[25] L Berger, Y Labaye, M Tamine, and JMD Coey. Ferromagnetic nanoparticles with strong surface anisotropy: Spin structures and magnetization processes. *Physical Review B*, 77(10):104431, 2008.

[26] Louis Néel. Anisotropie magnétique superficielle et surstructures d'orientation. *J. Phys. Radium*, 15(4):225–239, 1954.

[27] Walter Kündig and R Steven Hargrove. Electron hopping in magnetite. *Solid State Communications*, 7(1):223–227, 1969.

[28] M Iizumi, TF Koetzle, G Shirane, S Chikazumi, M Matsui, and S Todo. Structure of magnetite (Fe_3O_4) below the verwey transition temperature. *Acta Crystallographica Section B: Structural Crystallography and Crystal Chemistry*, 38(8):2121–2133, 1982.

[29] Javier Blasco, Joaquín García, and Gloria Subías. Structural transformation in magnetite below the Verwey transition. *Physical Review B*, 83(10):104105, 2011.

[30] EJW Verwey, PW Haayman, and FC Romeijn. Physical properties and cation arrangement of oxides with spinel structures II. Electronic conductivity. *The Journal of Chemical Physics*, 15(4):181–187, 1947.

[31] Horng-Tay Jeng, GY Guo, and DJ Huang. Charge-orbital ordering in low-temperature structures of magnetite: GGA+ U investigations. *Physical Review B*, 74(19):195115, 2006.

[32] Mark S Senn, Ingo Loa, Jon P Wright, and J Paul Attfield. Electronic orders in the Verwey structure of magnetite. *Physical Review B*, 85(12):125119, 2012.

[33] Kunihiko Yamauchi and Paolo Barone. Electronic ferroelectricity induced by charge and orbital orderings. *Journal of Physics: Condensed Matter*, 26(10):103201, 2014.

[34] S De Jong, R Kukreja, Christoph Trabant, N Pontius, CF Chang, T Kachel, M Beye, F Sorgenfrei, CH Back, B Bräuer, et al. Speed limit of the insulator–metal transition in magnetite. *Nature Materials*, 12(10):882, 2013.

[35] R Řezníček, V Chlan, H Štěpánková, and P Novák. Hyperfine field and electronic structure of magnetite below the Verwey transition. *Physical Review B*, 91(12):125134, 2015.

[36] H Forestier and G Guiot-Guillain. New ferromagnetic variety of ferric oxide. *CR Acad. Sci.(Paris)*, 199:720, 1934.

[37] JM Trautmann and H Forestier. Nouvelle préparation et étude de l'oxyde ε-Fe_2O_3. *CR Acad. Sci. Paris*, 261:4423–4425, 1965.

[38] I Dézsi and JMD Coey. Magnetic and thermal properties of ε-Fe_2O_3. *Physica Status Solidi (A)*, 15(2):681–685, 1973.

[39] E Tronc, Corinne Chanéac, and JP Jolivet. Structural and magnetic characterization of ε-Fe_2O_3. *Journal of Solid State Chemistry*, 139(1):93–104, 1998.

[40] Martí Gich, Anna Roig, Elena Taboada, Elies Molins, Caroline Bonafos, and Etienne Snoeck. Stabilization of metastable phases in spatially restricted fields: the case of the Fe_2O_3 polymorphs. *Faraday Discussions*, 136:345–354, 2007.

[41] M Gich, C Frontera, A Roig, E Taboada, E Molins, HR Rechenberg, JD Ardisson, WAA Macedo, C Ritter, V Hardy, et al. High-and low-temperature crystal and magnetic structures of ε-Fe_2O_3 and their correlation to its magnetic properties. *Chemistry of Materials*, 18(16):3889–3897, 2006.

[42] Jian Jin, Shin-ichi Ohkoshi, and Kazuhito Hashimoto. Giant coercive field of nanometer-sized iron oxide. *Advanced Materials*, 16(1):48–51, 2004.

[43] M Gich, C Frontera, A Roig, J Fontcuberta, E Molins, N Bellido, Ch Simon, and C Fleta. Magnetoelectric coupling in ε-Fe_2O_3 nanoparticles. *Nanotechnology*, 17(3):687, 2006.

[44] K Xu, JS Feng, ZP Liu, and HJ Xiang. Origin of ferrimagnetism and ferroelectricity in room-temperature multiferroic ϵ-Fe_2O_3. *Physical Review Applied*, 9(4):044011, 2018.

[45] R. L. White. Review of recent work on the magnetic and spectroscopic properties of the rare-earth orthoferrites. *Journal of Applied Physics*, 40(3):1061–1069, 1969.

[46] E Tronc, C Chanéac, JP Jolivet, and JM Greneche. Spin collinearity and thermal disorder in ε-Fe_2O_3. *Journal of Applied Physics*, 98(5):053901, 2005.

[47] J-L Rehspringer, Serge Vilminot, Daniel Niznansky, K Zaveta, Claude Estournès, and Mohamedally Kurmoo. A temperature and magnetic field dependence Mössbauer study of ε-Fe_2O_3. In *ICAME 2005*, pages 475–481. Springer, 2006.

[48] Jaroslav Kohout, Petr Brázda, K Závěta, Denisa Kubániová, T Kmječ, L Kubíčková, Mariana Klementová, Eva Šantavá, and A Lančok. The magnetic transition in ε-Fe_2O_3 nanoparticles: Magnetic properties and hyperfine interactions from Mössbauer spectroscopy. *Journal of Applied Physics*, 117(17):17D505, 2015.

[49] Richard Jones, Rachel Nickel, Palash K Manna, Joann Hilman, and Johan van Lierop. Temperature and field evolution of site-dependent magnetism in ε-Fe_2O_3 nanoparticles. *Physical Review B*, 100(9):094425, 2019.

[50] Melvin M Vopson. Fundamentals of multiferroic materials and their possible applications. *Critical Reviews in Solid State and Materials Sciences*, 40(4):223–250, 2015.

[51] Sang-Wook Cheong and Maxim Mostovoy. Multiferroics: a magnetic twist for ferroelectricity. *Nature Materials*, 6(1):13–20, 2007.

[52] Nicola A Hill. Why are there so few magnetic ferroelectrics? *The Journal of Physical Chemistry B*, 104(29):6694–6709, 2000.

[53] Daniel I Khomskii. Multiferroics: Different ways to combine magnetism and ferroelectricity. *Journal of Magnetism and Magnetic Materials*, 306(1):1–8, 2006.

[54] Nicola A Spaldin and Rammamoorthy Ramesh. Advances in magnetoelectric multiferroics. *Nature Materials*, 18(3):203–212, 2019.

[55] Manfred Fiebig, Thomas Lottermoser, Dennis Meier, and Morgan Trassin. The evolution of multiferroics. *Nature Reviews Materials*, 1(8):1–14, 2016.

[56] Haiyan Sun, Bo Chen, Xiuling Jiao, Zhen Jiang, Zhenhua Qin, and Dairong Chen. Solvothermal synthesis of tunable electroactive magnetite nanorods by controlling the side reaction. *The Journal of Physical Chemistry C*, 116(9):5476–5481, 2012.

[57] Jeotikanta Mohapatra, Arijit Mitra, Himanshu Tyagi, D Bahadur, and M Aslam. Iron oxide nanorods as high-performance magnetic resonance imaging contrast agents. *Nanoscale*, 7(20):9174–9184, 2015.

[58] Zhihui Xu, Jianru Liang, and Lixiang Zhou. Template-free hydrothermal synthesis of β-FeOOH nanorods and their catalytic activity in the degradation of methyl orange by a photo-fenton-like process. *Open Journal of Inorganic Non-Metallic Materials*, 3:58–65, 2013.

[59] Mihaela Popovici, Martí Gich, Daniel Nižňanskỳ, Anna Roig, Cecilia Savii, Lluís Casas, Elies Molins, Karel Zaveta, Corina Enache, Jordi Sort, et al. Optimized synthesis of the elusive ε-Fe_2O_3 phase via sol- gel chemistry. *Chemistry of materials*, 16(25):5542–5548, 2004.

[60] José Luis García-Muñoz, Arnau Romaguera, Francois Fauth, Josep Nogués, and Martí Gich. Unveiling a new high-temperature ordered magnetic phase in ε-Fe_2O_3. *Chemistry of Materials*, 29(22):9705–9713, 2017.

[61] Juan Rodríguez-Carvajal. Fullprof. *CEA/Saclay, France*, 2001.

[62] Brian H Toby and Robert B Von Dreele. GSAS-II: the genesis of a modern open-source all purpose crystallography software package. *Journal of Applied Crystallography*, 46(2):544–549, 2013.

[63] Ludwig Reimer. *Transmission electron microscopy: Physics of image formation and microanalysis*, volume 36. Springer, 2013.

[64] Beverley J Inkson. Scanning electron microscopy (SEM) and transmission electron microscopy (TEM) for materials characterization. In *Materials characterization using nondestructive evaluation (NDE) methods*, pages 17–43. Elsevier, 2016.

[65] Caroline A Schneider, Wayne S Rasband, and Kevin W Eliceiri. NIH Image to ImageJ: 25 years of image analysis. *Nature methods*, 9(7):671–675, 2012.

[66] P Stadelmann. Java electron microscopy software (JEMS). *Lausanne Interdiscip. Cent. Electron Microsc*, 2012.

[67] Ko-Wei Lin, Chuenhou Hao Ouyang, and Johan van Lierop. Using ion-beam-assisted deposition and ion implantation for the rational control of nanomagnetism in thin film and nanostructured systems. In *Solid State Physics*, volume 69, pages 1–45. Elsevier, 2018.

[68] Rudolf L Mössbauer. Kernresonanzfluoreszenz von gammastrahlung in Ir191. *Zeitschrift für Physik*, 151:124–143, 1958.

[69] N.N. Greenwood and T.C. Gibb. *Mössbauer spectroscopy*. Chapman and Hall Ltd, 1971.

[70] Philipp Gütlich, Eckhard Bill, and Alfred X Trautwein. *Mössbauer spectroscopy and transition metal chemistry: Fundamentals and applications*. Springer Science & Business Media, 2010.

[71] M Darby Dyar, David G Agresti, Martha W Schaefer, Christopher A Grant, and Elizabeth C Sklute. Mössbauer spectroscopy of earth and planetary materials. *Annu. Rev. Earth Planet. Sci.*, 34:83–125, 2006.

[72] Eric Lifshin. *X-ray Characterization of Materials*. John Wiley & Sons, 2008.

[73] Joachim Stöhr and Hans Christoph Siegmann. Magnetism. *Solid-State Sciences. Springer, Berlin, Heidelberg*, 5:236, 2006.

[74] Joachim Stöhr. *NEXAFS spectroscopy*, volume 25. Springer Science & Business Media, 2013.

[75] CT Chen, YU Idzerda, H-J Lin, NV Smith, G Meigs, E Chaban, GH Ho, E Pellegrin, and F Sette. Experimental confirmation of the x-ray magnetic circular dichroism sum rules for iron and cobalt. *Physical Review Letters*, 75(1):152, 1995.

[76] Eli Stavitski and Frank MF De Groot. The CTM4XAS program for EELS and

XAS spectral shape analysis of transition metal L edges. *Micron*, 41(7):687–694, 2010.

[77] Marius Retegan. Crispy: v0.7.3, 2019.

[78] Stephen P Cramer. X-ray Absorption and EXAFS. *X-Ray Spectroscopy with Synchrotron Radiation: Fundamentals and Applications*, pages 131–164, 2020.

[79] Matthew Newville. Fundamentals of XAFS. *Reviews in Mineralogy and Geochemistry*, 78(1):33–74, 2014.

[80] Bruce Ravel and Matthew Newville. ATHENA, ARTEMIS, HEPHAESTUS: Data analysis for x-ray absorption spectroscopy using IFEFFIT. *Journal of Synchrotron Radiation*, 12(4):537–541, 2005.

[81] EJW Verwey and PW Haayman. Electronic conductivity and transition point of magnetite (Fe_3O_4). *Physica*, 8(9):979–987, 1941.

[82] Benjamin Gilbert, Feng Huang, Hengzhong Zhang, Glenn A Waychunas, and Jillian F Banfield. Nanoparticles: strained and stiff. *Science*, 305(5684):651–654, 2004.

[83] J Laverock, LFJ Piper, ARH Preston, B Chen, James McNulty, KE Smith, S Kittiwatanakul, JW Lu, SA Wolf, P-A Glans, et al. Strain dependence of bonding and hybridization across the metal-insulator transition of VO2. *Physical Review B*, 85(8):081104, 2012.

[84] Nagaphani B Aetukuri, Alexander X Gray, Marc Drouard, Matteo Cossale, Li Gao, Alexander H Reid, Roopali Kukreja, Hendrik Ohldag, Catherine A

Jenkins, Elke Arenholz, et al. Control of the metal–insulator transition in vanadium dioxide by modifying orbital occupancy. *Nature Physics*, 9(10):661–666, 2013.

[85] Bin Hong, Yuanjun Yang, Kai Hu, Yongqi Dong, Jingtian Zhou, Yue Zhang, Weisheng Zhao, Zhenlin Luo, and Chen Gao. Strain engineering on the metal-insulator transition of VO2/TiO2 epitaxial films dependent on the strain state of vanadium dimers. *Applied Physics Letters*, 115(25):251605, 2019.

[86] Gregory Kh Rozenberg, Giovanni R Hearne, Moshe P Pasternak, PA Metcalf, and JM Honig. Nature of the verwey transition in magnetite (Fe_3O_4) to pressures of 16 GPa. *Physical Review B*, 53(10):6482, 1996.

[87] S Todo, N Takeshita, T Kanehara, T Mori, and N Mori. Metallization of magnetite (Fe_3O_4) under high pressure. *Journal of Applied Physics*, 89(11):7347–7349, 2001.

[88] MP Pasternak, WM Xu, G Kh Rozenberg, RD Taylor, and R Jeanloz. Pressure-induced coordination crossover in magnetite, a high pressure Mössbauer study. *Journal of Physics and Chemistry of Solids*, 65(8-9):1531–1535, 2004.

[89] Yasuo Nagasawa, Masashi Kosaka, Susumu Katano, Nobuo Môri, Sakae Todo, and Yoshiya Uwatoko. Effect of uniaxial strain on verwey transition in magnetite. *Journal of the Physical Society of Japan*, 76(Suppl. A):110–111, 2007.

[90] Xionghua Liu, Chun-Fu Chang, Aurora Diana Rata, Alexander Christoph Ko-

marek, and Liu Hao Tjeng. Fe_3O_4 thin films: controlling and manipulating an elusive quantum material. *npj Quantum Materials*, 1:16027, 2016.

[91] Jisoo Lee, Soon Gu Kwon, Je-Geun Park, and Taeghwan Hyeon. Size dependence of metal–insulator transition in stoichiometric Fe_3O_4 nanocrystals. *Nano Letters*, 15(7):4337–4342, 2015.

[92] Qing Li, Christina W Kartikowati, Shinji Horie, Takashi Ogi, Toru Iwaki, and Kikuo Okuyama. Correlation between particle size/domain structure and magnetic properties of highly crystalline Fe_3O_4 nanoparticles. *Scientific Reports*, 7(1):9894, 2017.

[93] Rachel Nickel, C-C Chi, Ashok Ranjan, Chuenhou Ouyang, John W Freeland, and Johan van Lierop. Reverse-engineering strain in nanocrystallites by tracking trimerons. *Advanced Materials*, 33(16):2007413, 2021.

[94] Amir Hevroni, Mukund Bapna, Stephan Piotrowski, Sara A Majetich, and Gil Markovich. Tracking the Verwey transition in single magnetite nanocrystals by variable-temperature scanning tunneling microscopy. *The Journal of Physical Chemistry Letters*, 7(9):1661–1666, 2016.

[95] TJ Daou, G Pourroy, S Bégin-Colin, JM Greneche, C Ulhaq-Bouillet, P Legaré, P Bernhardt, C Leuvrey, and G Rogez. Hydrothermal synthesis of monodisperse magnetite nanoparticles. *Chemistry of Materials*, 18(18):4399–4404, 2006.

[96] Javier Muro-Cruces, Alejandro G Roca, Alberto López-Ortega, Elvira Fantechi, Daniel del Pozo-Bueno, Sònia Estradé, Francesca Peiró, Borja Sepúlveda,

Francesco Pineider, Claudio Sangregorio, et al. Precise size control of the growth of Fe_3O_4 nanocubes over a wide size range using a rationally designed one-pot synthesis. *ACS Nano*, 2019.

[97] Wilhelm G Wolfer. Elastic properties of surfaces on nanoparticles. *Acta Materialia*, 59(20):7736–7743, 2011.

[98] JP Crocombette, M Pollak, F Jollet, N Thromat, and M Gautier-Soyer. X-ray-absorption spectroscopy at the Fe $L_{2,3}$ threshold in iron oxides. *Physical Review B*, 52(5):3143, 1995.

[99] C. Piamonteze, P. Miedema, and F. M. F. De Groot. Accuracy of the spin sum rule in XMCD for the transition-metal L edges from manganese to copper. *Physical Review B*, 80:1–12, 2009.

[100] Feng Lin, Dennis Nordlund, Taijun Pan, Isaac M Markus, Tsu-Chien Weng, Huolin L Xin, and Marca M Doeff. Influence of synthesis conditions on the surface passivation and electrochemical behavior of layered cathode materials. *Journal of Materials Chemistry A*, 2(46):19833–19840, 2014.

[101] ZY Wu, S Gota, F Jollet, M Pollak, M Gautier-Soyer, and CR Natoli. Characterization of iron oxides by x-ray absorption at the oxygen K edge using a full multiple-scattering approach. *Physical Review B*, 55(4):2570, 1997.

[102] I Leonov, AN Yaresko, VN Antonov, and VI Anisimov. Electronic structure of charge-ordered Fe_3O_4 from calculated optical, magneto-optical Kerr effect, and O K edge x-ray absorption spectra. *Physical Review B*, 74(16):165117, 2006.

[103] BJ Evans and SS Hafner. 57Fe hyperfine fields in magnetite (Fe_3O_4). *Journal of Applied Physics*, 40(3):1411–1413, 1969.

[104] GA Sawatzky, JMD Coey, and AH Morrish. Mössbauer study of electron hopping in the octahedral sites of Fe_3O_4. *Journal of Applied Physics*, 40(3):1402–1403, 1969.

[105] Robert Steven Hargrove and W Kündig. Mössbauer measurements of magnetite below the Verwey transition. *Solid State Communications*, 8(5):303–308, 1970.

[106] R. Řezníček, V. Chlan, H. Štěpánková, P. Novák, J. Żukrowski, A. Kozłowski, Z. Kakol, Z. Tarnawski, and J. M. Honig. Understanding the Mössbauer spectrum of magnetite below the Verwey transition: Ab initio calculations, simulation, and experiment. *Physical Review B*, 96:195124, Nov 2017.

[107] AR Muxworthy and W Williams. Micromagnetic models of pseudo-single domain grains of magnetite near the Verwey transition. *Journal of Geophysical Research: Solid Earth*, 104(B12):29203–29217, 1999.

[108] Rachel Nickel, Josh Gibbs, Jacob Burgess, Padraic Shafer, Debora Motta Meira, Chengjun Sun, and Johan van Lierop. Nanoscale size effects on push–pull Fe–O hybridization through the multiferroic transition of perovskite ϵ-Fe_2O_3. *Nano Letters*, 2023.

[109] Yuan-Chieh Tseng, Narcizo M Souza-Neto, Daniel Haskel, Martí Gich, Carlos Frontera, Anna Roig, Michel Van Veenendaal, and Josep Nogués. Nonzero

orbital moment in high coercivity ϵ-Fe_2O_3 and low-temperature collapse of the magnetocrystalline anisotropy. *Physical Review B*, 79(9):094404, 2009.

[110] Shunsuke Sakurai, Jian Jin, Kazuhito Hashimoto, and Shin-ichi Ohkoshi. Reorientation phenomenon in a magnetic phase of ε-Fe_2O_3 nanocrystal. *Journal of the Physical Society of Japan*, 74(7):1946–1949, 2005.

[111] Marin Tadic, Irena Milosevic, Slavko Kralj, Miodrag Mitric, Darko Makovec, Marie-Louise Saboungi, and Laurence Motte. Synthesis of metastable hard-magnetic ε-Fe_2O_3 nanoparticles from silica-coated akaganeite nanorods. *Nanoscale*, 9(30):10579–10584, 2017.

[112] Frank MF de Groot. XANES spectra of transition metal compounds. In *Journal of Physics: Conference Series*, volume 190, page 012004. IOP Publishing, 2009.

[113] Frank MF de Groot, ZW Hu, María Francisca López, G Kaindl, F Guillot, and M Tronc. Differences between L_3 and L_2 x-ray absorption spectra of transition metal compounds. *The Journal of Chemical Physics*, 101(8):6570–6576, 1994.

[114] J Schwitalla and H Ebert. Electron core-hole interaction in the x-ray absorption spectroscopy of $3d$ transition metals. *Physical Review Letters*, 80(20):4586, 1998.

[115] Federica Frati, Myrtille OJY Hunault, and Frank MF De Groot. Oxygen K-edge x-ray absorption spectra. *Chemical Reviews*, 120(9):4056–4110, 2020.

[116] Asuka Namai, Shinji Kurahashi, Hiroshi Hachiya, Kohtaro Tomita, Shunsuke Sakurai, Kazuyuki Matsumoto, Takashi Goto, and Shin-ichi Ohkoshi. High

magnetic permeability of ε-$Ga_xFe_{2-x}O_3$ magnets in the millimeter wave region. *Journal of Applied Physics*, 107(9):09A955, 2010.

[117] Marie Yoshikiyo, Asuka Namai, Makoto Nakajima, Keita Yamaguchi, Tohru Suemoto, and Shin-ichi Ohkoshi. High-frequency millimeter wave absorption of indium-substituted ε-Fe_2O_3 spherical nanoparticles. *Journal of Applied Physics*, 115(17):172613, 2014.

[118] Asuka Namai, Marie Yoshikiyo, and Shin-ichi Ohkoshi. Millimeter wave rotation in ε-$Al_{0.47}Fe_{1.53}O_3$ at one hundred gigahertz. *IEEE Magnetics Letters*, 7:1–4, 2016.

[119] Shin-ichi Ohkoshi, Asuka Namai, Marie Yoshikiyo, Kenta Imoto, Kazunori Tamazaki, Koji Matsuno, Osamu Inoue, Tsutomu Ide, Kenji Masada, Masahiro Goto, et al. Multimetal-substituted epsilon-iron oxide ε-$Ga_{0.31}Ti_{0.05}Co_{0.05}Fe_{1.59}O_3$ for next-generation magnetic recording tape in the big-data era. *Angewandte Chemie*, 128(38):11575–11578, 2016.

[120] Marie Yoshikiyo, Yuhei Futakawa, Ryota Shimoharai, Yusuke Ikeda, Jessica MacDougall, Asuka Namai, and Shin Ohkoshi. Aluminum-titanium-cobalt substituted epsilon iron oxide nanosize hard magnetic ferrite for magnetic recording and millimeter wave absorption. *Chemical Physics Letters*, 803:139821, 2022.

[121] Albert C Thompson, Douglas Vaughan, et al. *X-ray data booklet*, volume 8. Lawrence Berkeley National Laboratory, University of California Berkeley, CA, 2001.

[122] Robert D Shannon. Revised effective ionic radii and systematic studies of interatomic distances in halides and chalcogenides. *Acta Crystallographica Section A: Crystal physics, diffraction, theoretical and general crystallography*, 32(5):751–767, 1976.

[123] Nguyen TK Thanh, N Maclean, and S Mahiddine. Mechanisms of nucleation and growth of nanoparticles in solution. *Chemical Reviews*, 114(15):7610–7630, 2014.

[124] P Novák and V Chlan. Contact hyperfine field at Fe nuclei from density functional calculations. *Physical Review B*, 81(17):174412, 2010.

[125] Olivier Charles Gagné and Frank Christopher Hawthorne. Bond-length distributions for ions bonded to oxygen: Results for the transition metals and quantification of the factors underlying bond-length variation in inorganic solids. *IUCrJ*, 7(4):581–629, 2020.

[126] Norman Elliott. Magnetic moments of V^{2+}, Cr^{3+}, and Mn^{4+} ions in octahedral ligand fields. *The Journal of Chemical Physics*, 46(3):1006–1006, 1967.

[127] Eberhard Koster. Magnetic anisotropy of cobalt-doped gamma ferric oxide. *IEEE Transactions on Magnetics*, 8(3):428–429, 1972.

[128] Nai Li Huang, R Orbach, E Šimánek, J Owen, and DR Taylor. Cation-cation interaction contributions to the hyperfine interaction. The "supertransferred hyperfine interaction". *Physical Review*, 156(2):383, 1967.

[129] GA Sawatzky and F Van der Woude. Covalency effects in hyperfine interactions. *Le Journal de Physique Colloques*, 35(C6):C6–47, 1974.

[130] C Boekema, F Van Der Woude, and G.A. Sawatzky. Covalency effects and hyperfine interactions in the rare earth orthoferrites. *International Journal of Magnetism*, 3:341–348, 1972.

[131] Martí Gich, Ignasi Fina, Alessio Morelli, Florencio Sánchez, Marin Alexe, Jaume Gàzquez, Josep Fontcuberta, and Anna Roig. Multiferroic iron oxide thin films at room temperature. *Advanced Materials*, 26(27):4645–4652, 2014.

[132] Xiangxiang Guan, Lide Yao, Konstantin Z Rushchanskii, Sampo Inkinen, Richeng Yu, Marjana Ležaić, Florencio Sánchez, Martí Gich, and Sebastiaan van Dijken. Unconventional ferroelectric switching via local domain wall motion in multiferroic ε-Fe_2O_3 films. *Advanced Electronic Materials*, 6(4):1901134, 2020.

[133] Paolo Giannozzi, Stefano Baroni, Nicola Bonini, Matteo Calandra, Roberto Car, Carlo Cavazzoni, Davide Ceresoli, Guido L Chiarotti, Matteo Cococcioni, Ismaila Dabo, et al. QUANTUM ESPRESSO: A modular and open-source software project for quantum simulations of materials. *Journal of physics: Condensed matter*, 21(39):395502, 2009.

[134] Nelson Naveas, Ruth Pulido, Carlo Marini, Jacobo Hernández-Montelongo, and Miguel Manso Silván. First-principles calculations of hematite (α-Fe_2O_3) by self-consistent DFT+ U+ V. *Iscience*, 26(2), 2023.